12-13-2021

Relativistic and Interchannel Effects on Branching Ratios of Spin-Orbit Doublets

Chathuranga Rasadi Munasinghe

Relativistic and Interchannel Effects on Branching Ratios of Spin-Orbit Doublets

by

Chathuranga Rasadi Munasinghe

Under the Direction of Steven Manson, PhD

A Dissertation Submitted in Partial Fulfillment of the Requirements for the Degree of

Doctor of Philosophy

in the College of Arts and Sciences

Georgia State University

2021

ABSTRACT

Photoionization studies of atomic subshells have long been important tools in understanding the properties of atomic, molecular, and condensed matter systems. Recently, the ratio of photoionization cross section of atomic subshells split by the spin-orbit interaction (branching ratio) is gaining more attention in the scientific community because of the achievement of experimental measurements, which were impossible a few years ago. In this theoretical study to investigate the relativistic behavior of the photoionization process and to identify the interchannel coupling effects, numerical calculations were performed on noble gases (Ne, Ar, Kr, Xe, and Rn) and Hg using the relativistic-random-phase approximation (RRPA) based on the Dirac equation, which includes relativistic interactions in an *ab initio* manner; it also includes significant aspects of electron-electron correlation in initial and final state wave functions of the photoionization process.

At higher energies far away from the inner shell thresholds where the spin-orbit splitting is comparably insignificant, the branching ratio of spin-orbit (n*l*) doublets must go to the statistical value (*l*+1)/*l* in the absence of relativistic effects. We found the alteration of branching ratios from its statistical value at higher energies which indicates the relativistic interaction on the radial wave functions. Also, it has been found that the mechanism of interchannel coupling of the final state wave functions significantly influences the branching ratios of outer-shell doublets in the vicinity of inner-shell thresholds. Furthermore, it was found spin-orbit interaction activated interchannel coupling effects in Hg 3*d*, Rn 3*d*, and Rn 4*d* spin-orbit doublets.

INDEX WORDS: Photoionization, Spin-Orbit Doublets, Branching Ratio, Interchannel coupling, Relativistic Interaction, RRPA

Relativistic and Interchannel Effects on Branching Ratios of Spin-Orbit Doublets

by

Chathuranga Rasadi Munasinghe

Committee Chair: Steven Manson

Committee: Vadym Apalkov

Russel White

Mukesh Dhamala

Electronic Version Approved:

Office of Graduate Services

College of Arts and Sciences

Georgia State University

December 2021

DEDICATION

To my loving parents and to all who try to make the world a better place …

ACKNOWLEDGEMENTS

Firstly, I would like to express my sincere gratitude to my advisor, Dr. Steven T. Manson, for his motivation, patience, immense knowledge, guidance, and support towards the completion of this project. Also, I would like to appreciate the supervision and help I got from my committee members, Dr. Vadym Apalkov, Dr. Russel White, and Dr. Mukesh Dhamala. I need to thank all the members of my research group, especially Ms. Rezvan Khademhosseini, Dr. Ahmad Kafaee Razavi, and Dr. Prabha Padukka, for their help in completing my research works. Moreover, I am grateful to all the collaborators of our research group, especially Dr. Pranawa C. Deshmukh and his group (Indian Institute of Technology, Madras), for their expertise and support. I would like to express my gratitude to Dr. Walter R. Johnson (Notre Dame University) for his programing codes. I want to acknowledge that this work was supported by the US Department of Energy, Office of Basic Sciences, Division of Chemical Science, Geosciences, and Biosciences under Grant No. DE-FG02-03ER15428. I am also grateful to department technical staff, Dr. Justin Cantrell and Mr. Jeremy Simmons for their technical assistance. I would like to thank Mr. Bhashithe Abeysinghe (graduate assistance, Department of Computer Science) for his help with programming. I appreciate the department chair, Dr. Sebastien Lepine, and graduate director, Dr. Murad Sarsour of the Department of Physics and Astronomy at Georgia State University, for their kind understanding and opportunities. Finally, I would like to thank my loving husband, Dr. Binuka Gunawardana, for his technical assistance and immense support to complete this project and my parents, family, and friends for their encouragement.

TABLE OF CONTENTS

LIST OF TABLES

LIST OF FIGURES

LIST OF ABBREVIATIONS

HF – Hartree-Fock

DF – Dirac-Fock

RRPA – Relativistic Random Phase Approximation

Ne – Neon

Ar – Argon

Kr – Krypton

Xe – Xenon

Hg – Mercury

Rn – Radon

a. u. – atomic units

SOIAIC – Spin-Orbit Interaction Activated Interchannel Coupling.

1 INTRODUCTION

Atomic photoionization studies have garnered considerable interest recently because of their applications in a variety of technological fields and the advancement of experimental techniques such as synchrotron light sources and free electron lasers with increased brightness along with improvement in electron detection in the X-ray region. These studies allow us to study atomic dynamics in great detail, owing to the facts that the interaction between the incoming photon and the target electron is comparably weak, and the photon disappears after the photoionization process [1].

Introducing relativistic effects into quantum mechanics caused a revolution in atomic physics, allowing us to understand a number of new phenomena in atomic dynamics. Starting with the Dirac equation, which includes special relativity in an *ab initio* manner, there are many recent studies aimed at understanding how relativity affects the atomic structure and dynamics [2, 3]. An electron becomes relativistic when its kinetic energy or binding energy is a significant fraction of rest mass energy. In addition, atomic electron wave functions can contract or expand due to relativistic interactions [4].

Although there are many studies aimed at understanding relativistic influence on the photoionization process at lower energies [5-7], there is a lack of thorough understanding of this effect at the higher energy ranges. Therefore, this study is aimed at the effects of relativistic interactions in the photoionization process of atoms in the higher energy regime. Photoionization studies of spin-orbit doublets in atoms are of interest in that they spot-light relativistic interactions; in the absence of relativistic effects, the cross sections for a spin-orbit doublet should be just the ratio of their occupation numbers. The ratio of photoionization cross sections of atomic subshells split by the spin-orbit interaction is known as the branching ratio. Aside from spotlighting

relativistic effects, branching ratio data is experimentally more accurate than individual cross sections because many of the experimental uncertainties cancel out in the ratio.

The branching ratios of spin-orbit doublets are strongly energy-dependent near threshold. This energy dependence occurs due to the kinetic energy difference of the photoelectrons from the spin-orbit doublet and the significant electron-electron correlations near thresholds [6]. At higher energies, far above the thresholds, where the energy splitting of the $j = l \pm 1$ states is comparably insignificant, this kinetic energy effect is unimportant, and branching ratios of spin-orbit n*l* doublets must reach its statistical value of $(l+1)/l$ in the absence of relativistic forces [6]. Therefore, the alteration of the branching ratio from its statistical value at higher energies indicates the existence of relativistic interactions on the radial wave functions. Decades ago, this was theoretically predicted [8] and recently been verified experimentally [8, 9]. From this earlier theoretical work [8], It was expected that the branching ratio continually decreases with the energy without reaching a limit due to the relativistic alteration of the initial state wave functions. To understand this effect both qualitatively and quantitatively, we investigate the behavior of the branching ratios of spin-orbit doublets over a broad energy range for the closed-shell atoms Ne, Ar, Ne Kr, Xe, Hg, and Rn, i.e., from Z=10 to Z=86.

Also, in high-energy regions, just above the inner-shell thresholds, structures can be found in branching ratio data due to the influence of relativistic effect on the interchannel coupling of the final state wave functions [9, 10]. The other purpose of this study is to get a broad understanding of these effects as a function of energy, subshell angular momentum, and atomic number (Z). To accomplish this, spin-orbit doublets of the six elements listed above were studied over a wide range of energy.

Calculations have been performed to obtain cross sections and branching ratios of the listed elements using the Relativistic-Random-Phase Approximation (RRPA) which is based on the Dirac Equation and includes relativistic interactions on an *ab initio* basis [11, 12]. RRPA calculations contain significant aspects of electron-electron correlation in initial and final state wave functions of the photoionization process; the initial state two-particle two-hole correlations; and the final state in the form of interchannel coupling (configuration interaction in the continuum) [11, 12]. Furthermore, RRPA allows to perform the calculation with selected relativistic single-photoionization channels omitted, and, therefore, specific aspect of interchannel coupling can be identified. RRPA has been applied at low energies, where correlation is significant and resulted in excellent agreement with experimental branching ratios [5]. Therefore, it is safe to assuming that it is at least as accurate at higher energies, where correlation is generally much less important, and this has already been demonstrated in several cases [9, 13]. However, strictly speaking, RRPA is applicable only for closed subshell systems. Therefore, all the noble gasses from Ne to Rn were used in this study which will help in the understanding of the atomic behavior of elements in the periodic table over a wide Z range. Moreover, this theoretical analysis is also focused on the transition metal Hg, anticipating to fill the lack of experimental photoionization studies of Hg because of the difficulty arising from the damage made on experimental setups by its evaporation.

The next chapter of this dissertation will explain the theoretical aspects of photoionization and discuss RRPA calculations' details. Succeeding chapters will present results obtained through this analytical work and conclusions.

2 THEORY

2.1 Photoionization

The process of a photon of energy $\hbar\omega$ being absorbed by an atom or molecule with the subsequent emission of an electron is known as photoionization [14, 15]. If the *X(i)* is the initial atomic system in state *i* and the residual positive ion $X(j)^+$ is in the state *j*, then the single photoionization process can be expressed as,

$$\hbar\boldsymbol{\omega} + \boldsymbol{X}(\boldsymbol{i}) \longrightarrow \boldsymbol{X}(\boldsymbol{j})^+ + \boldsymbol{e}^-, \tag{2.1}$$

In most cases, X(i) and X(j)+ refer to their ground state, but they can also be excited states. The ejected electron is known as photoelectron, and if its kinetic energy is ε, then the fundamental relation of the photoionization process is,

$$\boldsymbol{\varepsilon} = \hbar\boldsymbol{\omega} - \boldsymbol{I}_{\boldsymbol{ij}}, \tag{2.2}$$

The threshold (minimum) energy needed to remove an electron from *X(i)*, leaving $X(j)^+$ is represented by I_{ij}. If *i* and *j* represent ground states, I_{ij} is the binding energy of the ejected electron [14].

2.1.1 Photoionization Cross Section

Since not all photons incident on an atomic system can ionize the system, the probability of ionization of an *nl* subshell due to an incident beam of photons is defined as the photoionization cross section [3]. The photoionization cross section, σ_{nl} can be expressed as the number of ionizations per unit time per atom, divided by the incident photon flux. To drive the general formula for the photoionization cross section, nonrelativistic Hamiltonian *H* [16] will be used for simplicity. The relativistic influence will be discussed later in section 2.2.3. Let us consider an atom or ion containing *N* electrons and a nucleus charge of *Ze* (In Gaussian units);

$$\boldsymbol{H} = \sum_{\mu=1}^{N}\left(-\frac{\hbar^2}{2m}\boldsymbol{\nabla}_{r_\mu}^2 - \frac{Ze^2}{r_\mu}\right) + \sum_{\mu<\gamma+1}^{N}\frac{e^2}{r_{\mu\gamma}}, \tag{2.3}$$

where m is the electron mass, r_μ is the relative coordinate of the μ^{th} electron with respect to the nucleus, and $r_{\mu\gamma} = |r_\mu - r_\gamma|$. The first two terms represent each electron's kinetic and potential energy under the attractive Coulomb interaction of the nucleus, and the last term describes the Coulomb repulsion between the electrons [16]. The semi-classical Hamiltonian *H(t)* for a system of charged particles under the influence of electromagnetic radiation field can be written as follows [16],

$$\boldsymbol{H}(\boldsymbol{t}) = \frac{1}{2m}\sum_{\mu=1}^{N}\left[\boldsymbol{p}_\mu + \frac{|e|}{c}\boldsymbol{A}(\boldsymbol{r}_\mu, \boldsymbol{t})\right]^2 + \boldsymbol{\Phi}, \tag{2.4}$$

where $A(r_\mu,t)$ is the vector potential for the radiation field, $p_\mu = -i\hbar\nabla$ is the momentum operator of the μ^{th} electron and Φ is the sum of the all interactions in the absence of radiation field, $\Phi = -\sum_{\mu=1}^{N}\left(\frac{Ze^2}{r_\mu}\right) + \sum_{\mu<\gamma+1}^{N}\frac{e^2}{r_{\mu\gamma}}$. Combining equations (2.3) and (2.4) and using the Coulomb gauge ($\boldsymbol{\nabla}\cdot\boldsymbol{A} = 0$) where momentum and vector potential commute, it can be shown that the time-dependent Hamiltonian for an atomic system under electromagnetic radiation is $H + H_{int}(t)$, where interaction Hamiltonian $H_{int}(t)$ is,

$$\boldsymbol{H}_{\boldsymbol{int}}(\boldsymbol{t}) = \frac{|e|}{mc}\sum_{\mu=1}^{N}\boldsymbol{A}(\boldsymbol{r}_\mu, \boldsymbol{t})\cdot\boldsymbol{p}_\mu + \frac{e^2}{2mc^2}\sum_{\mu=1}^{N}\boldsymbol{A}^2(\boldsymbol{r}_\mu, \boldsymbol{t}), \tag{2.5}$$

and H is as defined in the equation 2.3.

Furthermore, we consider only the weak field case so that the A^2 is negligible compared to the linear terms in A, and the process can be treated as a small perturbation. So, we end up only with the first term of the equation (2.5) as the $H_{int}(t)$. Then the vector potential can be chosen as follows treating the incident radiation classically [17],

$$\boldsymbol{A}(\boldsymbol{r}_\mu, \boldsymbol{t}) = \left(\frac{2\pi c^2\hbar}{\omega V}\right)^{1/2}\hat{\boldsymbol{\epsilon}}\boldsymbol{e}^{\boldsymbol{i}(\boldsymbol{k}\cdot\boldsymbol{r}_\mu - \boldsymbol{\omega t})}, \tag{2.6}$$

where V is the spatial volume, $\hat{\epsilon}$ is the polarization direction, k is the wave vector, and the ω is the angular frequency of the incident radiation. The exponential term can be expanded as follows,

$$\boldsymbol{e^{ik\cdot r_\mu} \approx 1 + i\kappa \cdot r_\mu + \frac{1}{2!}\left(ik \cdot r_\mu\right)^2 + \cdots,} \tag{2.7}$$

Then, using the electric dipole approximation [18], which is applicable for our purposes as explained in Appendix A, the above expansion replaced by unity. By applying this approximation in equation (2.6) and plugging it to equation (2.5) gives,

$$\boldsymbol{H_{int}(t) = \frac{|e|}{mc}\left(\frac{2\pi c^2\hbar}{\omega V}\right)^{1/2} \sum_{\mu=1}^{N} \hat{\epsilon} \cdot p_\mu \, e^{-i\omega t},} \tag{2.8}$$

Then for further calculations, let us describe the atomic photoionization process in *LS* (orbital angular momentum L and spin angular momentum S) coupling,

$$\boldsymbol{X(L,S,M_L,M_s,\wp_X) + \gamma(\wp_\gamma,l_\gamma,m_\gamma) \longrightarrow X^+(\overline{LS}\wp_{X^+})\varepsilon l(L',S',M_{L'},M_{S'}),} \tag{2.9}$$

Here γ represents the photon, l is the orbital angular momentum of the photoelectron, and $\wp$ denotes the parity. For the photoionization process, initial and final quantum numbers must satisfy the angular momentum and parity selection rules for the electric dipole transitions [1, 17, 19]. Then, the final state wave function ψ_f satisfies the following asymptotic boundary condition so that the photoelectron is ionized into a specific transition channel α [17, 19].

$$\begin{aligned}\boldsymbol{\psi_f(r_1S_1,\ldots,r_NS_N)_{r_N\to\infty} \longrightarrow \varphi_\alpha(r_1S_1,\ldots,r_NS_N)\frac{1}{i(2\pi k_\alpha)^{\frac{1}{2}}}\frac{1}{r_N}e^{i\Delta_\alpha}}\\ \boldsymbol{-\sum_{\alpha'}\varphi_{\alpha'}(r_1S_1,\ldots,r_NS_N)\frac{1}{i(2\pi k_{\alpha'})^{\frac{1}{2}}}\frac{1}{r_N}e^{i\Delta_{\alpha'}}S^\dagger_{\alpha'\alpha},}\end{aligned} \tag{2.10}$$

$$\boldsymbol{\Delta_\alpha = k_\alpha r_N - \frac{1}{2}\pi l_\alpha + \frac{1}{k_\alpha}log2k_\alpha r_N + \theta_{l_\alpha},} \tag{2.11}$$

where k_α is the photoelectron momentum in channel α and θ_{l_α} is the Coulomb phase shift. The negative part of equation (2.10) indicates the normalization of the incoming wave function in channel α with $S^\dagger_{\alpha'\alpha}$ being the Hermitian conjugate of the *S*-matrix of scattering theory [19]. In

addition, to represent a final state with a well-defined k_α and spin states $m_{1/2}$ for the photoelectron along with well define ionic states, an alternate final-state wave function can be obtained and related to ψ_f by uncoupling the ionic and electronic angular momenta and then projecting the photoelectron's angular momentum states l_α, m_α in the direction of $\hat{k}_\alpha$ [17, 19]. i. e.,

$$\boldsymbol{\psi_{\alpha k_\alpha}(r_1 S_1, \ldots, r_N S_N) = \sum_{l_\alpha m_\alpha} \frac{i^{l_\alpha} e^{-\theta_{l_\alpha}}}{k_\alpha^{\frac{1}{2}}} Y^*_{l_\alpha m_\alpha}(\hat{k}_\alpha) \sum_{LM_L SM_S} \langle \bar{L} M_{\bar{L}} l_\alpha m_\alpha | L M_L \rangle}$$

$$\boldsymbol{\times \left\langle \bar{S} M_{\bar{S}} \tfrac{1}{2} m_{\frac{1}{2}} \middle| S M_S \right\rangle \psi_f(r_1 S_1, \ldots, r_N S_N),} \qquad \textbf{(2.12)}$$

where $Y^*_{l_\alpha m_\alpha}(\hat{k}_\alpha)$ indicates the spherical harmonics.

Meanwhile, using the first-order perturbation theory, which means treating the radiative transitions for a single photon emitted or absorbed [16], transition rate is obtained as equation (2.13) [3, 17, 19]; the second-order perturbation theory result is smaller by a factor of 1/137 than the first-order result and can be neglected so that,

$$\boldsymbol{dW_{k_\alpha} = \frac{2\pi}{\hbar} |\langle \psi_i | H_{int} | \psi_{\alpha k_\alpha} \rangle|^2 \delta(E_f - E_i - \hbar\omega) k_\alpha{}^2 dk_\alpha d\Omega(\hat{k}_\alpha),} \qquad \textbf{(2.13)}$$

where ψ_i is the initial state wave function, ψ_f is the final state wave function, and their energies are E_i and E_f correspondingly. $d\Omega$ is the differential solid angle, and the delta function expresses the energy conservation. Substituting $H_{int}(0)$ from the equation (2.8), dividing the transition rate by incident photon current density c/V, and integrating over dk_α, the differential photoionization cross section for channel α is,

$$\boldsymbol{\frac{d\sigma_\alpha}{d\Omega} = \frac{4\pi^2}{\omega c} k_\alpha \left(\frac{e^2}{m\hbar^2}\right) |\hat{\epsilon} \cdot \langle \psi_i | \sum_{\mu=1}^{N} p_\mu | \psi_{\alpha k_\alpha} \rangle|^2.} \qquad \textbf{(2.14)}$$

Substituting ψ_f from the equation (2.12) in the equation (2.14) and carrying out numerous summations over quantum numbers gives the relationship for the differential cross section [17, 19].

$$\frac{d\sigma_\alpha}{d\Omega} = \frac{\sigma_\alpha}{4\pi}[\mathbf{1} + \boldsymbol{\beta} \boldsymbol{P_2}(\boldsymbol{cos\theta})], \quad \textbf{(2.15)}$$

where β is the asymmetry parameter, which is discussed in detail in section 3.2, and θ is the angle between outgoing photoelectron and the polarization vector of the incident photons. The photoionization cross section σ_{ij} of a system in initial state *i*, photoionized by a photon beam of energy $\hbar\omega$ and going to final state *f* consisting with photoelectrons of energy ε and with the ion left in state *j* is [14, 19, 20],

$$\boldsymbol{\sigma_{ij}(\varepsilon)} = (\boldsymbol{4\pi^2 a_0^2 \alpha / 3 g_i})(\boldsymbol{\varepsilon + I_{ij}})\left|\boldsymbol{M_{if}}\right|^2, \quad \textbf{(2.16)}$$

In equation (2.16), Rydberg units are used where a_0 is the Bohr radius, and α(~1/137) is the fine structure constant so that $a_0 = \hbar^2/me^2$, $\alpha = e^2/\hbar c$, energy is measured in the units of $e^2/2a_0$ and wave number is in the units of $1/a_0$. I_{ij} is the ionization energy so that $I_{ij} + \varepsilon = E_f - E_i = \hbar\omega$ as in equation (2.2) and g_i is the number of degenerate sublevels at the initial state energy. The dipole matrix element [14, 20] is given by,

$$\left|\boldsymbol{M_{if}}\right| = \frac{\hbar^2}{\boldsymbol{m^2(\varepsilon + I_{ij})^2}}\left|\langle\boldsymbol{\psi_i}|\sum_{\boldsymbol{\mu=1}}^{\boldsymbol{N}} \boldsymbol{p_\mu}\,|\boldsymbol{\psi_f}\rangle\right|^2. \quad \textbf{(2.17)}$$

2.1.2 Velocity and length forms of the dipole matrix element

If we consider the nonrelativistic Hamiltonian of an atomic system, where p_μ and r_μ satisfy the commutation relations, $\left[x_\mu, p_{\mu'_y}\right] = 0$, $\left[x_\mu, p_{\mu'_x}\right] = i\hbar\delta_{\mu\mu'}$, etc., then,

$$\left[\boldsymbol{r_\mu}, \boldsymbol{H}\right] = \boldsymbol{i\hbar p_\mu / m}, \quad \textbf{(2.18)}$$

If we consider initial and final states of the photoionization process to be eigenstates of the exact Hamiltonian [14, 20] so that, $H|\psi_i\rangle = E_i|\psi_i\rangle$ and $H|\psi_f\rangle = E_f|\psi_f\rangle$ then from equation (2.18) we get,

$$\langle \psi_i | [r_\mu, H] | \psi_f \rangle = \frac{i\hbar}{m} \langle \psi_i | p_\mu | \psi_f \rangle = (E_f - E_i) \langle \psi_i | r_\mu | \psi_f \rangle , \quad \textbf{(2.19)}$$

Therefore, alternative velocity and length forms of the dipole matrix can be written as equations (2.17) and (2.20), respectively,

$$|M_{if}| = |\langle \psi_i | \sum_{\mu=1}^{N} r_\mu | \psi_f \rangle|^2, \quad \textbf{(2.20)}$$

Exact wave functions are not available other than for the Hydrogen atom. Therefore, approximate wave functions are using for photoionization calculations of other atoms. Then the results from using length and velocity forms of the dipole matrix can differ considerably which means that one, and possibly, both are incorrect. Even though two forms give the same results, they can still be incorrect. Thus, equality of the outcomes from different forms of dipole matrix is necessary but not sufficient for the accuracy of the result. The acceleration form is another alternative form of the dipole matrix, and it is strongly dependent on the details of the wave function near the nucleus [14, 20]. But approximate wave functions are usually generated by the variational principle on the energy that is not very sensitive to wave function near the nucleus. Therefore, most of the time, only velocity and length forms are computed and compared.

2.2 Wave Function Calculations

2.2.1 Central field calculations

The simplest wave functions used in photoionization calculations are based on the central-field approximation, i.e., a Hamiltonian $H_o = \sum_\mu [\left(\frac{p_\mu^2}{2m}\right) + \Phi(r_\mu)]$, where the central potential $\Phi(r_\mu)$ is a function of the scalar r_μ only. Then the wave functions are linear combinations of products of one-electron wave functions, and the radial parts of those functions are solutions of one-body Schrödinger equation [14]. In this method, if more than one electron changes quantum numbers,

the matrix element vanishes, and therefore multiple transitions are excluded. Also, after the transition, the remaining electrons rearrange (core relaxation), which is not included in this method. That is because the initial and final states are solutions of the Schrödinger equation in the same central potential, and thus orbitals not involved in direct transition will not change. Furthermore, in these calculations, velocity and length forms are necessarily equal, and therefore, they cannot be used to check the result, as discussed in section 2.1.2.

If we consider hydrogenic potential in central-field approximation, the nuclear charge screening effect by other electrons will not work correctly for smaller r_μ and larger r_μ situations [14]. Therefore, we need boundary conditions like in Thomas-Fermi potential approximation, but it does not include shell effects [21]. The Hartree self-consistent-field method includes shell effects, but it does not contain exchange terms [22]. Since the exchange is nonlocal non-central interaction, it is impossible to have exchange terms with a central potential field. But, by forming a weighted mean of the exchange charges and considering them as a free electron gas, Slater introduced an average potential field that approximates the exchange effect [23]. This average potential, combined with the Hartree method, can be used to obtained central-field wave functions.

2.2.2 Hartree-Fock (HF) calculations

Wave functions as a linear combination of one-electrons functions can still be obtained while correctly maintaining exchange terms using the Hartree-Fock method [24]. According to this approach, congruent with Pauli exclusion principle and independent-particle approximation, the N-electron wave function $\psi(q_1, q_2, \dots, q_N)$ can be written as an antisymmetric product of individual electron spin-orbitals (Slater determinant) as follows [16, 24].

$$\boldsymbol{\psi(q_1, q_2, \ldots, q_N)} = \frac{\mathbf{1}}{\sqrt{N!}} \begin{vmatrix} \boldsymbol{u_\alpha(q_1)} & \boldsymbol{u_\beta(q_1)} & \cdots & \cdots & \boldsymbol{u_\nu(q_1)} \\ \boldsymbol{u_\alpha(q_2)} & \boldsymbol{u_\beta(q_2)} & \cdots & \cdots & \boldsymbol{u_\nu(q_2)} \\ \vdots & \vdots & & & \vdots \\ \boldsymbol{u_\alpha(q_N)} & \boldsymbol{u_\beta(q_N)} & \cdots & \cdots & \boldsymbol{u_\nu(q_N)} \end{vmatrix}, \quad \textbf{(2.21)}$$

where $\alpha, \beta, \ldots, \nu$ represent the quantum numbers $n, l, m_l,$ and m_s. Then the Hartree-Fock is obtained using the variational method to get the optimum individual electron spin-orbitals. If we consider the Hamiltonian H in equation (2.3), and total energy is $E[\psi]$, then the ground state energy, $E_0 \leq E[\psi] = \langle\psi|H|\psi\rangle$, and $\langle\psi|\psi\rangle = 1$. Thus the total energy in atomic units is,

$$\boldsymbol{E[\psi]} = \sum_{\boldsymbol{\lambda}} \langle \boldsymbol{u_\lambda(q_i)} \left| -\frac{\mathbf{1}}{\mathbf{2}} \boldsymbol{\nabla_{r_i}^2} - \frac{\boldsymbol{Z}}{\boldsymbol{r_i}} \right| \boldsymbol{u_\lambda(q_i)} \rangle + \frac{\mathbf{1}}{\mathbf{2}} \sum_{\boldsymbol{\lambda}} \sum_{\boldsymbol{\mu}} \left[\boldsymbol{J_{\lambda\mu}} - \boldsymbol{K_{\lambda\mu}} \right], \quad \textbf{(2.22)}$$

where, $J_{\lambda\mu}$ and $K_{\lambda\mu}$ represent the direct and exchange terms respectively and $\lambda, \mu = \alpha, \beta, \ldots, \nu$.

$$\boldsymbol{J_{\lambda\mu}} = \left\langle \boldsymbol{u_\lambda(q_i) u_\mu(q_i)} \left| \frac{\mathbf{1}}{\boldsymbol{r_{ij}}} \right| \boldsymbol{u_\lambda(q_i) u_\mu(q_i)} \right\rangle, \quad \textbf{(2.23)}$$

$$\boldsymbol{K_{\lambda\mu}} = \left\langle \boldsymbol{u_\lambda(q_i) u_\mu(q_i)} \left| \frac{\mathbf{1}}{\boldsymbol{r_{ij}}} \right| \boldsymbol{u_\mu(q_i) u_\lambda(q_i)} \right\rangle, \quad \textbf{(2.24)}$$

where $r_{ij} = |r_i - r_j|$. For the variation of the spin-orbitals, $E[\psi]$ should remain stationary because ψ represents an orthonormal set owing to the condition that the value of a determinant remains unchanged by any non-singular linear transformation. To satisfy this condition, N^2 Lagrange multipliers ($\varepsilon_{\lambda\mu}$) can be introduced, and then the variational equation reads [16],

$$\boldsymbol{\delta E} - \sum_{\boldsymbol{\lambda}} \sum_{\boldsymbol{\mu}} \boldsymbol{\varepsilon_{\lambda\mu}} \boldsymbol{\delta \langle u_\mu | u_\lambda \rangle} = \mathbf{0}, \quad \textbf{(2.25)}$$

According to equation (2.25), $\varepsilon_{\lambda\mu} = \varepsilon_{\lambda\mu}^*$, so that the Lagrange multipliers act like the elements of a Hermitian matrix. Using the unitary transformation, any Hermitian matrix can be diagonalized, and therefore Lagrange multipliers become a diagonal matrix with elements $E_\lambda \delta_{\lambda\mu}$.

$$\boldsymbol{\delta E} - \sum_{\boldsymbol{\lambda}} \boldsymbol{E_\lambda} \boldsymbol{\delta \langle u_\lambda | u_\lambda \rangle} = \mathbf{0}, \quad \textbf{(2.26)}$$

Now the Hartree-Fock equation can be obtained as a system of integrodifferential equations [16].

$$E_\lambda u_\lambda(q_i) = \left[-\frac{1}{2}\nabla_{r_i}^2 - \frac{Z}{r_i}\right] u_\lambda(q_i) + \left[\sum_\mu \int u_\mu^*(q_j)\frac{1}{r_{ij}} u_\mu(q_j) d \right] u_\lambda(q_i)$$

$$- \left[\sum_\mu \int u_\mu^*(q_j)\frac{1}{r_{ij}} u_\lambda(q_j) d \right] u_\mu(q_i), \qquad \textbf{(2.27)}$$

In the Hartree-Fock equation each of the spin-orbitals are similar to Schrödinger eigenvalue equations. Iterations can be used to solve this system of integrodifferential equations. One first calculates the direct and exchange terms using approximate individual spin-orbitals. Then the Hartree-Fock equation is solved with direct and exchange terms, which in turn yields new spin-orbitals. This procedure is repeated until the calculated direct and exchange terms are identical to the previous cycle's terms. Then the corresponding spin-orbitals indicate the final wave function.

2.2.3 Dirac-Fock (DF) calculations

To introduce relativistic effect (including spin-dependent interactions) to the atomic structure, the Hartree-Fock method can be modified by replacing the Schrödinger equation with the Dirac equation. Dirac introduced a wave equation based on Schrödinger and Gordon-Klein wave equations consistent with Lorentz transformations [2]. To deal with the particle of spin ½, it required a two-component wave function for the two spin states. Also, it was found that spin ½ particles are associated with antiparticles, leading to a four-component wave function [16]. Therefore, the relativistic wave equation has positive and negative eigenvalues corresponding to particle and antiparticle states, as indicated in figure 2.1.

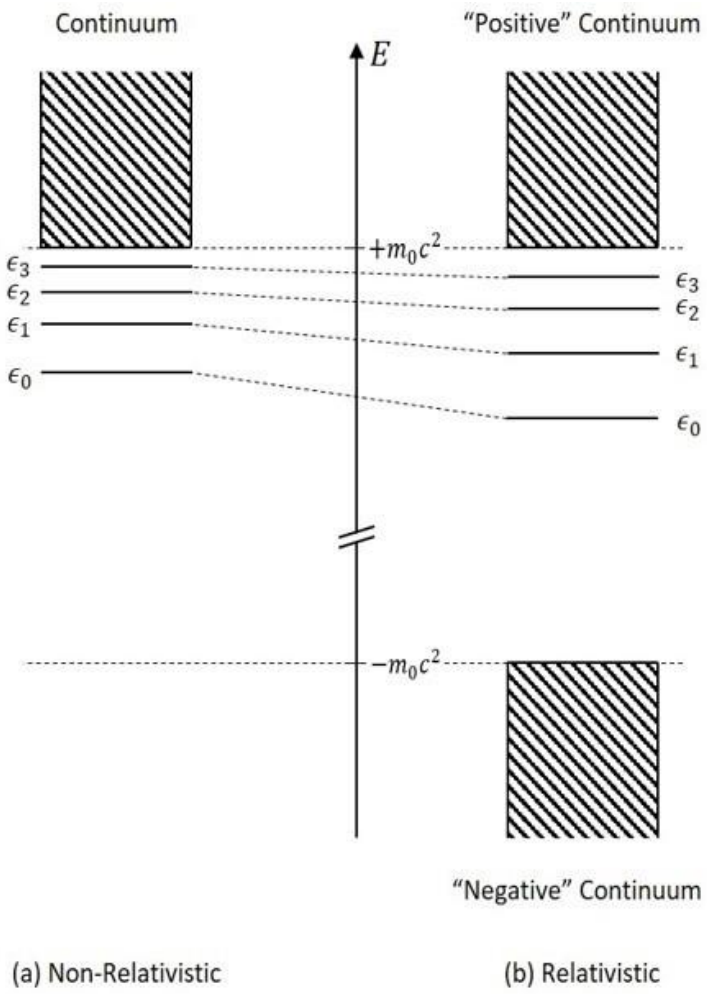

Figure 2.1 Schematic diagram of electron (a) nonrelativistic and (b) relativistic states in a mean atomic potential.

The Dirac-Coulomb Hamiltonian for N-electron atom in a central field of the nucleus of charge Z [25-27] (in atomic units) is,

$$\boldsymbol{H_{DC} = \sum_i^N H_D(r_i) + U(r_i) = \sum_i^N (c\alpha_i . p_i + \beta_i c^2 + V_{nuc}(r_i)) + \phi(r_i)}, \quad \textbf{(2.28)}$$

where V_{nuc} is the nuclear potential, ϕ is a spherically symmetric potential that occurs due to the other remaining bound electrons, p is the momentum operator, c is the speed of light, and α and β are Dirac matrices constructed from 2×2 Pauli spin matrices (σ) [26] and 2×2 identity matrix (I) as follows,

$$\boldsymbol{\alpha} = \begin{bmatrix} \mathbf{0} & \boldsymbol{\sigma} \\ \boldsymbol{\sigma} & \mathbf{0} \end{bmatrix} \quad \textbf{and} \quad \boldsymbol{\beta} = \begin{bmatrix} \boldsymbol{I} & \mathbf{0} \\ \mathbf{0} & -\boldsymbol{I} \end{bmatrix}, \tag{2.29}$$

If $\psi(r)$ is the four-component Dirac spinors wave function,

$$\boldsymbol{H_{DC}\psi(r)} = (\boldsymbol{E} + \boldsymbol{m_e c^2})\boldsymbol{\psi(r)}\,, \tag{2.30}$$

where E is the total energy, not including the rest mass energy $m_e c^2$, Then the solution for the $\psi(r)$ can be written as follows with the large $P_\kappa(r)$ and small $Q_\kappa(r)$ radial components of one-electron wave functions [25, 26, 28, 29].

$$\boldsymbol{\psi(r)} = \frac{\mathbf{1}}{r}\begin{pmatrix} \boldsymbol{P_\kappa(r)} & \boldsymbol{\chi_{\kappa,m}(\theta,\varphi)} \\ \boldsymbol{iQ_\kappa(r)} & \boldsymbol{\chi_{-\kappa,m}(\theta,\varphi)} \end{pmatrix}, \tag{2.31}$$

Here κ and m represent the angular momentum quantum numbers, and θ and φ represent the angular coordinates of r. The spinors $\boldsymbol{\chi_{\pm\kappa,m}}$ are Eigenfunctions of the total angular momentum j^2, j_z, and parity define as [25, 26],

$$\boldsymbol{\kappa} = -\left(\boldsymbol{j} + \frac{\mathbf{1}}{\mathbf{2}}\right); \qquad \boldsymbol{\chi_{\kappa,m}} = \begin{bmatrix} \left[\frac{\boldsymbol{j+m}}{\mathbf{2}\boldsymbol{j}}\right]^{\mathbf{1/2}} & \boldsymbol{Y}^{\boldsymbol{m-\frac{1}{2}}}_{\boldsymbol{j-\frac{1}{2}}}(\boldsymbol{\theta},\boldsymbol{\varphi}) \\ \left[\frac{\boldsymbol{j-m}}{\mathbf{2}\boldsymbol{j}}\right]^{\mathbf{1/2}} & \boldsymbol{Y}^{\boldsymbol{m+\frac{1}{2}}}_{\boldsymbol{j-\frac{1}{2}}}(\boldsymbol{\theta},\boldsymbol{\varphi}) \end{bmatrix}, \tag{2.32}$$

$$\boldsymbol{\kappa} = +\left(\boldsymbol{j} + \frac{\mathbf{1}}{\mathbf{2}}\right); \qquad \boldsymbol{\chi_{\kappa,m}} = \begin{bmatrix} -\left[\frac{\boldsymbol{j+1-m}}{\mathbf{2}\boldsymbol{j+2}}\right]^{\mathbf{1/2}} & \boldsymbol{Y}^{\boldsymbol{m-\frac{1}{2}}}_{\boldsymbol{j+\frac{1}{2}}}(\boldsymbol{\theta},\boldsymbol{\varphi}) \\ \left[\frac{\boldsymbol{j+1+m}}{\mathbf{2}\boldsymbol{j+2}}\right]^{\mathbf{1/2}} & \boldsymbol{Y}^{\boldsymbol{m+\frac{1}{2}}}_{\boldsymbol{j+\frac{1}{2}}}(\boldsymbol{\theta},\boldsymbol{\varphi}) \end{bmatrix}, \tag{2.33}$$

Then as in section 2.2.2 Hartree-Fock method, the variational condition can be represented by equation (2.34) with the indices a and b referring to one-electron orbitals $(n_a\kappa_a)$ and $(n_b\kappa_b)$ [29].

$$\boldsymbol{\delta(E - \sum_{ab}\delta(\kappa_a,\kappa_a)\lambda_{ab}\langle a|b\rangle)} = \mathbf{0}\,, \tag{2.34}$$

λ_{ab} indicates the introduced Lagrange multipliers to ensure the orthogonality of the orbitals with the same angular momentum quantum numbers. Then the radial Dirac Hamiltonian,

$$\boldsymbol{H_D} = \begin{bmatrix} \boldsymbol{V(r) + mc^2} & \boldsymbol{c\left[\frac{d}{dr} - \frac{\kappa}{r}\right]} \\ \boldsymbol{c\left[\frac{d}{dr} + \frac{\kappa}{r}\right]} & \boldsymbol{V(r) - mc^2} \end{bmatrix}, \tag{2.35}$$

The resulting Dirac-Fock coupled first-order differential equations are [25, 26, 29, 30],

$$\boldsymbol{(V(r) + mc^2)P_{a,\kappa}(r) + c\left(\frac{d}{dr} - \frac{\kappa}{r}\right)Q_{a,\kappa}(r) = \varepsilon_a P_{a,\kappa}(r) + \sum_{b\neq a}\varepsilon_{ab}P_{\kappa}(r)}, \tag{2.36}$$

$$\boldsymbol{-c\left(\frac{d}{dr} + \frac{\kappa}{r}\right)P_{a,\kappa}(r) + (V(r) - mc^2)Q_{a,\kappa}(r) = \varepsilon_a Q_{a,\kappa}(r) + \sum_{b\neq a}\varepsilon_{ab}Q_{\kappa}(r)}, \tag{2.37}$$

where $V(r) = V_{nuc}(r) + \phi(r)$. The normalization condition for $\psi(r)$ leads that the total radial density is finite [25, 28],

$$\boldsymbol{\int_0^\infty p_\kappa^2(r) + Q_\kappa^2(r) = 1}. \tag{2.38}$$

The potential V_{nuc} depends on the finite size of the distribution of nuclear charges. Spherically symmetric nuclear charge distribution can be interpolated as follows [26, 29],

$$\boldsymbol{V_{nuc}(r)} = \begin{cases} \boldsymbol{-\frac{Z}{R}\left(\frac{3}{2} - \frac{r^2}{2R^2}\right), for\ r \le R_{rms}} \\ \boldsymbol{-\frac{Z}{r}, \qquad for\ r > R_{rms}} \end{cases}, \tag{2.39}$$

The $\boldsymbol{R_{rms}}$ is the root-mean-square radius of the nucleus $R = \sqrt{\frac{5}{3}}\boldsymbol{R_{rms}}$.

Moreover, modifications can be added for this standard model to fix the energy shifts occurring due to nuclear recoil, vacuum polarization, and other radiative corrections [25, 26]. The interaction between electrons that arises due to the exchange of transverse photons is called the Breit interaction [26, 31]. This interaction recounts the relativistic correction for the motion of electrons because of the magnetic and retardation effects. Breit operator is derived using the quantum electrodynamic perturbation theory [29, 31],

$$\boldsymbol{H_{ij}^{Breit} = -\frac{1}{r_{ij}}\left[\alpha_i \cdot \alpha_j - \frac{(\alpha_i \cdot r_{ij})(\alpha_j \cdot r_{ij})}{2r_{ij}^2}\right]}, \tag{2.40}$$

Where α indicates the Dirac matrices. The Breit operator is added to the Dirac-Coulomb Hamiltonian to make the Breit correction in the atomic structure calculations.

2.3 Relativistic Random-Phase Approximation (RRPA)

The many experimental and theoretical studies revealed that the electron correlations within and among subshells are crucial components of the atomic photoionization process [3, 32]. Electron correlation includes the many-body interactions among the electron of an atom in both initial (discrete) and final (continuum) states of photoionization [33]. Therefore, it was required to develop new methods without limiting the calculation to single-particle and single-channel models, such as we discussed in section 2.2. Various methods are employed to fulfill this requirement, and among those, is the Relativistic Random-Phase approximation (RRPA) [11, 34]. RRPA is based on the Dirac equation, and therefore it is explicitly relativistic. RRPA includes the ground state correlations and interchannel couplings of the final state (configuration interaction in the continuum) while omitting self-interaction error present in Hartree calculations [34]. Also, in this method, all single excitation and ionization channels are included. However, there are some limitations, such as omitting satellite channels [14], and this method only applicable for closed-shell atoms [33]. Despite these limitations, RRPA methodology generally agrees with the experimental data within the range of the experimental errors [12, 33].

RRPA starts with the Dirac-Fock equation (equation (2.28)) with the Dirac Hamiltonian (equation (2.35)), and then the DF potential $\phi(r)$ is given by [12],

$$\boldsymbol{\phi u}(\boldsymbol{r}) = \sum_{j=1}^{N} \boldsymbol{e^2} \int \frac{\boldsymbol{d^3 r'}}{|\boldsymbol{r}-\boldsymbol{r'}|} \left[\left(\boldsymbol{u_j^\dagger u_j} \right)' \boldsymbol{u} - \left(\boldsymbol{u_j^\dagger u} \right)' \boldsymbol{u_j} \right], \qquad \textbf{(2.41)}$$

Where $u_i(r)$ represents the DF orbitals and natural units are used. If a time-dependent external field ($v_+ e^{-i\omega t} + v_- e^{i\omega t}$) is applied, it causes a time-dependent perturbation,

$$\boldsymbol{u_i(r) \rightarrow\ u_i(r) + w_{i+}(r)e^{-i\omega t} + w_{i-}(r)e^{i\omega t}},\tag{2.42}$$

where higher-order terms are neglected, and w_i represents the perturbed orbitals. Generalization of equation (2.28) and expand it in powers of the external field taking only the first-order terms gives,

$$\boldsymbol{(H_D + \phi - \varepsilon_i \mp \omega)w_{i\pm} = \left(v_\pm - V_\pm^{(1)}\right)u_i + \sum_j \lambda_{ij}u_j},\tag{2.43}$$

Where the $\boldsymbol{\lambda_{ij}}$ denote the Lagrange multipliers introduced in order to ensure orthogonality of perturbed orbitals, ε_i denotes the orbital energy eigenvalue and the $\phi_\pm^{(1)}$ are the first-order perturbations of ϕ, including the electron-electron correlations [11, 12].

$$\boldsymbol{\phi_\pm^{(1)}u_i = \sum_{j=1}^{N} e^2 \int \frac{d^3r'}{|r-r'|}\left[\left(u_j^\dagger w_{j\pm}\right)' u_i + \left(w_{j\mp}^\dagger u_j\right)' u_i - \left(w_{j\mp}^\dagger u_i\right)' u_j - \left(u_j^\dagger u_i\right)' w_{j\pm}\right]},\tag{2.44}$$

The basic RRPA equation is obtained by omitting the driving term $v_\pm$ and isolating ω in equation (2.42) [11, 12]. Then the eigenvalues of ω gives an approximation to the excitation spectrum. w_{i+} represents the excited state, including the final state correlations, and w_{i-} represents the ground state correlations [11, 12]. The orthogonality constraint for these eigenfunctions is,

$$\boldsymbol{\int d^3r\, w_{i\pm}^\dagger u_j = 0},\tag{2.45}$$

Then the transition amplitude T from the ground state to excited state can be obtained in terms of the vector potential A and Dirac matrices α as,

$$\boldsymbol{T = \sum_{i=1}^{N} e \int d^3r\,(w_{i+}^\dagger \alpha \cdot A u_i + u_i^\dagger \alpha \cdot A w_{i-})},\tag{2.46}$$

To construct the radial RRPA equation for an atomic excitation with angular momentum J and M, auxiliary functions $y_{\bar{k}\bar{m}\pm}$ can be introduced [11, 12]. These auxiliary functions project the excited state orbitals $w_{nkm\pm}(r)$ onto excitation channels $(nk, \bar{k})$ with explicit angular momentum $\bar{k}\bar{m}$,

$$\boldsymbol{w_{nkm+}(r) = \sum_{\bar{k}\bar{m}}(-1)^{j-m}\langle j\ -m\, j\bar{m}|jjJM\rangle \times \pi(l,\bar{l},J+\lambda-1)y_{\bar{k}\bar{m}+}(r)},\tag{2.47}$$

$$\boldsymbol{w_{nkm-}(r) = \sum_{\bar{k}\bar{m}}(-1)^{j-m+M}\langle j\ -m\, j\bar{m}|jjJ\ -M\rangle \times \pi(l,\bar{l},J+\lambda-1)y_{\bar{k}\bar{m}-}(r)},\tag{2.48}$$

where π is a parity operator; for orbitals a and b,

$$\boldsymbol{\pi} = \begin{cases} \mathbf{1} & \boldsymbol{if\ \ l_a + l_b + l\ \ is\ even} \\ \mathbf{0} & \boldsymbol{if\ \ l_a + l_b + l\ \ is\ odd} \end{cases}, \tag{2.49}$$

The parity of the excited state JM is determined by λ parameter as;

- $\lambda = 1 \rightarrow$ state with parity $(-1)^J \rightarrow$ electric 2^J pole excitation.
- $\lambda = 0 \rightarrow$ state with parity $(-1)^{J+1} \rightarrow$ magnetic 2^J pole excitation.

The auxiliary function can be written in terms of large and small radial components as in the DF wave function (equation (2.31)). For simplicity, let's denote unperturbed orbitals (nk) by $a,b,\ldots$ and the perturbed orbital ($nk \rightarrow \bar{k}$) by $\bar{a}$, $\bar{b}$, …

$$\boldsymbol{y_{\bar{a}\pm}(r)} = \begin{pmatrix} \boldsymbol{S_{\bar{a}\pm}(r)} \\ \boldsymbol{T_{\bar{a}\pm}(r)} \end{pmatrix}, \tag{2.50}$$

Substituting equations (2.47) and (2.48) into RRPA equation, radial RRPA equation can be obtained for electric ($\pi = (-1)^J$) and magnetic ($\pi = (-1)^{J+1}$) cases as equation (2.51) and (2.52) correspondingly [11, 12].

$$\begin{aligned} [\boldsymbol{H_{\bar{a}} - (\varepsilon_a \pm \omega)}]\boldsymbol{y_{\bar{a}\pm}(r)} = & -\boldsymbol{C_J(a,\bar{a})V_J^{(1)}(r)Q_a(r)} \\ & + \textstyle\sum_{b\bar{b}l}[\boldsymbol{A\left(a,b,\bar{a},\bar{b},l,J\right)\frac{e^2}{r}Y_l(a,b,r)y_{\bar{b}\pm}(r)} \\ & + \boldsymbol{(-1)^{j_b - j_{\bar{b}}} A\left(a,\bar{b},\bar{a},b,l,J\right)\frac{e^2}{r}Y_l\left(a,\bar{b}\mp,r\right)Q_b(r)} \\ & + \textstyle\sum_b \boldsymbol{\delta_{k_b\bar{k}_a}\lambda_{\bar{a}b\pm}Q_b(r)}, \end{aligned} \tag{2.51}$$

$$\begin{aligned} [\boldsymbol{H_{\bar{a}} - (\varepsilon_a \pm \omega)}]\boldsymbol{y_{\bar{a}\pm}(r)} = & \textstyle\sum_{b\bar{b}l}[\boldsymbol{F\left(-a,-b,\bar{a},\bar{b},l,J\right)\frac{e^2}{r}Y_l(a,b,r)y_{\bar{b}\pm}(r)} \\ & + \boldsymbol{(-1)^{j_b - j_{\bar{b}}} A\left(-a,-\bar{b},\bar{a},b,l,J\right)\frac{e^2}{r}Y_l\left(a,\bar{b}\mp,r\right)Q_b(r)}] \\ & + \textstyle\sum_b \boldsymbol{\delta_{k_b\bar{k}_a}\lambda_{\bar{a}b\pm}Q_b(r)}, \end{aligned} \tag{2.52}$$

Where $Y_l(a,b,r)$ is the Hartree-screening function [35], and C_J and F are the angular momentum coefficients,

$$\boldsymbol{C_J(a,b) = (-1)^{j_a+\frac{1}{2}}\sqrt{(2j_a+1)}\sqrt{(2j_b+1)}\begin{pmatrix} j_a & j_b & J \\ -\frac{1}{2} & \frac{1}{2} & 0 \end{pmatrix}\pi(l_a,l_b,J),} \quad \textbf{(2.53)}$$

$$\boldsymbol{F(a,b,c,d,l,J) = (-1)^{l+J-j_b-j_c}C_l(a,b)C_l(c,d)\times\begin{Bmatrix} j_a & j_b & l \\ j_d & j_c & J \end{Bmatrix}\pi(l_a,l_c,J)\pi(l_b,l_d,J),} \quad \textbf{(2.54)}$$

$$\boldsymbol{V_J^{(1)}(r) = \sum_{b\bar{b}}\frac{C_J(b,\bar{b})}{(2J+1)}\frac{e^2}{r}\left[Y_J(b,\bar{b}+,r) + Y_J(b,\bar{b}-,r)\right],} \quad \textbf{(2.55)}$$

where the curly bracket indicates the 6-*j* symbol.

3 CALCULATION METHODOLOGY

Calculations begin with obtaining ground state discrete wave functions and subshell threshold energies of atoms using the DF method. In this procedure, the iteration is continued by solving the equations (2.36) and (2.37) using the numerical Green's function techniques [36]. Then those data were used as inputs for photoionization calculations which are based on the RRPA method. This procedure also uses numerical Green's function techniques to solve equations (2.51) and (2.52) iteratively, starting with approximate single-channel solutions to the (N-1) case [12], where N is the number of electrons in the atom. Calculations have been performed to obtain asymmetry parameter, cross sections, and branching ratios of noble gasses (Ne, Ar, Kr, Xe, Rn) and Hg over a wide energy range using RRPA based on the Dirac Equation, which includes relativistic interactions on an *ab initio* basis as discussed in section 2.3. Also, RRPA calculations include significant aspects of electron-electron correlation in initial and final state wave functions of the photoionization process; the initial state two-particle two-hole correlations, and the final state in the form of inter-channel coupling (configuration interaction in the continuum). Furthermore, RRPA allows to perform the calculation with some of the photoionization transition channels omitted, and therefore the specific aspect of inter-channel coupling can be identified. The omission of excitation of electrons in certain subshells was obtained using truncated RRPA equation,

$$\left[\boldsymbol{H}_{\bar{a}}^{(N-1)} - (\boldsymbol{\varepsilon}_a + \boldsymbol{\omega})\right]\boldsymbol{y}_{\bar{a}}^{-}(\boldsymbol{r}) = \boldsymbol{R}_{\bar{a}} + \boldsymbol{\lambda}_{\bar{a}b}\boldsymbol{Q}_b(\boldsymbol{r}), \tag{3.1}$$

In this chapter, all the symbols follow the same meanings defined in the RRPA theory section 2.3. The negative frequency orbitals ($w_{-}(r)$ and therefore $y_{\bar{a}-}(r)$) are neglected, and it is called Tamm-Dancoff approximation [37]. The coupling term $R_{\bar{a}}$ for electric ($\pi = (-1)^J$) and magnetic

($\pi = (-1)^{J+1}$) cases defined as equation (3.2) and (3.3) correspondingly [11]. The primes on the sums in these equations indicate the omission of corresponding *a* and *b* channels.

$$\boldsymbol{R_{\bar{a}} = -C_J(a,\bar{a})\sum'_{b,\bar{b}} \frac{C_J(b,\bar{b})}{(2J+1)} \frac{e^2}{r} Y_l(b,\bar{b},r) Q_a(r)} + \sum'_{b,\bar{b},l} \boldsymbol{A(a,b,\bar{a},\bar{b},l,J)} \frac{e^2}{r} \boldsymbol{Y_l(a,b,r) y_{\bar{b}}(r)}, \quad \textbf{(3.2)}$$

$$\boldsymbol{R_{\bar{a}} = \sum'_{b,\bar{b},l} A(-a,-\bar{b},\bar{a},b,l,J)} \frac{e^2}{r} \boldsymbol{Y_l(a,b,r) y_{\bar{b}}(r)}, \quad \textbf{(3.3)}$$

In this project, all the DF and RRPA calculations were done numerically using Fortran codes. Nonrelativistic calculations were done using the same code by setting the limit of the speed of light $c \to \infty$ [25]. For all the RRPA results, the dipole calculations (J =1) were performed as described in equations (2.47), (2.48), and (3.7). Moreover, both length and velocity forms of the RRPA dipole matrix elements (Appendix A) were calculated (as in equations (3.9) and (3.10) respectively) and checked for equality to ensure the validity as discussed in section 2.1.2.

Just below the threshold of each subshell, there are auto-ionization resonance regions. Auto-ionization is a radiationless decay of an atom in an excited state above the ionization potential which undergoes a transition into the continuum [38]. we have not considered these resonance regions (from about 0.15 a.u. below each threshold to the threshold) because the spectator Auger process is not included in the RRPA method. A spectator Auger process is the where an inner-shell electron is photoexcited into a Rydberg orbital, an excited state above the ionization potential, and remains as a spectator to core Auger transitions [39].

3.1 Photoionization cross section and branching ratio calculations

In terms of the transition amplitude *T* in equation (2.46), differential photoionization cross section is given as [12],

$$\frac{d\sigma}{d\Omega} = \frac{\alpha E p}{2\pi\omega}|T|^2, \tag{3.4}$$

Where σ is the photoionization cross section, $d\Omega$ is the differential solid angle, ω is the photon energy, and E and p are the photoelectron energy and momentum, respectively. Then the differential cross section for a specific subshell nk can be found by,

$$\frac{d\sigma_{nk}}{d\Omega} = \sum_{L=0}^{\infty} A_L P_L(cos\theta), \tag{3.5}$$

where A_L is a function of ω, and it depends bi-linearly on the reduced matrix element $\left\langle \bar{a} \left\| Q_J^{(\lambda)} \right\| a \right\rangle_{RRPA}$ of the multipole moment operator $Q_J^{(\lambda)}$ [12]. The angle between the photon direction and the photoelectron momentum vectors is denoted by θ. Integrating the right-hand side of the equation (3.5) over outgoing electron directions [12] gives,

$$\sigma_{nk}(\omega) = \frac{2\pi^2\alpha}{\omega}\sum_{J\bar{K}\lambda}\frac{J+1}{J(2J+1)}\frac{\omega^{2J}}{[(2J-1)!!]^2} \times \left|\left\langle \bar{a} \left\| Q_J^{(\lambda)} \right\| a \right\rangle_{RRPA}\right|^2, \tag{3.6}$$

If we only consider electric dipole amplitudes with $J = \lambda = 1$, the differential cross section is left only with two non-vanishing terms,

$$\frac{d\sigma_{nk}}{d\Omega} = \frac{\sigma_{nk}(\omega)}{4\pi}\left[1 - \frac{1}{2}\beta_{nk}(\omega)P_2(cos\theta)\right], \tag{3.7}$$

with,

$$\sigma_{nk}(\omega) = \frac{4\pi^2\alpha}{3}\,\omega\left(\left|D_{j\to j-1}\right|^2 + \left|D_{j\to j}\right|^2 + \left|D_{j\to j+1}\right|^2\right), \tag{3.8}$$

where scattering amplitudes $D_{j\to\bar{j}} = i^{1-l}e^{i\delta k}\left\langle \bar{k} \left\| Q_J^{(\lambda)} \right\| k \right\rangle_{RRPA}$.

In the low-frequency limit,

Length gauge:

$$\left\langle \bar{b}_{\pm} \| Q_1^{(1)} \| b \right\rangle = C_1(b,\bar{b})\int_0^{\infty} dr\, r[S_{\bar{b}\pm}P_b + T_{\bar{b}\pm}Q_b], \tag{3.9}$$

Velocity gauge:

$$\left\langle \bar{b}_{\pm} \| Q_1^{(1)} \| b \right\rangle = \pm C_1(b, \bar{b}) \frac{1}{\omega} \int_0^{\infty} dr \left[(k_b - \bar{k}_b + 1) S_{\bar{b}_{\pm}} Q_b + (k_b - \bar{k}_b - 1) T_{\bar{b}_{\pm}} P_b \right], \quad \textbf{(3.10)}$$

where S and T represent the large and small components of the perturbed orbitals (equation (2.50)) while P and Q represent the large and small components of the unperturbed orbitals (equation (2.31)) respectively.

The ratio of photoionization cross sections of atomic subshells split by the spin-orbit interaction is known as the branching ratio. The spin-orbit interaction splits nl ($l \neq 0$) subshells into $j = l \pm 1/2$ states [40]. These subshells contain different energies. For example, if the outer np^6 subshell of a noble gas atom is photoionized, then the residual np^5 ion can be left in two distinct states $^2p_{1/2}$ or $^2p_{3/2}$. Therefore, depending on the residual ion, photoelectrons can have two different energies. By separating these subshells as individual photoionization transition channels in RRPA calculation, partial cross sections for spin-orbit doublets can be obtained. The ratios between these partial cross sections were calculated as the branching ratio of p, d, and f orbitals ($^2p_{3/2}$:$^2p_{1/2}$, $^2d_{5/2}$:$^2d_{3/2}$, $^2f_{5/2}$:$^2f_{7/2}$).

3.2 Angular distribution asymmetry parameter calculations

The angular distribution of photoelectrons relative to the direction of the incident photon or the photon polarization is used as a tool to study various aspects of the photoionization process [7]. When a photon absorbed by an atom at an energy low enough that the dipole approximation is valid, the angular relationship between the incident photon and the photoelectron is proportional to a linear combination of 1 and $cos^2\theta$ [41] as represented in the equation (3.7). Then the angular distribution asymmetry parameter β can be calculated in terms of scattering amplitudes [11, 41, 42] as,

$$\beta_{nk}(\omega) = \left[\frac{1}{2}\frac{(2j-3)}{2j}|D_{j\to j-1}|^2 - \frac{3}{2j}\left(\frac{2j-1}{2(2J+2)}\right)^{\frac{1}{2}}(D_{j\to j-1}D^*_{j\to j} + c.c.) - \frac{(2j-1)(2j+3)}{(2j)(2j+2)}|D_{j\to j}|^2\right.$$

$$-\frac{3}{2}\left(\frac{(2j-1)(2j+3)}{(2j)(2j+2)}\right)^{\frac{1}{2}}(D_{j\to j-1}D^*_{j\to j+1} + c.c.) + \frac{1}{2}\frac{(2j+5)}{(2j+2)}|D_{j\to j+1}|^2 \qquad \textbf{(3.11)}$$

$$\left.+\frac{3}{(2j+2)}\left(\frac{(2j+3)}{2(2j)}\right)^{\frac{1}{2}}(D_{j\to j}D^*_{j\to j+1} + c.c.)\right]\left(|D_{j\to j-1}|^2 + |D_{j\to j}|^2 + |D_{j\to j+1}|^2\right)^{-1},$$

Therefore, the energy dependence of β provides information about the relativistic and inter-channel coupling effects of the photoionization process [7, 30, 41].

4 RESULTS AND DISCUSSION

This chapter presents the calculated results for branching ratios of *nl* spin-orbit doublet of noble gases and Hg. In the absence of relativistic effects (neglecting spin effects) i.e., in *LS* coupling, the asymptotic high-energy branching ratio should approach the statistical value of *(l+1)/l* [6]. This results from the multiplicity of the initial states of a spin-orbit doublet ($2j+1$ degeneracy of the orbitals), along with the assumption that the radial wave functions, particularly for the initial state, are the same for both members of the doublet [43].

$$\frac{\sigma_{j=l+1/2}}{\sigma_{j=l-1/2}} = \frac{n_{l+1/2}}{n_{l-1/2}} = \frac{{}^{l+1}/_{2l+1}}{{}^{l}/_{2l+1}} = \frac{l+1}{l}. \qquad \textbf{(4.1)}$$

It was shown that near-threshold regions with electron-electron correlation and the kinetic energy difference of photoelectron emitted from spin-orbit doublet are significant; the branching ratio is non-statistical [6]. But at higher energies, away from inner-shell thresholds, where the magnitude of the spin-orbit splitting is relatively insignificant, the deviation from the statistical value would demonstrate a relativistic (j-dependence) of the $j = l \pm 1/2$ initial state wave functions [40]. This can be explained by noting that, due to relativistic interactions, the electrons in spin-orbit doublets have different radial wave functions [8, 9, 43-45]. However, there are only a few studies regarding this matter in high-energy branching ratio regions. Moreover, just above the thresholds significant structures have been found in the branching ratio data due to the interchannel coupling effects. In this section, both these phenomena were thoroughly investigated over a broad energy range for all the higher subshells of six different closed-shell atoms with Z from 10 to 86. Since the length and velocity dipole matrix element calculated are essentially the same, only the velocity calculations are included in all the plots.

4.1 Neon (Ne)

We start with Ne, the element with the lowest atomic number that has been studied. For the Ne calculations, all the single-excitation relativistic dipole photoionization channels of 1*s*, 2*s*, and 2*p* were coupled (Appendix B). Table 4-1 shows the relativistically and nonrelativistically calculated threshold values of each subshell. For low *Z* elements like Ne, relativistic and nonrelativistic thresholds do not deviate much from each other. The nonrelativistic values for 2*p* spin-orbit doublets are the same due to the omission of spin effects.

Table 4-1 Calculated subshell thresholds of Ne in atomic energy units

Subshell	Threshold (Relativistic)	Threshold (NonRelativistic)
1*s*	32.817	32.772
2*s*	1.936	1.930
2*p*(1/2)	0.853	0.850
2*p*(3/2)	0.848	0.850

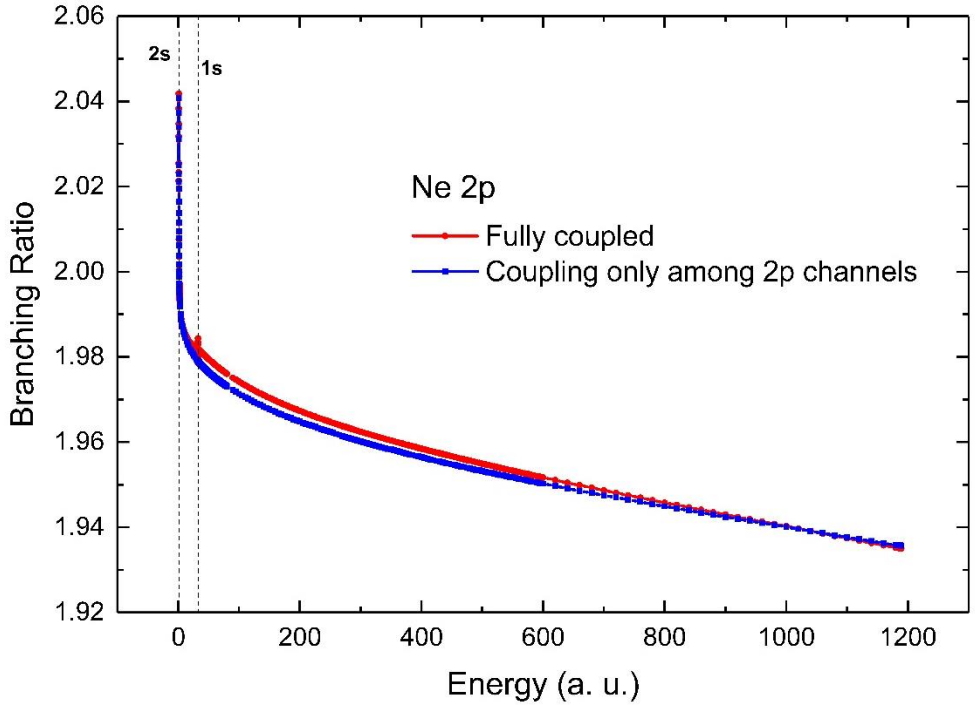

Figure 4.1 Branching ratio of Ne 2p $\left(\sigma_{2p(3/2)}/\sigma_{2p(1/2)}\right)$ *calculated with fully coupled (red-dots), and without coupling of 1s and 2s channels (blue-squares). The vertical dashed lines indicate the thresholds.*

Figure 4.1 shows the $2p$ branching ratio $\left(\sigma_{2p(3/2)}/\sigma_{2p(1/2)}\right)$ of Ne in the whole energy range studied. From figure 4.1, it can be clearly seen that the Ne $2p$ branching ratio depends on incident photon energy, which shows the effects of the relativistic modification of the $2p$ wave functions. Both fully coupled and 1*s* and 2*s* uncoupled branching ratios continuously decrease away from its statistical value of 2 (equation 4.1) with the increasing energy. The deviation of the coupled results from the uncoupled indicates that the interchannel coupling is affected by the relativistic interactions as well. Moreover, this result reinforces the earlier conclusion that interchannel coupling affects most subshells of most atoms at most energies and collapsing the independent particle approximation [46, 47]. Even though this deviation is not huge, it agrees with the previous prediction that the branching ratio never approaches its statistical value at higher energies due to the relativistic effects [8, 33, 45, 48]. To clearly identify this behavior and compare it with the behavior of high Z elements, the branching ratio of Ne $2p$ above the 1*s* threshold is shown in figure 4.2.

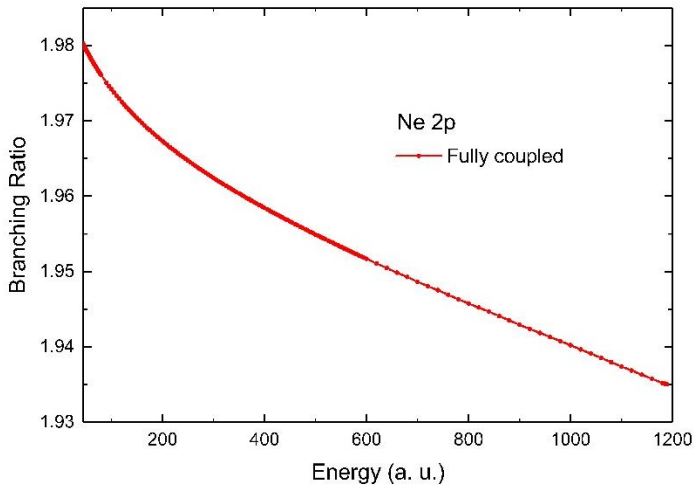

Figure 4.2 High energy behavior of calculated Ne 2p branching ratio $\left(\sigma_{2p(3/2)}/\sigma_{2p(1/2)}\right)$.

The Ne result can be explained using the behavior of the dipole matrix element. The matrix element is generated at smaller and smaller r, closer to the nucleus, with increasing energy. From a physical standpoint, this occurs due to the constraints of the combination of energy and momentum conservation in the photoionization process. At higher energies, most of the momentum of the photon must be absorbed by the nucleus, where most of the atomic mass is concentrated. Therefore, photoabsorption is much more likely to occur near the nucleus. Parenthetically, that is why a free electron cannot absorb a photon because, in such a situation, momentum cannot be conserved. From a mathematical viewpoint, this happens because, at higher energies, the continuum wave function becomes more oscillatory. Therefore, matrix element beyond the first node of the wave function cancels out. Moreover, with increasing energy, the first node of the wave function gets closer and closer to the nucleus.

At larger r (further away from the nucleus), both nl_j spin-orbit states (in this case, both $2p(1/2)$ and $2p(3/2)$) behave similarly, thus creating virtually identical wave functions. But smaller r (closer to the nucleus), nl_j bound states behave differently determined by j according to the Dirac equation [49]. Because of the spin-orbit effect, the $l+1/2$ wave function is slightly repelled from the nucleus while the $l-1/2$ wave function is drawn closer to the nucleus. In fact, it turns out that the ratio of the radial charge densities of states corresponding to $l-1/2$ divided by $l+1/2$ increases as r decreases and diverges as $1/r^2$ as $r \rightarrow 0$. Thus for smaller r, the wave function of $l-1/2$ enhanced relative to its counterpart $l+1/2$, thereby increasing the $l-1/2$ dipole matrix element. This difference is caused to the decreases in branching ratio from its statistical value at higher energies where matrix elements are dominated by smaller r.

According to figure 4.1, the branching ratio calculated with no interchannel coupling from ns channels slightly deviates from the fully coupled result, demonstrate that the interchannel

coupling has a small effect over a vast energy range. Moreover, there is a small kink in figure 4.1 around the 1*s* threshold, and it is shown in greater detail in figure 4.3.

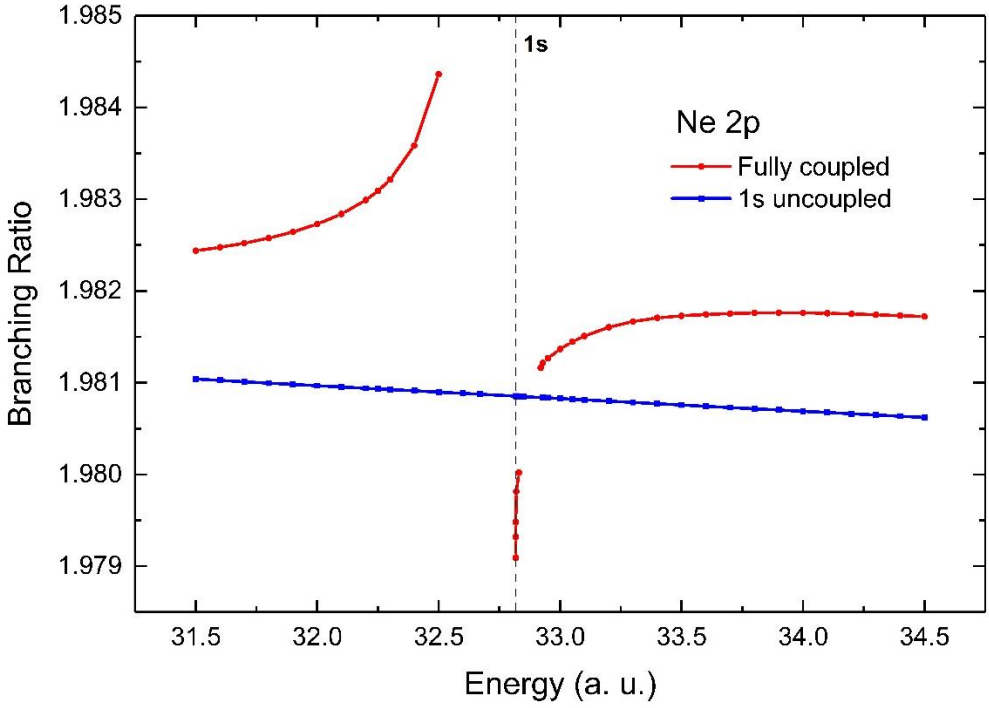

Figure 4.3 Branching ratio of Ne 2p $\left(\sigma_{2p(3/2)}/\sigma_{2p(1/2)}\right)$ *calculated with fully coupled (red-dots), and without coupling to 1s channels (blue-squares). The vertical dashed line indicates the 1s threshold.*

As in figure 4.3, the interchannel coupling is seen to have a small effect in the vicinity of the 1s threshold. The plot representing the calculations without coupling of 1*s* channels quite smooth through this region manifests that the structure around 1*s* threshold is due to the interchannel coupling. Tailing up in the fully coupled curve just below the threshold indicates the beginning of the $2p \rightarrow ns, nd$ resonances. Data in the resonance region was not included because of the omission of spectator Auger effect of RRPA calculations, as discussed in chapter 3. Just above the 1*s* threshold, there is a slight rise in the fully coupled curve, thereby indicating the

interchannel coupling affects the 2*p*(3/2) and the 2*p*(1/2) ionization probabilities differently, i.e., the interchannel coupling is affected by relativistic interactions. Even though the 1*s* cross section is much larger than the 2*p* cross sections, this effect is very small. This is because the interchannel coupling matrix element is relatively small here due to the fact that the overlap of 2*p* and 1*s* wave functions is quite small in this region. It is interesting to note that even at so low a Z as 10, relativistic effects are evident.

4.2 Argon (Ar)

Going up in Z, Ar was studied with all the single-excitation relativistic dipole photoionization channels of 1*s*, 2*s*, 2*p*, 3*s*, and 3*p* coupled. Table 4-2 shows the relativistically and nonrelativistically calculated subshell threshold values of Ar.

Table 4-2 Calculated subshell thresholds of Ar in atomic energy units

Subshell	Threshold (Relativistic)	Threshold (NonRelativistic)
1*s*	119.127	118.610
2*s*	12.412	12.322
2*p*(1/2)	9.632	9.571
2*p*(3/2)	9.547	9.571
3*s*	1.287	1.277

For Ar, still, *Z*(=18) is relatively low, and therefore relativistic and nonrelativistic thresholds do not deviate much from each other. However, it can be clearly seen that with the increasing atomic number, the deviation increases because of the enhancement of the relativistic effect with *Z*. Moreover, outer subshells experiencing lower deviation due to the shielding of the nucleus by inner subshells. Essentially, the nonrelativistic values for 2*p* spin-orbit doublets are the same due to the absence of spin effects.

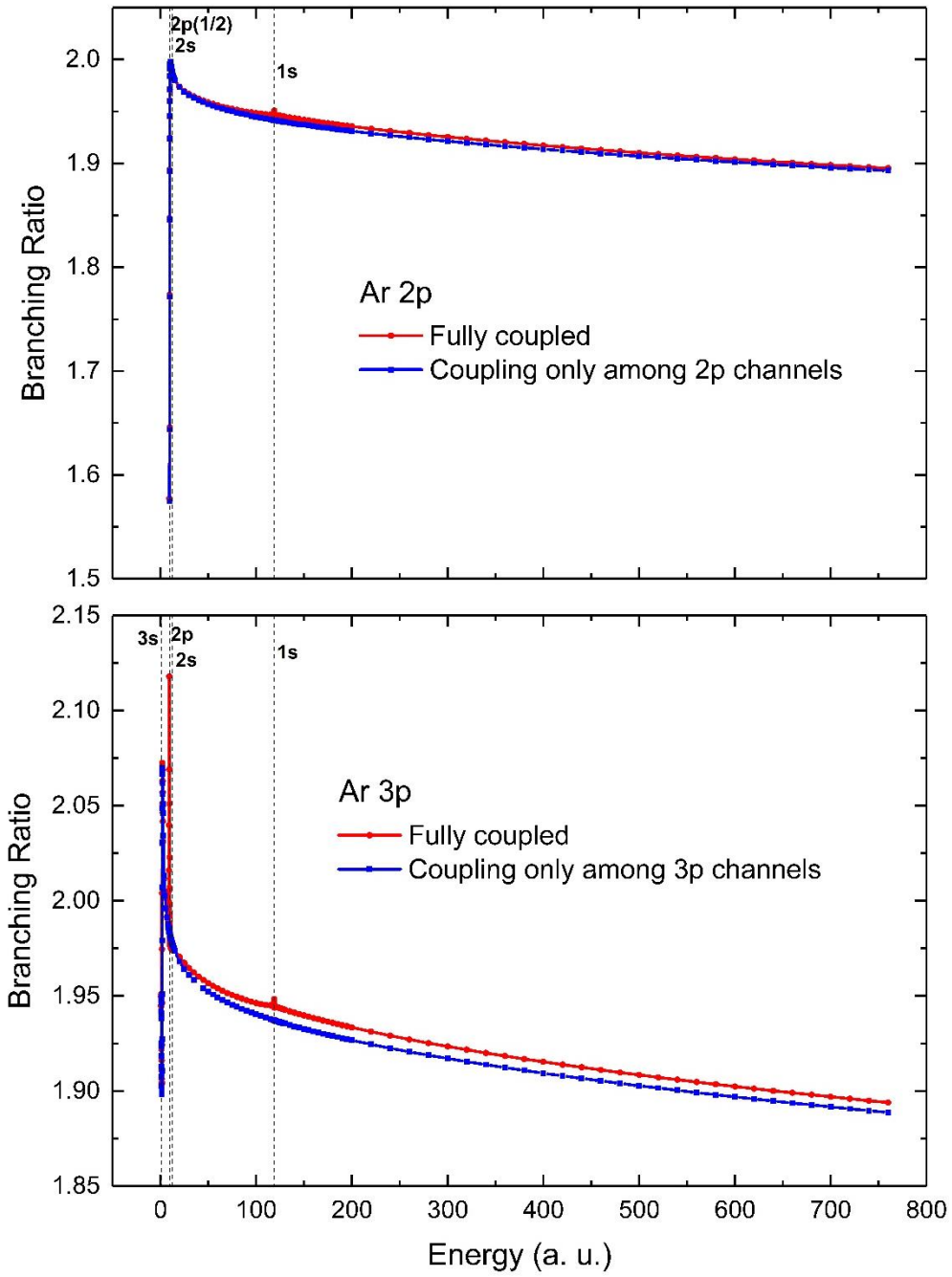

Figure 4.4 Branching ratio of Ar 2p $\left({}^{\sigma_{2p(3/2)}}/_{\sigma_{2p(1/2)}}\right)$ *(upper panel) and 3p* $\left({}^{\sigma_{3p(3/2)}}/_{\sigma_{3p(1/2)}}\right)$ *(lower panel) calculated with fully coupled (red-dots), and with coupling only among 2p and 3p channels respectively (blue-squares). The vertical dashed lines indicate the thresholds.*

Figure 4.4 shows the 2*p* and 3*p* branching ratios of Ar in the whole energy range studied. Even though the 2*p* and 3*p* branching ratios differ from each other at low energies, they are remarkably similar at higher energies, indicating that the initial state principal quantum number is not important for their high-energy behavior. To clearly show this behavior, the branching ratio of Ar 2*p* and 3*p* above the 1*s* threshold are shown together in figure 4.5. This can be explained by considering that the high-energy dipole matrix elements are generated closer to the nucleus (smaller *r*). Since in this region, effect of the nuclear potential is quite large, binding energies are essentially irrelevant. Furthermore, in this region of space, the wave functions of different initial states of the same *l* are the same, except for an overall normalization factor [50-52]. This normalization factor cancels out when the cross section ratio is calculating, thus causing the high-energy branching ratios for states of the same *l* to be the same, exactly as the Ar results indicate.

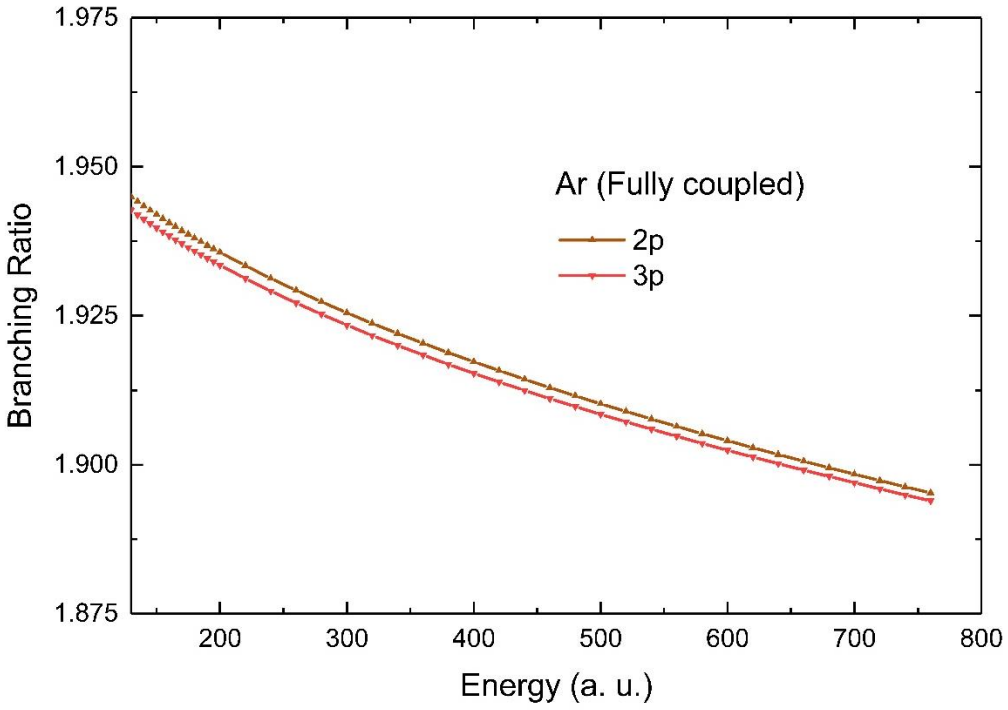

Figure 4.5 Comparison of Ar branching ratios 2p (Brown-upward triangles) and 3p (pink-downward triangles) above the 1s threshold.

As in Ne, Ar branching ratios also fall off with increasing energy, but they fall off much faster. It can be seen by comparing figure 4.5 with figure 4.2. For example, at the photon energy of 800 a. u., Ne *np* branching ratio is 1.95 while the Ar ratios are about 1.90, thereby indicating that the relativistic effect grows with the nuclear charge. This is expected; as discussed earlier, high-energy dipole matrix elements are generated quite closer to the nucleus. Experiment results for the Ar 2*p* branching ratio range from 100 a. u. to 150 a. u. photon energies demonstrated a good agreement with the RRPA results, both with absolute values and the decrease of the branching ratio with energy, as demonstrated in figure 4.6 [9].

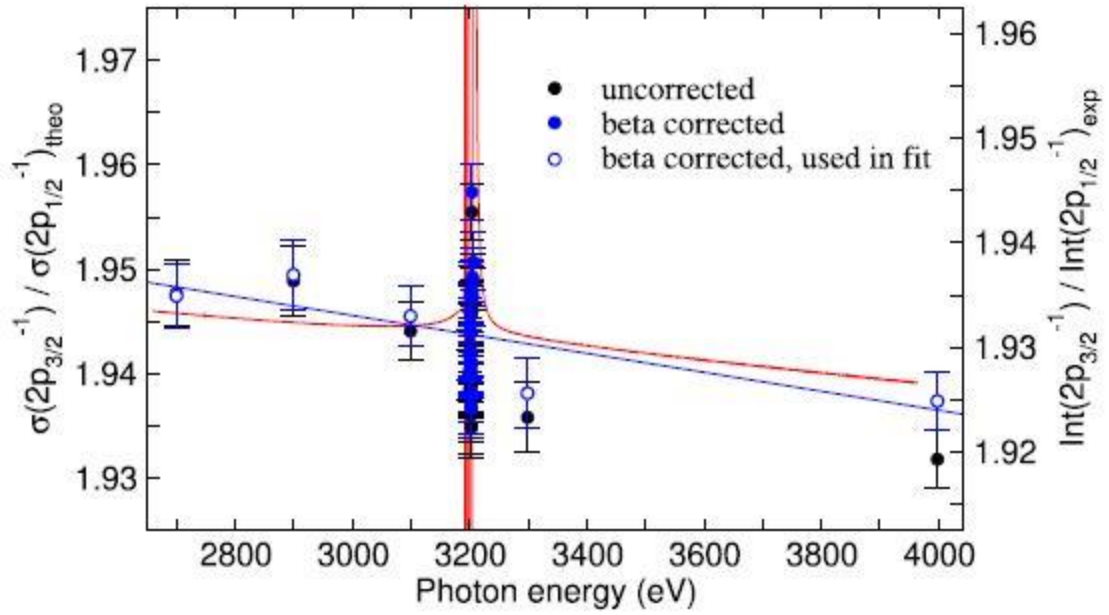

Figure 4.6 Photoionization branching ratio for Ar 2p. The left scale is theory (red). The right scale is experimental intensity (black) and experiment corrected using theoretical angular distribution parameters, β (blue). The blue solid line is a linear fit to the five blue hollow dots. The theoretical data are shifted by 35.3 eV to lower energies in order to match the theoretical and experimental Ar 1s ionization energies [7].

The difference between the fully coupled curves and the curves with coupling only among *np* channels (intrashell coupling) is much more significant for the Ar than in Ne (figure 4.4). Also, it is pervasive over a larger energy range in Ar than in Ne. This indicates that with the increasing

number of electrons, the influence on the *np* branching ratios by other electronic channels is increasing.

Figure 4.7 shows the Ar 2*p* and 3*p* branching ratios in the vicinity of the 1*s* threshold. Similar to the Ne, interchannel coupling effects are exhibited here, but they are about a factor of two smaller than in the Ne case. The 1*s* orbital in Ar is much more compact so that there is almost no overlap with the higher orbitals. Thus the interchannel coupling matrix element is relatively small in this region, and this causes the decrease in the manifestation of interchannel coupling in Ar curves compared to Ne around 1*s* threshold.

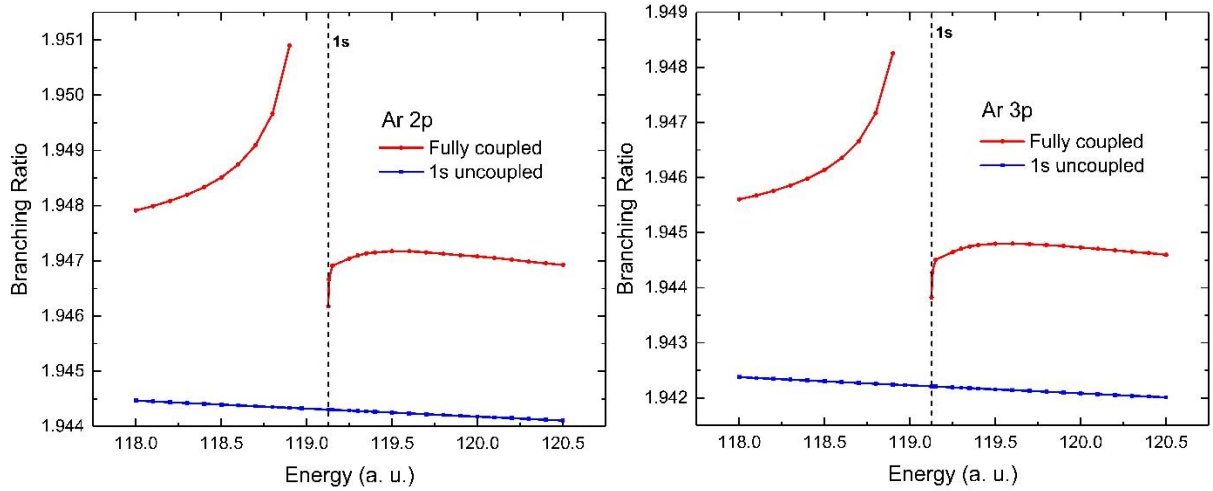

Figure 4.7 Branching ratios of Ar 2p $\left({}^{\sigma_{2p(3/2)}}/_{\sigma_{2p(1/2)}}\right)$ *(right panel) and 3p* $\left({}^{\sigma_{3p(3/2)}}/_{\sigma_{3p(1/2)}}\right)$ *(left panel) calculated with fully coupled (red-dots), and without coupling to 1s channels (blue-squares). The vertical dashed line indicates the 1s threshold.*

In the vicinity of the Ar 2*s* threshold (figure 4.8), the interchannel coupling effect on the branching ratio is small due to two factors; the 2*s* cross section is smaller than the 2*p* cross sections, and the 2*s* threshold is very close to the 2*p* thresholds. Results are somewhat different for the 3*p* branching ratio because the 2*s* threshold is well above the 3*p* thresholds. Thus, while the 2*p* and

3*p* branching ratios are similar at higher energies, they behave differently in the vicinity of the 2*s* threshold owing to the difference of threshold energies.

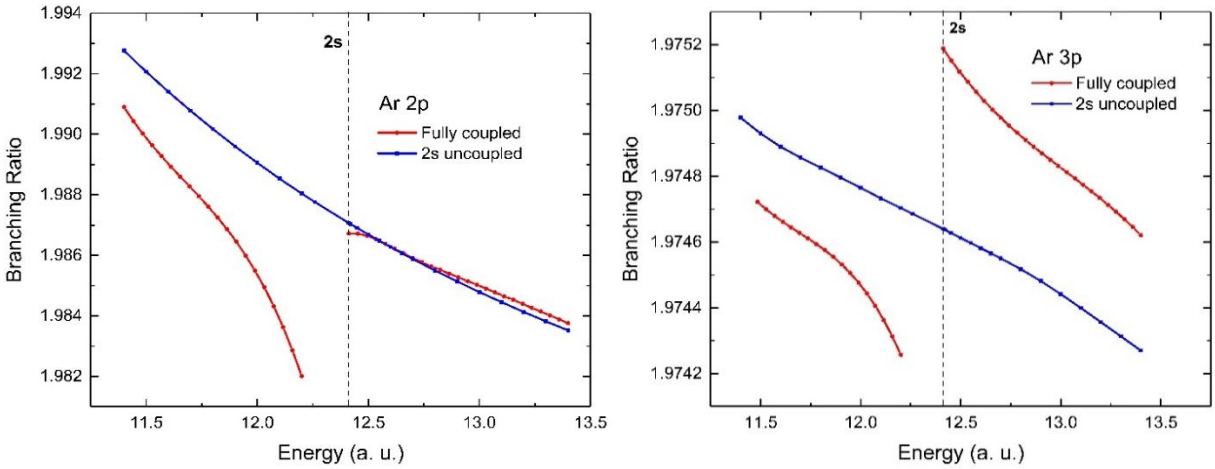

Figure 4.8 Branching ratios of Ar 2p $\left({}^{\sigma_{2p(3/2)}}/_{\sigma_{2p(1/2)}}\right)$ *(right panel) and 3p* $\left({}^{\sigma_{3p(3/2)}}/_{\sigma_{3p(1/2)}}\right)$ *(left panel) calculated with fully coupled (red-dots), and without coupling to 2s channels (blue-squares). The vertical dashed line indicates the 2s threshold.*

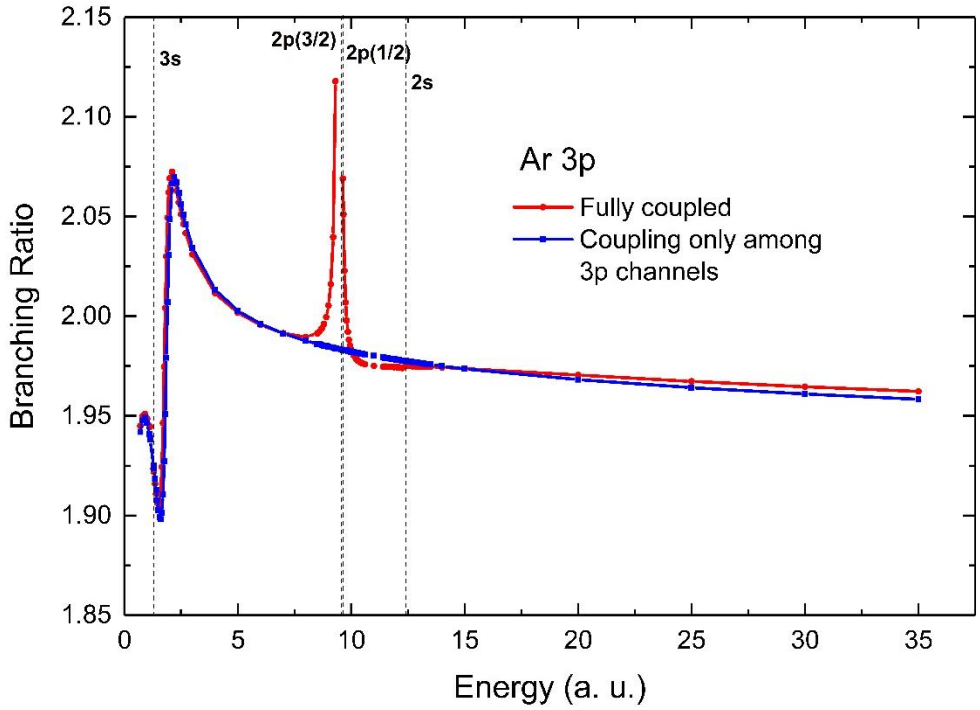

Figure 4.9 Branching ratio of Ar at low energies calculated with fully coupled (red-dots), and with coupling only among 3p channels (blue-squares). The vertical dashed lines indicate the thresholds.

Figure 4.9 shows a close-up of the Ar 3*p* branching ratio at the lower energies. It shows the strong coupling effects of the 3*p* photoionization channels with the 2*p* channels in the vicinity of 2*p* thresholds. The notable variation of 3*p* ratios indicates significant interchannel coupling among *np* channels, and this coupling is strongly affected by relativistic interaction, i. e. strongly *j* dependent. The near-threshold behavior of Ar was discussed earlier [5, 53], and present calculations are in good agreement with them. There are no significant experimental data to be found for the Ar 3*p* branching ratio, probably due to the small splitting (0.177 eV) between 3*p*(3/2) and 3*p*(1/2) doublets.

4.3 Krypton (Kr)

Kr calculations include a total of 29 relativistic channels for all the subshells, 1*s*, 2*s*, 2*p*, 3*s*, 3*p*, 3*d*, 4*s*, and 4*p*. Table 4-3 shows the relativistically and nonrelativistically calculated subshell threshold values of Kr.

Table 4-3 Calculated subshell thresholds of Kr in atomic energy units

Subshell	Threshold (Relativistic)	Threshold (NonRelativistic)
1*s*	529.685	520.159
2*s*	72.080	69.902
2*p*(1/2)	64.875	63.010
2*p*(3/2)	62.879	63.010
3*s*	11.224	10.849
3*p*(1/2)	8.620	8.332
3*p*(3/2)	8.313	8.332
3*d*(3/2)	3.778	3.825
3*d*(5/2)	3.727	3.825
4*s*	1.188	1.153

Since Kr, atomic number (Z =36), is much heavier than the previous two elements discussed, relativistic and nonrelativistic thresholds deviate considerably from each other. With increasing atomic number, the deviation increases because of the enhancement of the relativistic

effect. For Kr, as in the previous cases, outer subshells experience smaller deviation between relativistic and nonrelativistic data due to the shielding of the nucleus by inner subshells. The nonrelativistic values for each member of the n*p* and 3*d* spin-orbit doublets are the same due to the absence of spin-orbit effects. All three elements show that for a specific atom, the spin-orbit splitting decreases with increasing *n* and *l*, while also the splitting increases with *Z*.

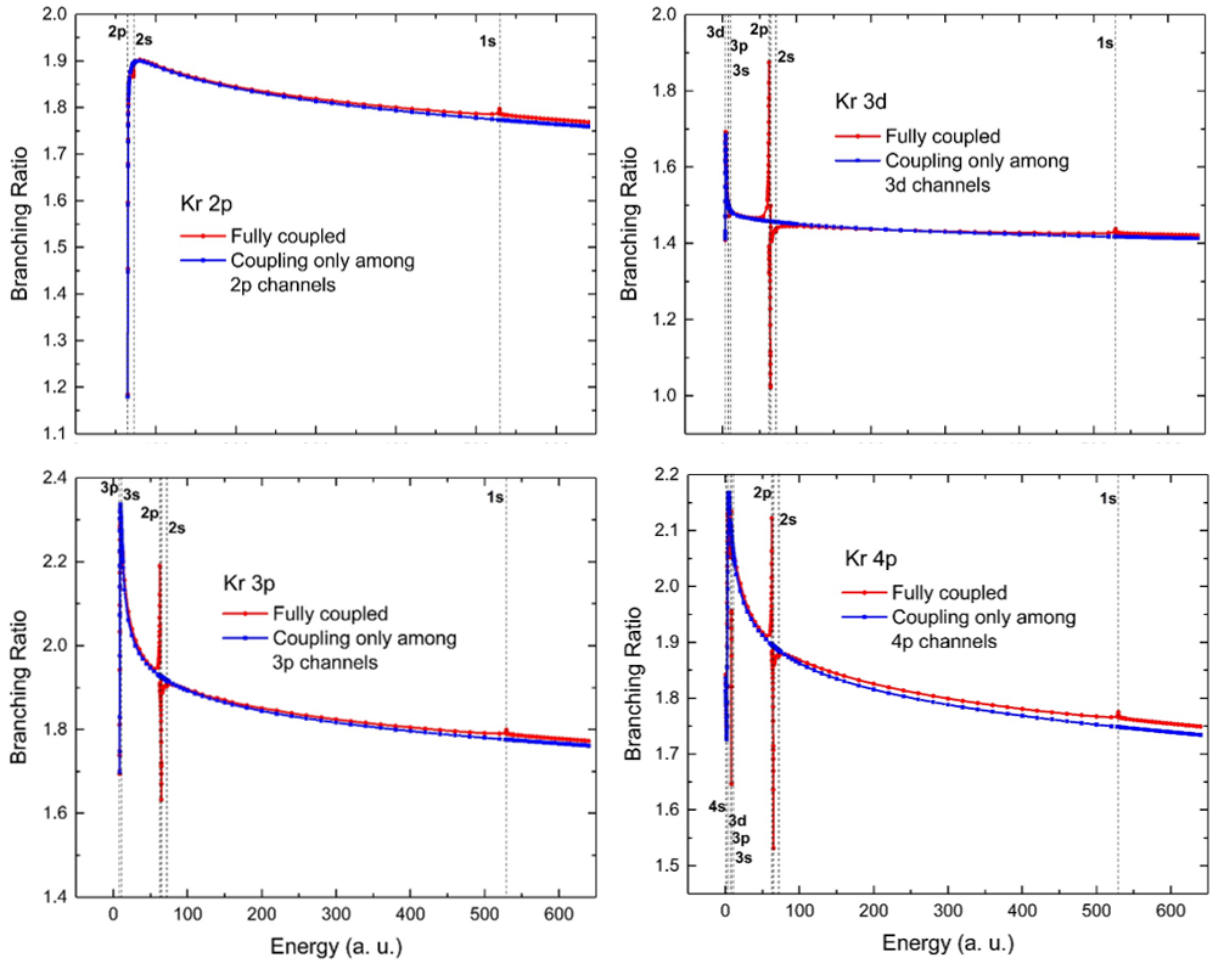

Figure 4.10 Branching ratio of Ar 2p, 3p, 4p $\left(\sigma_{np(3/2)}/\sigma_{np(1/2)}\right)$*, and 3d* $\left(\sigma_{3d(5/2)}/\sigma_{3d(3/2)}\right)$ *calculated with fully coupled (red-dots), and with only intrashell coupling (blue-squares). The vertical dashed lines indicate the thresholds.*

Figure 4.10 shows the overall view of all the Kr branching ratios calculated using RRPA. At the highest energy shown of 640 a. u., the *np* branching ratios are about 1.8, demonstrating that

the Kr *np* branching ratios continue the same trend seen in both Ne and Ar, as that the asymptotic branching ratio decreases with the nuclear charge owing to the increased relativistic effects associated with higher *Z*. Similarly, all the elements show the trend that difference between the fully coupled and intrashell coupled branching ratios increase with the *Z*. This is evidently due to the interchannel coupling with a larger number of photoionization channels.

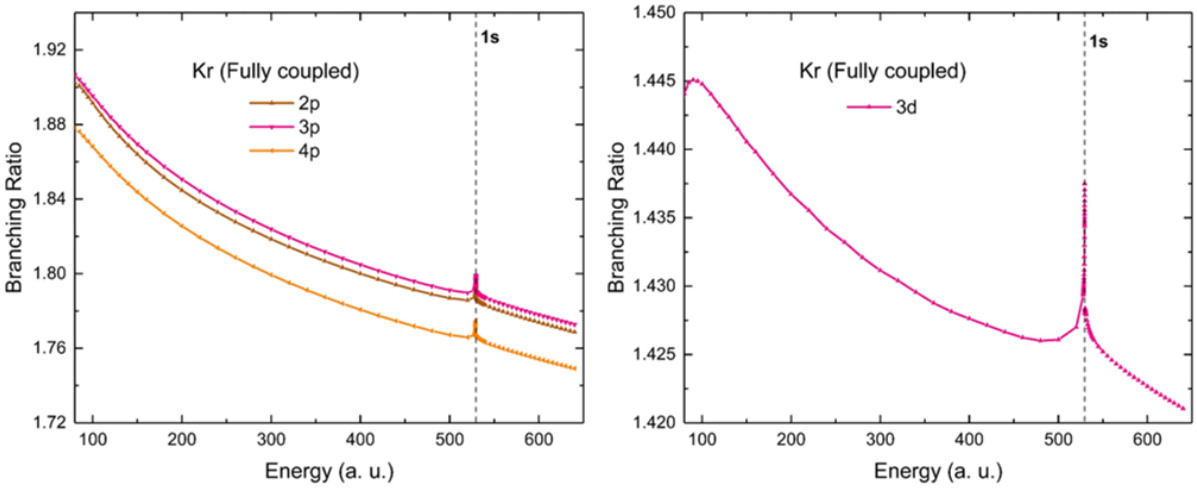

Figure 4.11 Comparison of Kr branching ratios np (2p –brown, 3p –pink, and 4p –orange) (left panel), and 3d (right panel) at high-energy region. The vertical dashed line indicates the 1s threshold.

Figure 4.11 shows a close-up of high-energy behavior of all the branching ratios of Kr. As seen and explained for Ar, the *np* branching ratios are almost independent of the principal quantum number *n* of the initial *np* states. The 3*d* branching ratio is 1.42 at the highest energy of 640 a. u., while its statistical value is 1.5, and it falls off to this value much more slowly than in the *np* case. This demonstrates that for 3*d*, the relativistic effect on the wave function is less significant than the *np* case. This occurs due to the *d*-state centrifugal barrier, which keeps the 3*d* wave function further away from the nucleus than *np* wave functions. Therefore, matrix elements of 3*d* are generated further away from the nucleus where the difference between 3*d*(3/2) and 3*d*(5/2) wave

functions is small. As a result, both the slope of the branching ratio with energy and the deviation from its statistical value are considerably smaller than in the *np* case.

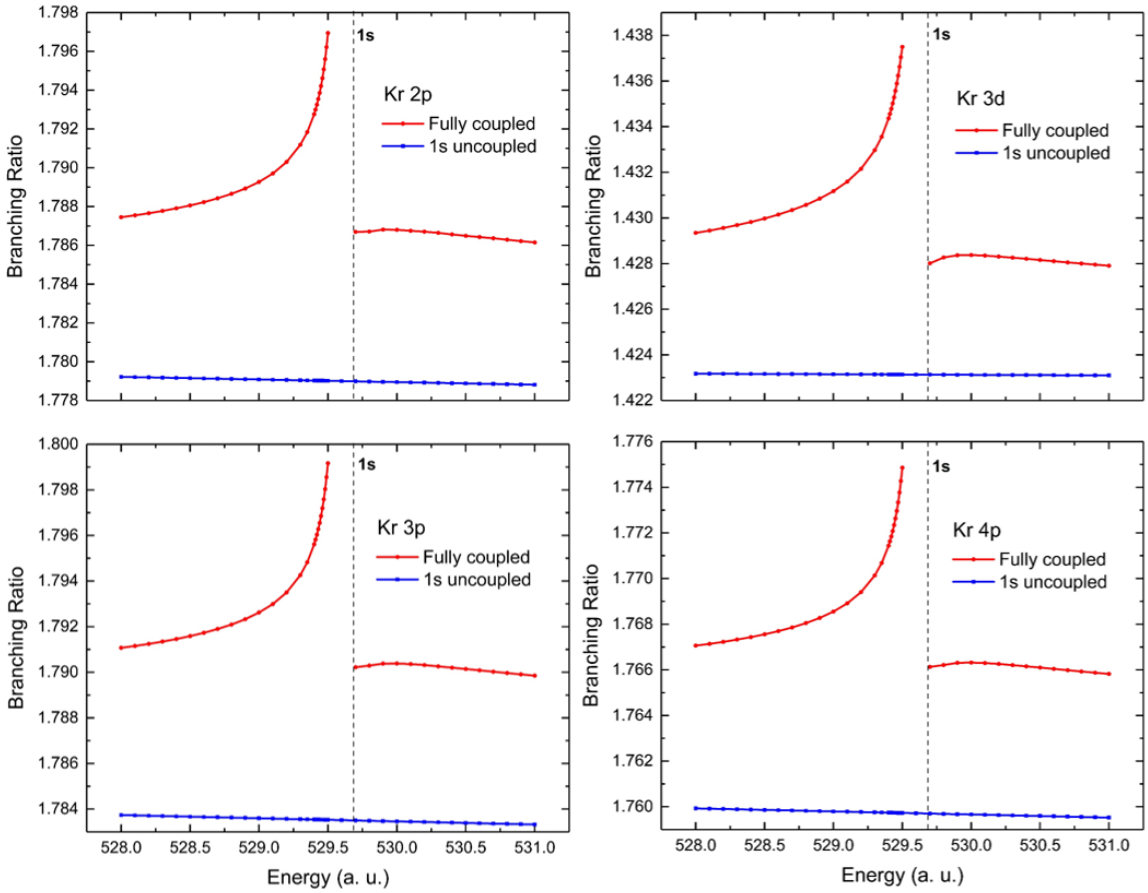

Figure 4.12 Branching ratios of Kr 2p, 3p, 4p $\left(\sigma_{np(3/2)}/\sigma_{np(1/2)}\right)$*, and 3d* $\left(\sigma_{3d(5/2)}/\sigma_{3d(3/2)}\right)$ *calculated with fully coupled (red-dots), and without coupling to 1s channels (blue-squares). The vertical dashed line indicates the 1s threshold.*

Figure 4.12 shows the Kr branching ratios in the vicinity of the 1*s* threshold. Like in the case of Ar, interchannel coupling with the 1*s* channels causes only minimal changes for reasons as discussed in connection with Ar. The changes in the *np* and 3*d* ratios are of about the same size, so there does not appear to be an interchannel coupling angular momentum effect here.

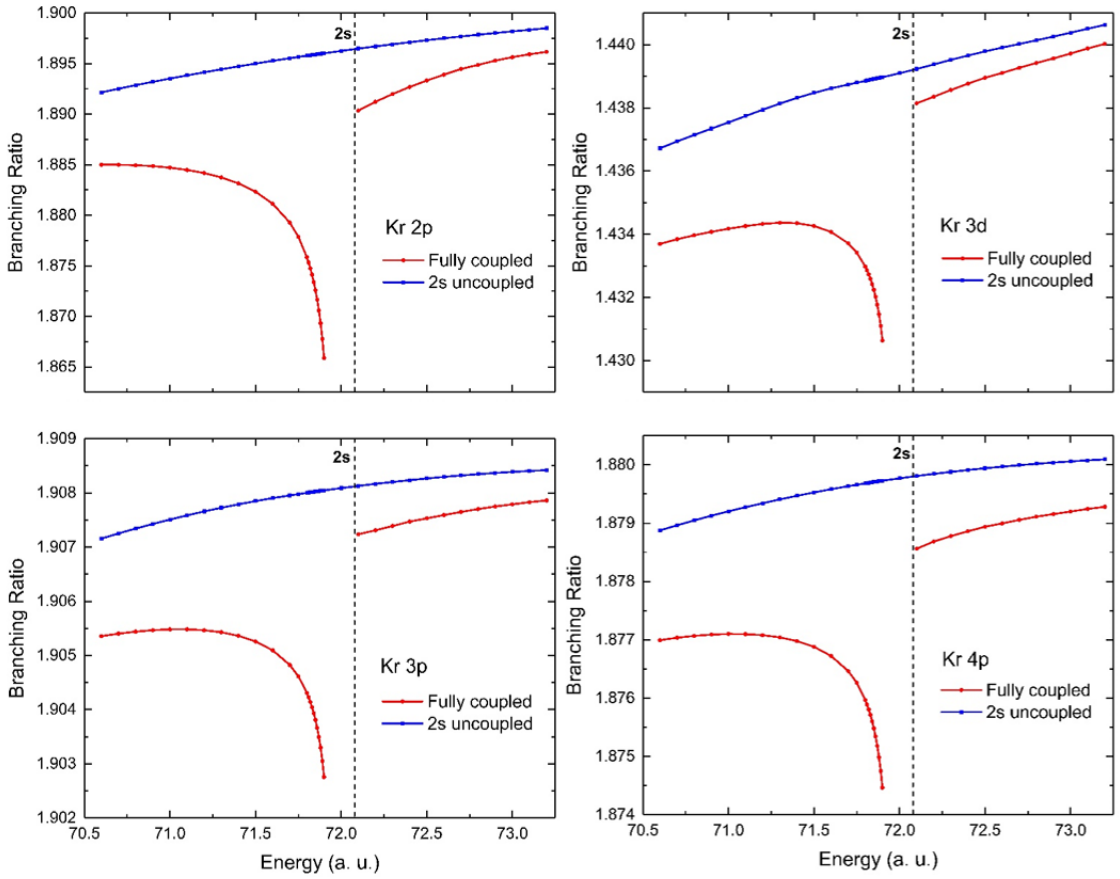

Figure 4.13 Branching ratios of Kr 2p, 3p, 4p $\left(\sigma_{np(3/2)}/\sigma_{np(1/2)}\right)$*, and 3d* $\left(\sigma_{3d(5/2)}/\sigma_{3d(3/2)}\right)$ *calculated with fully coupled (red-dots), and without coupling to 2s channels (blue-squares). The vertical dashed line indicates the 2s threshold.*

Figure 4.13 presents the Kr branching ratios in the neighborhood of the 2*s* threshold. Here the branching ratios are rather different from the 1*s* vicinity, and all of them increasing as a function of energy even without coupling to the 2*s* channels. This seems at odds with the relativistic effect that causes the ratios to decrease with increasing energy. Since earlier works [9, 10] reveal that the interchannel coupling can affect cross sections and therefore branching ratios over a broad range, this phenomenology perhaps results from coupling with other channels.

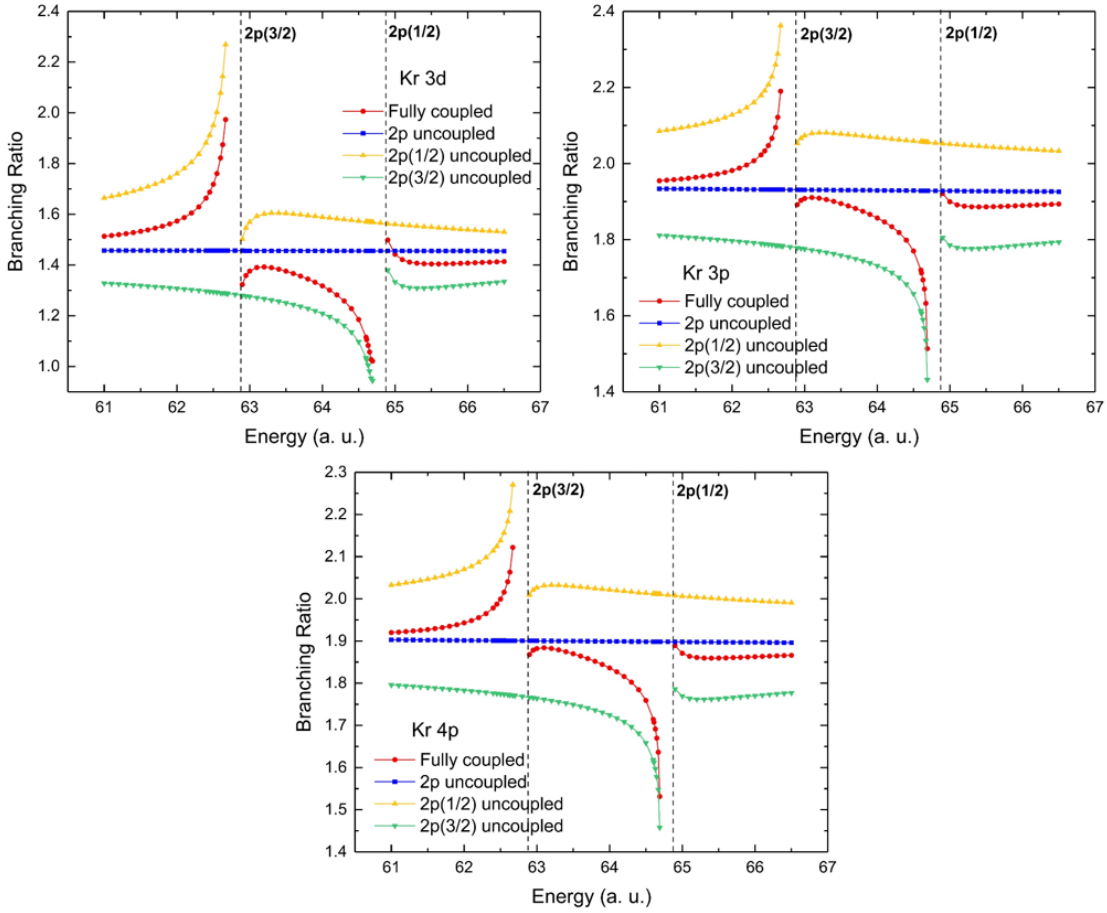

Figure 4.14 Branching ratios of Kr 3d $\left(\sigma_{3d(5/2)}/\sigma_{3d(3/2)}\right)$ *and np* $\left(\sigma_{np(3/2)}/\sigma_{np(1/2)}\right)$ *calculated with fully coupled (red-dots), without coupling to 2p channels (blue-squares), without coupling to 2p(1/2) channels (yellow-triangles), and without coupling to 2p(3/2) channels (green-inverted triangles). The vertical dashed lines indicate the 2p thresholds.*

The branching ratios of Kr in the vicinity of 2*p* thresholds are shown in figure 4.14. Here 2*p* thresholds are sufficiently split to accommodate significant interchannel coupling activities in this region. All the Kr branching ratios, *np*, and 3*d* show a similar pattern around 2*p* thresholds implying that the interchannel coupling effect in this region is independent of the angular momentum. Furthermore, Figure 4.14 includes truncated calculations without coupling all the 2*p* channels and without coupling either one of the spin split channels 2*p*(1/2) or 2*p*(3/2). The coupling

of 2*p* excitation channels dramatically changes the plots, demonstrating the interchannel coupling effect of 2*p* channels on the 3*p*, 4*p* and 3*d* photoionization processes. The structures in the branching ratios are caused solely by the coupling with 2*p* channels since the without coupling of those channels the branching ratios are featureless in this energy region.

Moreover, it is evident from the truncated calculations the coupling with 2*p*(3/2) channels is primarily responsible for the structures around 2*p*(3/2) threshold, and coupling with 2*p*(1/2) channels are mainly responsible for the structures around 2*p*(1/2) threshold. In all of the fully coupled plots, there are a rise and a dip below 2*p*(3/2) and 2*p*(1/2) thresholds correspondingly, and it indicates the Auger resonance has different shapes in the two cases. The drops above the 2*p*(1/2) and the rises above the 2*p*(3/2) thresholds are due to the interchannel coupling with the 2*p* channels since the uncoupled branching ratios are monotonically decreasing in this region.

The calculated branching ratios over an extended range covering both 2*p* and 2*s* thresholds are shown in figure 4.15, and it reveals the source of the peculiar behavior seen around the 2*s* threshold in figure 4.13. Omitting the coupling with both 2*p* and 2*s* channels gives smooth monotone decreasing branching ratios over the entire energy range for all the subshells implying that the coupling with the 2*p* channels causes the branching ratios to rise in the vicinity of the 2*s* threshold. Here the coupling with 2*p* channels is pivotal in the vicinity of the 2*s* threshold, even though 2*p* thresholds are several hundred electron volts away from it. As found in some previous works [9, 10], this behavior of Kr demonstrates that the interchannel coupling with inner shells is not limited to a small energy region around the subshell threshold, but it is operative over a broad energy range.

The 3*d* and 4*p* branching ratios in the vicinity of 3*p* and 3*s* thresholds are given in figure 4.16, and it includes the truncated results in which coupling with the 3*s* and 3*p* channels was

omitted. Coupling effects are pretty small in both plots. But interestingly, the 3*d* branching ratio is monotonically decreasing in both fully coupled and truncated plots except in the resonance regions, even in this low-energy region. The 4*p* branching ratio is larger than its statistical value and increasing. At such low energies all sorts of correlations affect the branching ratios strongly, so that these behaviors are essentially the threshold effects, as seen in figure 4.10.

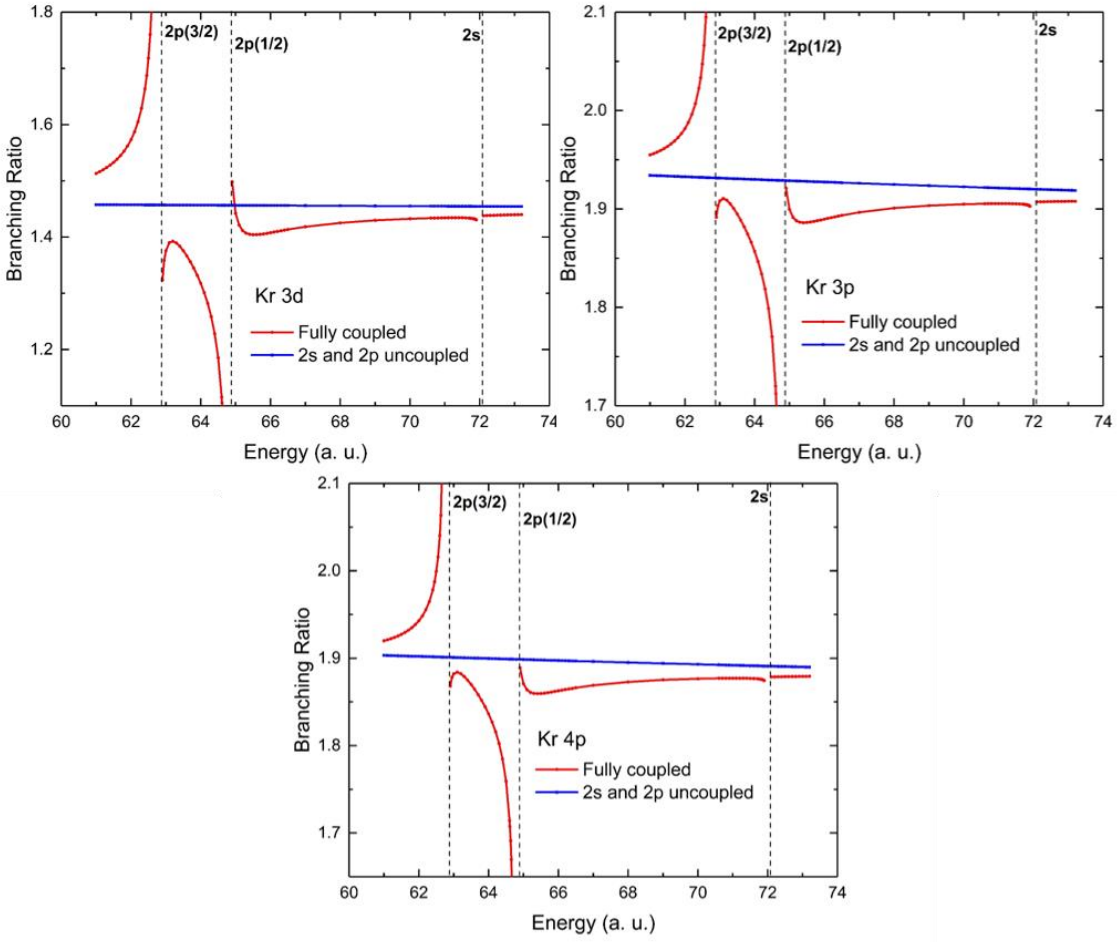

Figure 4.15 Branching ratios of Kr 3d $\left(\sigma_{3d(5/2)}/\sigma_{3d(3/2)}\right)$*, 3p, and 4p* $\left(\sigma_{np(3/2)}/\sigma_{np(1/2)}\right)$ *calculated with fully coupled (red-dots), and without coupling to 2s and 2p channels (blue-squares). The vertical dashed line indicates the thresholds.*

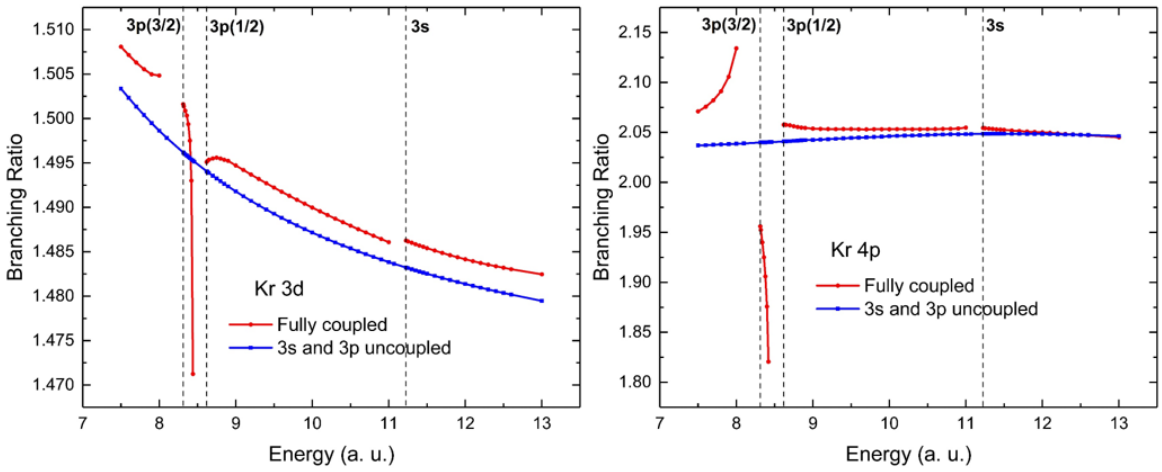

Figure 4.16 Branching ratios of Kr 3d $\left(\sigma_{3d(5/2)}/\sigma_{3d(3/2)}\right)$*, and 4p* $\left(\sigma_{4p(3/2)}/\sigma_{4p(1/2)}\right)$ *calculated with fully coupled (red-dots), and without coupling to 3s and 3p channels (blue-squares). The vertical dashed line indicates the thresholds.*

4.4 Xenon (Xe)

Xe calculations involve a total of 40 relativistic photoionization channels from 2*s*, 2*p*, 3*s*, 3*p*, 3*d*, 4*s*, 4*p*, 4*d*, 5*s*, and 5*p* subshells, leaving out the 1*s* channels. The 1s threshold is deeply bound, over 1200 a. u., and to avoid the RRPA calculation difficulties arising from that, the 1*s* channels were excluded. Since the binding energy of 1*s* is so much higher than the considered energy range, it is essentially irrelevant for the calculations.

Table 4-4 shows the relativistically and nonrelativistically calculated subshell thresholds of Xe. For Xe, atomic number (Z = 54) is much heavier than the atoms considered above and therefore, the relativistic and nonrelativistic thresholds deviate considerably from each other. As noted and explained for the previous cases, in Xe also, outer subshells experiencing smaller deviations between relativistic and nonrelativistic calculations and the nonrelativistic energies for

np and *nd* spin-orbit doublets are the same. All the elements show that for a specific atom, the spin-orbit splitting decreases with increasing *n* and *l*, while the splitting increases with *Z*.

Table 4-4 Calculated subshell thresholds of Xe in atomic energy units

Subshell	Threshold (Relativistic)	Threshold (NonRelativistic)
1*s*	1277.256	1224.353
2*s*	202.465	189.335
2*p*(1/2)	189.680	177.783
2*p*(3/2)	177.705	177.783
3*s*	43.010	40.175
3*p*(1/2)	37.660	35.222
3*p*(3/2)	35.325	35.222
3*d*(3/2)	26.023	26.119
3*d*(5/2)	25.537	26.119
4*s*	8.430	7.856
4*p*(1/2)	6.453	6.008
4*p*(3/2)	5.983	6.008

The overall views of the 2*p*, 3*p*, 4*p*, 5*p*, 3*d* and 4*d* of branching ratios for Xe are depicted in figure 4.17. Considering all the elements studied so far, the asymptotic branching ratios decrease with nuclear charge owing to the increased relativistic effect with higher *Z*. At the highest energy point, 500 a. u., *np* branching ratios for Xe are in the range of 1.61 – 1.68, continuing this trend. However, the difference between the branching ratios of fully coupled and ones with coupling only among particular subshells (intrashell coupling) is slightly smaller for Xe than in Kr, reversing the trend seen in Ne, Ar, and Kr. This alteration occurs due to very complicated interactions of interchannel coupling, which can increase or decrease cross sections; with so many different interchannel coupling interactions in Xe, some of them apparently partially cancel out.

As seen and explained in both Ar and Kr, high-energy branching ratios are highly independent of the principal quantum number *n* of the initial *np* or *nd* state, as shown in figure 4.18.

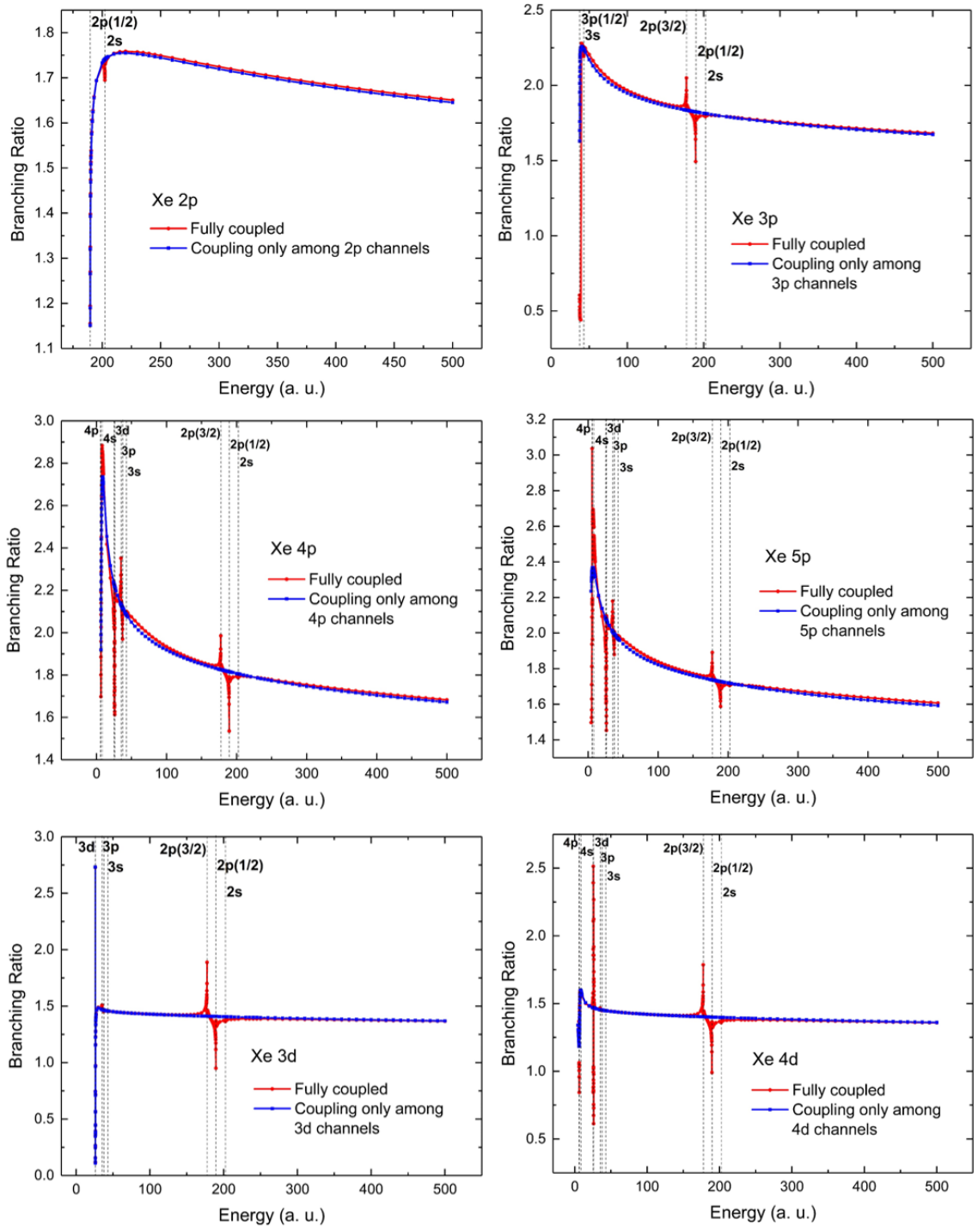

Figure 4.17 Branching ratio of Xe 2p, 3p, 4p, 5p $\left({}^{\sigma_{np(3/2)}}/_{\sigma_{np(1/2)}}\right)$*, 3d, and 4d* $\left({}^{\sigma_{3d(5/2)}}/_{\sigma_{3d(3/2)}}\right)$ *calculated with fully coupled (red-dots), and with only intrashell coupling (blue-squares). The vertical dashed lines indicate the thresholds.*

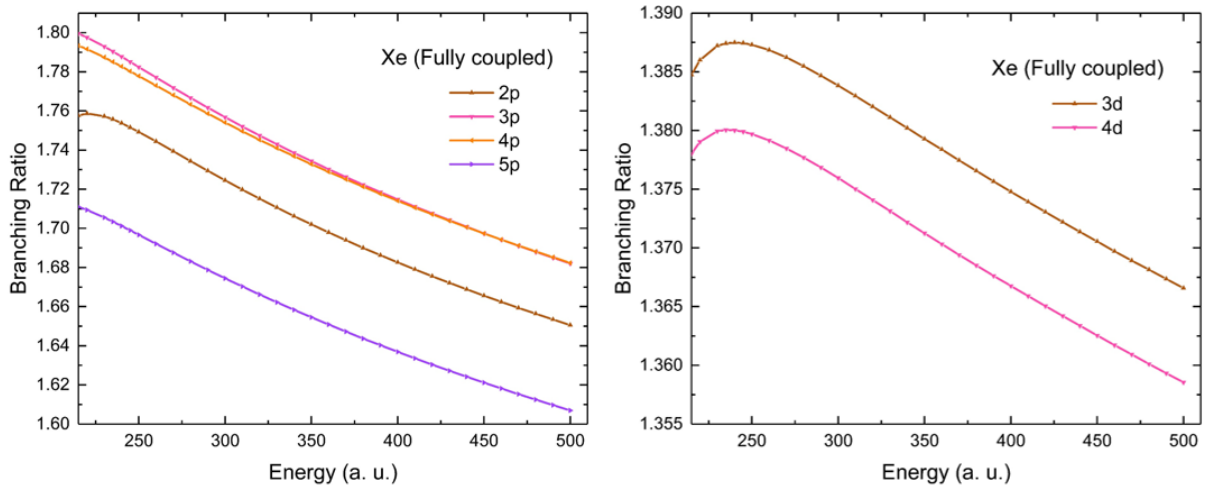

Figure 4.18 Comparison of Xe branching ratios np (2p –brown, 3p –pink, 4p – orange, and 5p –purple) (left panel), and nd (3d –brown and 4d –pink) (right panel) at high-energy region.

The *nd* branching ratios of Xe (the statistical value is 1.5) at 500 a. u. is about 1.36 and somewhat lower than in the Kr as expected. Furthermore, Xe *nd* branching ratio also falls off slower than that of *np* as in Kr. It shows that the relativistic effects on the *nd* wave functions are smaller than that on *np*.

In the vicinity of inner-shell thresholds, there are large excursions of Xe plots from their smooth behavior. To explore this phenomenon, first Xe branching ratios in the vicinity of $n = 2$ thresholds were plotted in figure 4.19. Without the coupling of $n = 2$ channels, the branching ratios are monotonically decreasing, thereby showing that the structures are due to the coupling. Here the phenomenology is similar to the Kr around $n = 2$ threshold region (figure 4.15) and for the same reasons.

Figure 4.20 shows the experimental (red) and theoretical (black) Xe 3*d* and 4*d* branching ratios in the vicinity of $n = 2$ thresholds [9]. Here the experimental trends follow the theoretically calculated behavior of the branching ratios with good agreement between theory and experiment.

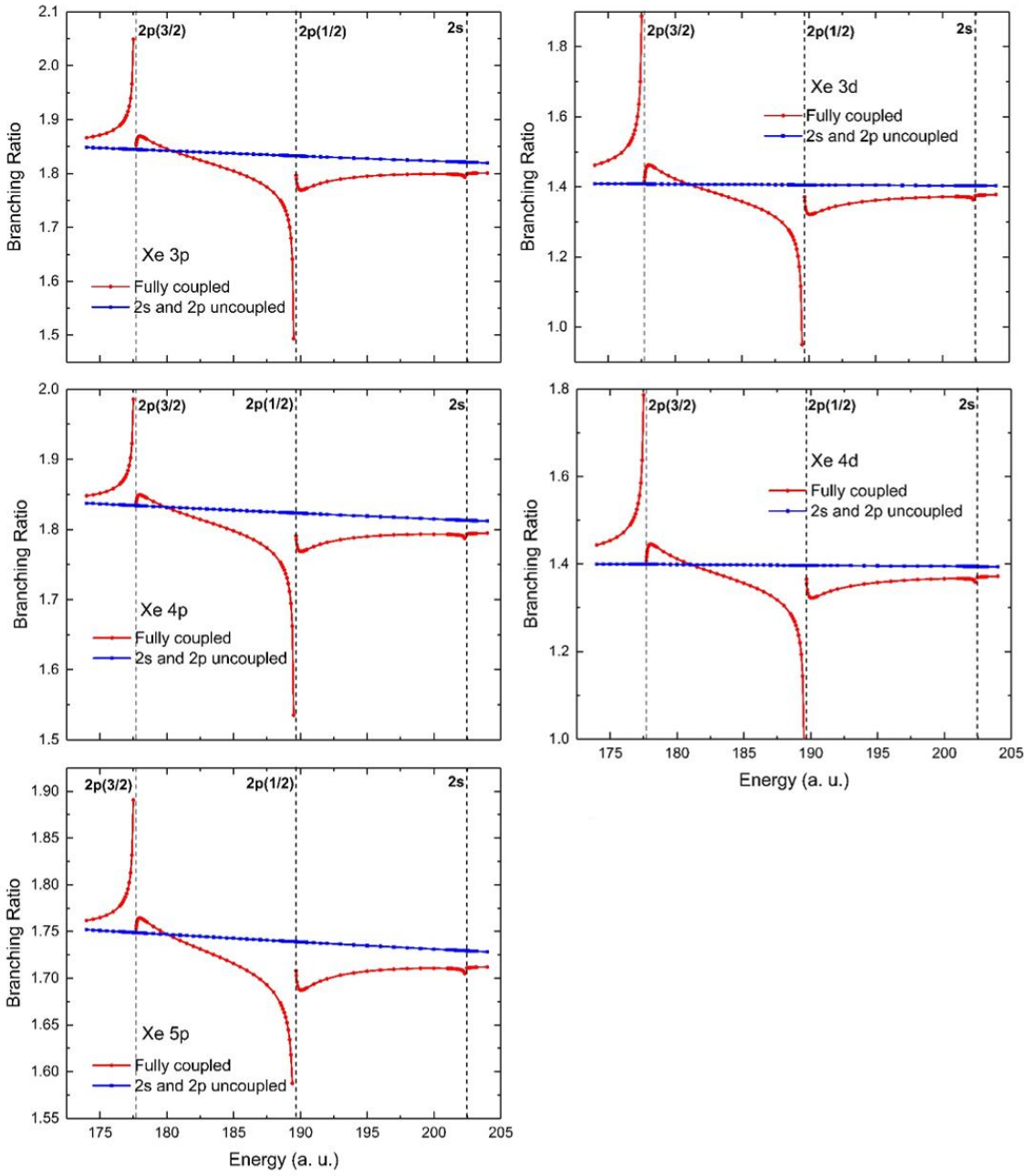

Figure 4.19 Branching ratios of Xe 3d, 4d $\left(\sigma_{3d(5/2)}/\sigma_{3d(3/2)}\right)$*, 3p, 4p, and 5p* $\left(\sigma_{np(3/2)}/\sigma_{np(1/2)}\right)$ *calculated with fully coupled (red-dots), and without coupling to 2s and 2p channels (blue-squares). The vertical dashed lines indicate the thresholds.*

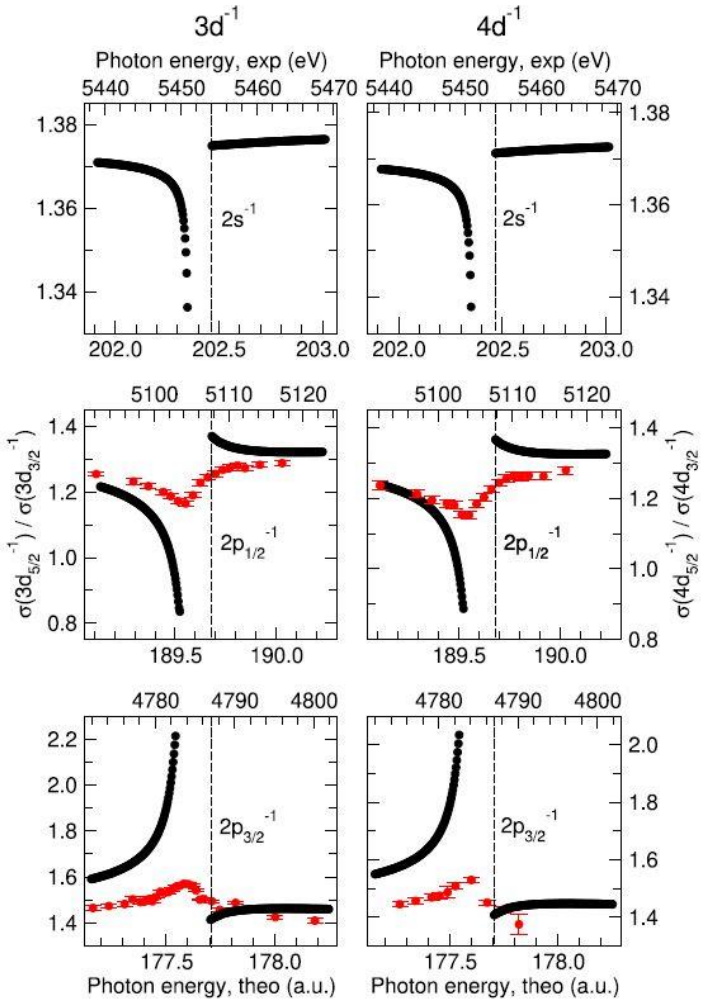

Figure 4.20 Xe 3d and 4d photoionization branching ratios in the vicinity of the n = 2 thresholds. Experiment (red), theory (black). The experimental and theoretical energy scales are shifted relative to each other so that the respective ionization energies are located at the dashed vertical lines [7].

The Xe 4*p*, 5*p*, 3*d*, and 4*d* branching ratios in the neighborhood of the $n = 3$ (3*s* and 3*p*) thresholds are shown in figure 4.21. Qualitatively, the trend of all the branching ratios is the same around both sets of thresholds $n = 2$ and $n = 3$. As in the case of Kr, in all the plots of Xe, there is a rise and then a drop below *np*(3/2) and *np*(1/2) thresholds correspondingly, indicating that the resonance has different shapes around the spin-orbit doublets of the inner *np* subshells. Notably, in both regions, the structures in branching ratios are not only the same for states with the same

initial angular momentum independent of *n*, but also structures in both *p* and *d* plots are similar. Therefore, it appears to be that the interchannel coupling similarly affects *np* and *nd* states independent of *l*. Kr showed similar behavior, but we have no obvious explanation for this. However, the excursion from the smooth background of plots around $n = 3$ thresholds is smaller in magnitude than around $n = 2$ thresholds, indicating the interchannel coupling is less relativistic for $n = 3$ case than in $n = 2$ case. This occurs because the 3*s* and 3*p* wave functions are less relativistic than their $n = 2$ counterparts owing to their very different binding energies (the binding energies for 2*p* and 2*s* are about 200 a. u. while that of 3*p* and 3*s* are about 40 a. u.). Also, the spin-orbit splitting decreases with increasing *n* for both *p* and *d* subshells.

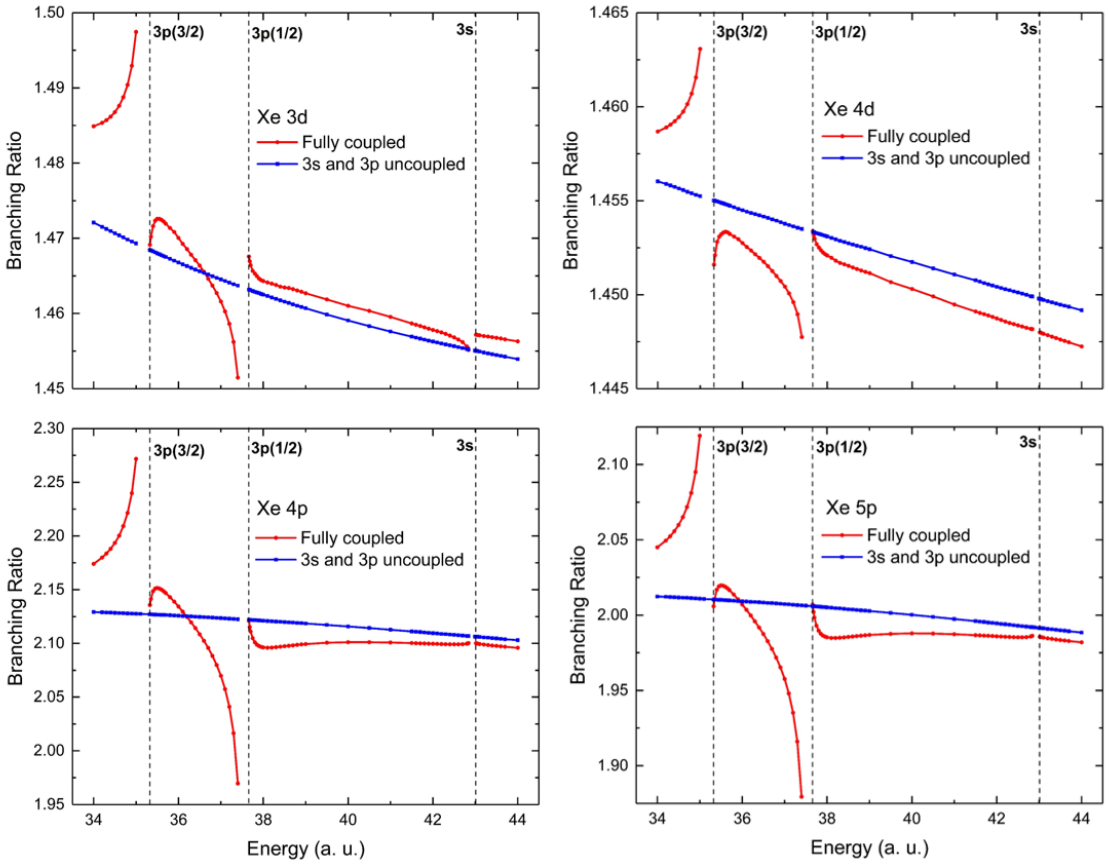

Figure 4.21 Branching ratios of Xe 3d, 4d $\left(\sigma_{3d(5/2)}/\sigma_{3d(3/2)}\right)$*, 4p, and 5p* $\left(\sigma_{np(3/2)}/\sigma_{np(1/2)}\right)$ *calculated with fully coupled (red-dots), and without coupling to 3s and 3p channels (blue-squares). The vertical dashed lines indicate the thresholds.*

As discussed in the Kr case, for Xe also, interchannel coupling affects the branching ratios over a broad energy range, not just around the subshell thresholds. Moreover, Xe also exhibits the peculiar increase of branching ratios with the energy around *ns* thresholds, as opposed to the expected relativistic decrease, due to the interchannel coupling of corresponding *np* channels.

The branching ratios of Xe in the vicinity of the 3d thresholds are depicted in figure 4.22, and they are particularly interesting because of the unusual structures in the curves. The sharp variations in the branching ratios are caused solely by the coupling with 3*d* channels because without coupling of those channels gives featureless plots.

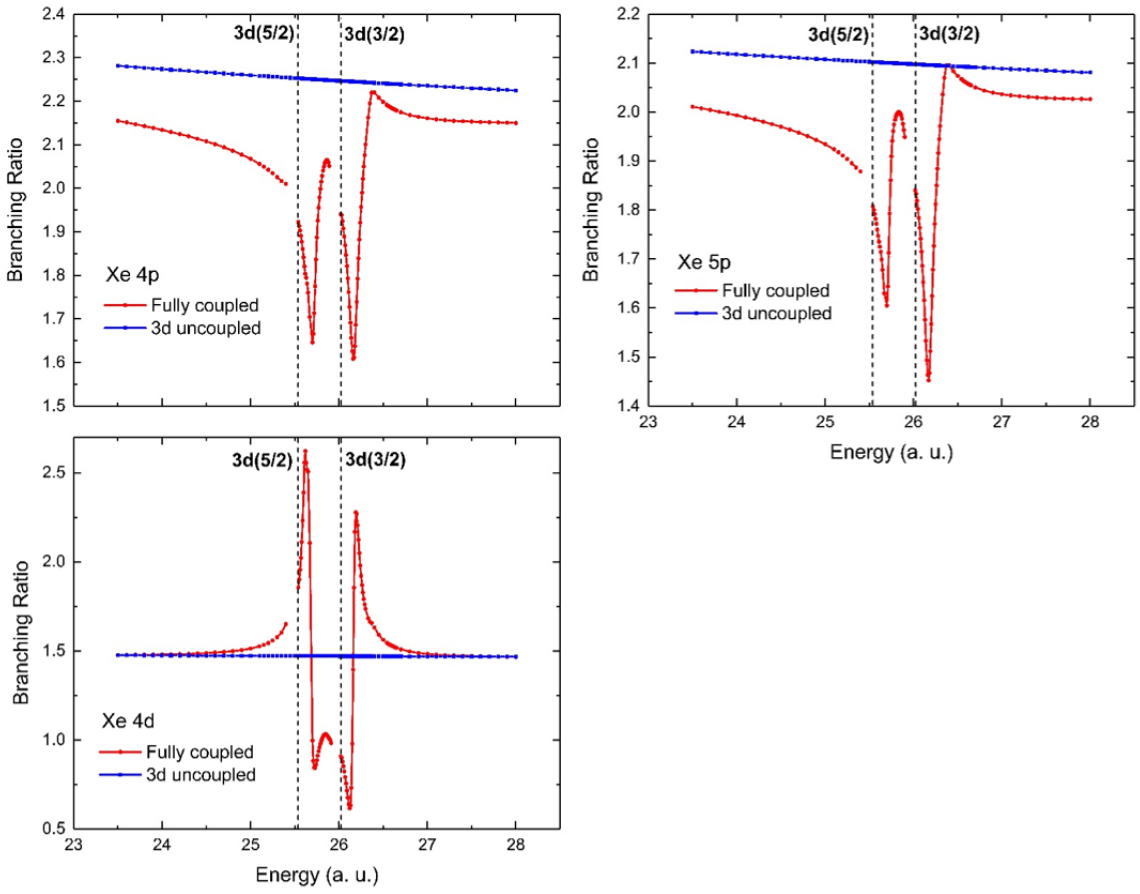

Figure 4.22 Branching ratios of Xe 4p, 5p $\left({}^{\sigma_{np(3/2)}}/_{\sigma_{np(1/2)}}\right)$*, and 4d* $\left({}^{\sigma_{3d(5/2)}}/_{\sigma_{3d(3/2)}}\right)$ *calculated with fully coupled (red-dots), and without coupling to 3d channels (blue-squares). The vertical dashed lines indicate the 3d thresholds.*

Around Xe 3*d* thresholds, branching ratio curves follow a different pattern than in the vicinity of *np* thresholds. Moreover, all the branching ratios follow a similar trend around the *np* threshold, while around 3*d* thresholds, *np,* and *nd* branching ratio curves follow somewhat different patterns. Therefore, unlike in other cases, the effect of the interchannel coupling with 3*d* subshells is dependent on the angular momentum.

In the neighborhood of 3*d* thresholds, fully coupled *np* branching ratios vary about 0.6 within a small energy range, from 1.6 to 2.2 for 4*p* and from 1.5 to 2.1 for 5*p*. Moreover, the variation of the 4*d* branching ratio in the same small energy range is much more significant than *np*, about 2.0 from 0.6 to 2.6. Thus, the interchannel coupling is much more important in 4*d* case than in *np* cases in this region. It happens for this particular situation because the angular part of the interchannel coupling matrix element is larger in between channels of the same angular momenta than between channels of different angular momenta while, in the present case, the radial parts are about the same.

To understand huge variations in this region, the individual cross sections of the spin-orbit doublets of Xe 3*d* were examined. Figure 4.23 shows the cross section and branching ratio for the Xe 3*d* subhells. As in figure 4.23 left panel, the 3*d* cross sections show sharp maxima above the thresholds. Those maxima are shape resonance or delayed maxima and were discovered many years ago [54]. In addition, the Xe 3*d*(5/2) cross section exhibits an extra small peak at the energy of the 3*d*(3/2) shape resonance maximum. This phenomenon was first discovered experimentally [55] and subsequently explained theoretically [13, 56, 57]. It is known as spin-orbit interaction activated interchannel coupling (SOIAIC). Briefly, owing to the spin-orbit splitting of the 3*d* threshold, the 3*d*(3/2) delayed maximum occurs at an energy where the 3*d*(5/2) cross section is small, thereby transferring oscillator strength to the much smaller 3*d*(5/2) cross section via

interchannel coupling and, as a result, an extra peak can be seen in the 3*d*(5/2) cross section at about 26.2 a.u. This can be also seen in the branching ratio plots (figure 4.23 – right panel) as a small bump of fully coupled curve at the same energy.

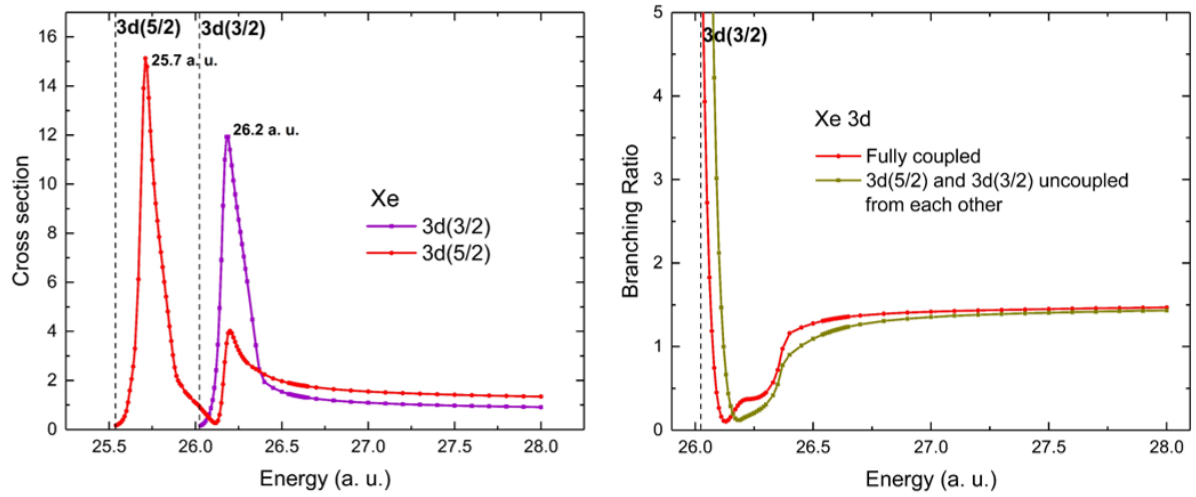

Figure 4.23 Calculated Xe 3d cross sections, 3d(3/2) (purple) and 3d(5/2) (red) – left panel and branching ratios, fully coupled (red) and 3d(5/2) and 3d(3/2) uncoupled from each other – right panel. The vertical dashed lines indicate the 3d thresholds.

Calculated cross sections for *np* and *nd* subshells around 3*d* thresholds are plotted to further understand the above phenomenon, shown in figure 4.24. Let us first focus on the 4*d* case. As seen from figure 4.24, The maxima in the 3*d* cross sections are two orders of magnitude larger than the 4*d* cross sections, thus creating the conditions for significant changes to 4*d* cross sections via interchannel coupling. This interchannel coupling creates structures in the 4*d* cross section at the same energies where the maxima in the 3*d* cross sections (figure 4.23). Moreover, the manifestation of the interchannel coupling in the 4*d* cross sections is different for two spin-orbit doublets. This difference indicates that the interchannel coupling matrix elements are strongly *j*-dependent; said another way, photoionization in this energy region is strongly affected by

relativistic interactions. The significant difference in cross sections explains the variations in 4*d* branching ratios in the vicinity of 3*d* thresholds.

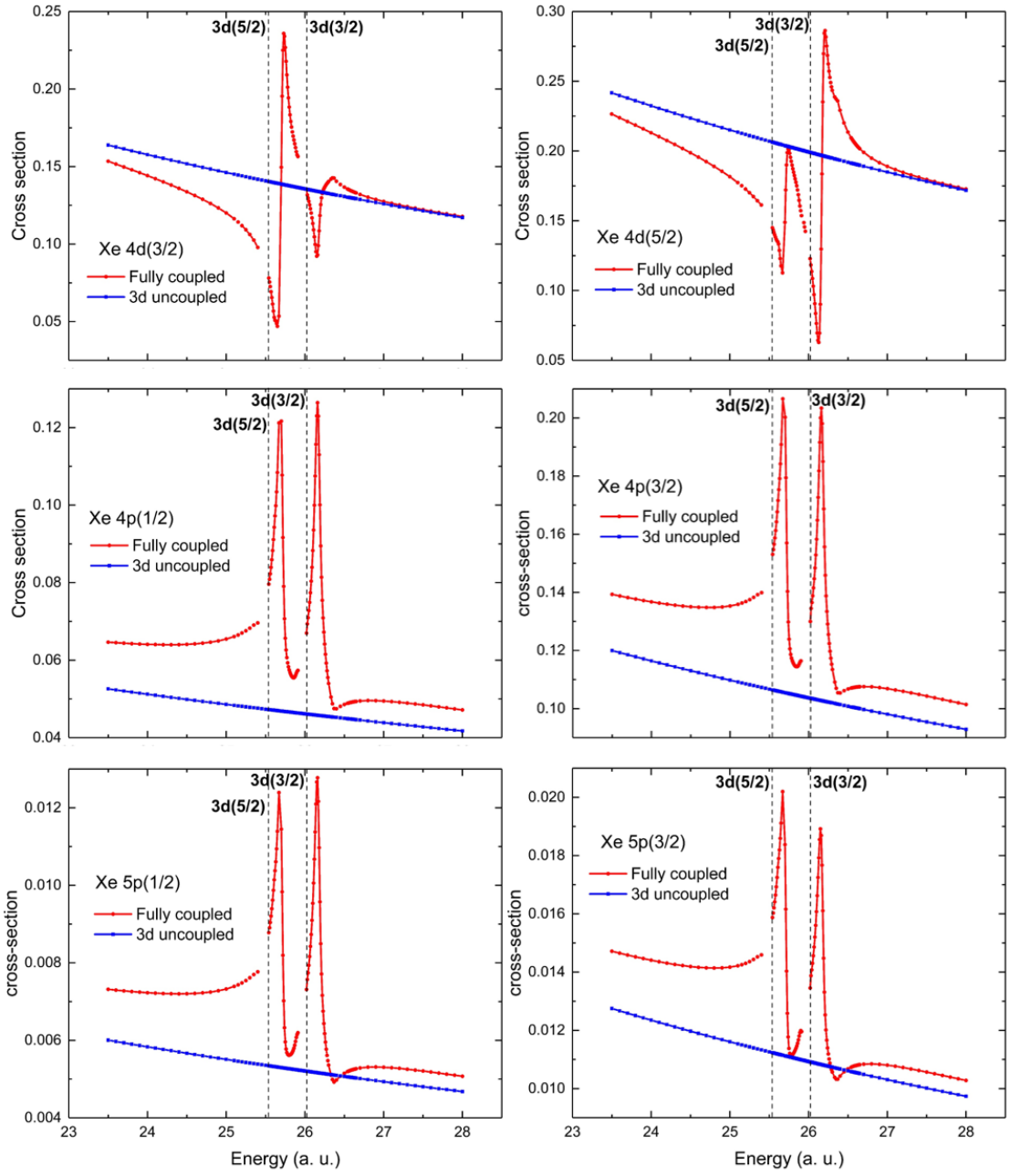

Figure 4.24 Calculated Xe 4d, 4p, and 5p cross sections, fully coupled (red) and without coupling to 3d channels (blue-squares). The vertical dashed lines indicate the 3d thresholds.

The features in the Xe 4*p* and 5*p* branching ratios are also located at the exact photon energies as in 4*d*, where the peaks of 3*d* cross sections appeared (figures 4.23 and 4.24). Therefore, the explanation for the huge variations in Xe 4*p* and 5*p* branching ratios is essentially the same as for the 4*d* case, although the details differ somewhat.

Figure 4.25 shows the 4*d* and 5*p* branching ratios in the vicinity of 4*p* and 4*s* thresholds. According to those plots, the interchannel coupling effect is relatively small except for the resonance region just below 4*p* thresholds. Above the 4*p*(1/2) threshold, the 5*p* branching ratio shows a small effect, while the 4*d* branching ratio shows no effect at all. It further indicates that the interchannel coupling interaction between outer and inner subshells is strongest between channels of the same angular momentum than in channels of different angular momentum.

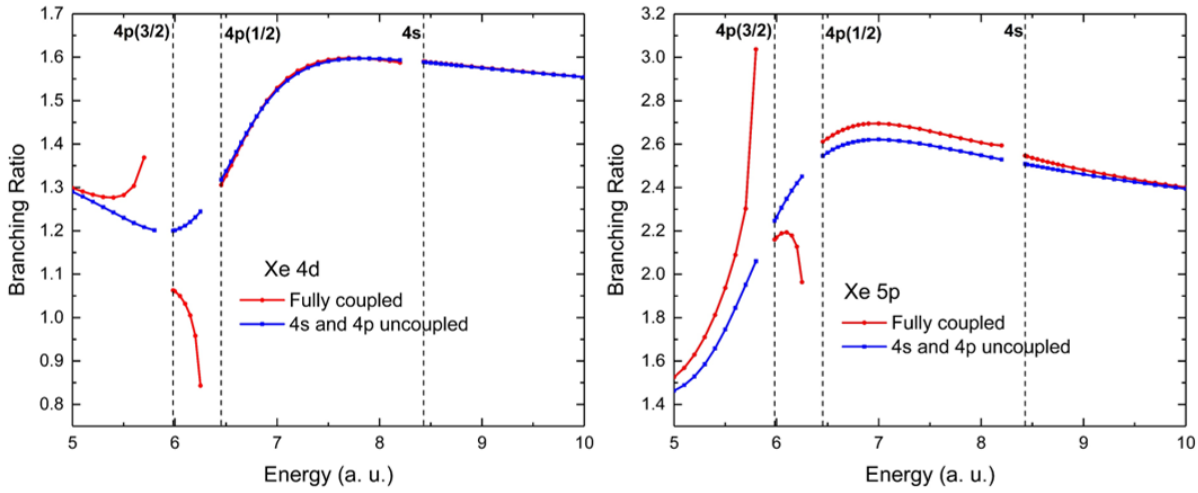

Figure 4.25 Branching ratios of Xe 4d $\left(\sigma_{3d(5/2)}/\sigma_{3d(3/2)}\right)$*, and 5p* $\left(\sigma_{np(3/2)}/\sigma_{np(1/2)}\right)$ *calculated with fully coupled (red-dots) and without coupling to 4s and 4p channels (blue-squares). The vertical dashed lines indicate the 4s and 4p thresholds.*

4.5 Mercury (Hg)

Mercury atoms have a closed-shell structure, and it is a transition metal. So far, all the elements studied are noble gasses. There is a lack of experimental studies about Hg because of the difficulty arising from the damage made on experimental setups by its evaporation. To fill this gap and to identify the variation of other elements from the trends we found on noble gasses, subshell photoionization probabilities of Hg were studied in this research. Hg calculations involve a total of 47 relativistic photoionization channels from 3*s*, 3*p*, 3*d*, 4*s*, 4*p*, 4*d*, 5*s*, 5*p*, 5*d*, and 6*s* subshells except 1*s*, 2*s*, and 2*p* channels. As discussed in the section of Xe, those channels were excluded to avoid the RRPA calculation difficulties. Since the binding energies of those subshells are much higher than the considered energy range, they are essentially irrelevant for the present calculations.

Table 4-5 Calculated subshell thresholds of Hg in atomic energy units

Subshell	Threshold (Relativistic)	Threshold (NonRelativistic)
1*s*	3074.231	2778.402
2*s*	550.252	470.404
2*p*(1/2)	526.855	452.182
2*p*(3/2)	455.157	452.182
3*s*	133.113	113.130
3*p*(1/2)	122.639	104.341
3*p*(3/2)	106.545	104.341
3*d*(3/2)	89.437	88.146
3*d*(5/2)	86.020	88.146
4*s*	30.648	25.572
4*p*(1/2)	26.124	21.670
4*p*(3/2)	22.189	21.670
4*d*(3/2)	14.797	14.610
4*d*(5/2)	14.053	14.610

Table 4-5 shows the relativistically and nonrelativistically calculated subshell thresholds of Hg. Hg ($Z = 80$) is much heavier than the previous elements studied, and therefore the relativistic and nonrelativistic thresholds deviate considerably from each other. As noted and explained in connection with the previous elements, in Hg also, thresholds of outer subshells experience smaller

deviation from nonrelativistical values than inner subshells. For Hg also, the spin-orbit splitting decreases with the increasing *n* and *l*.

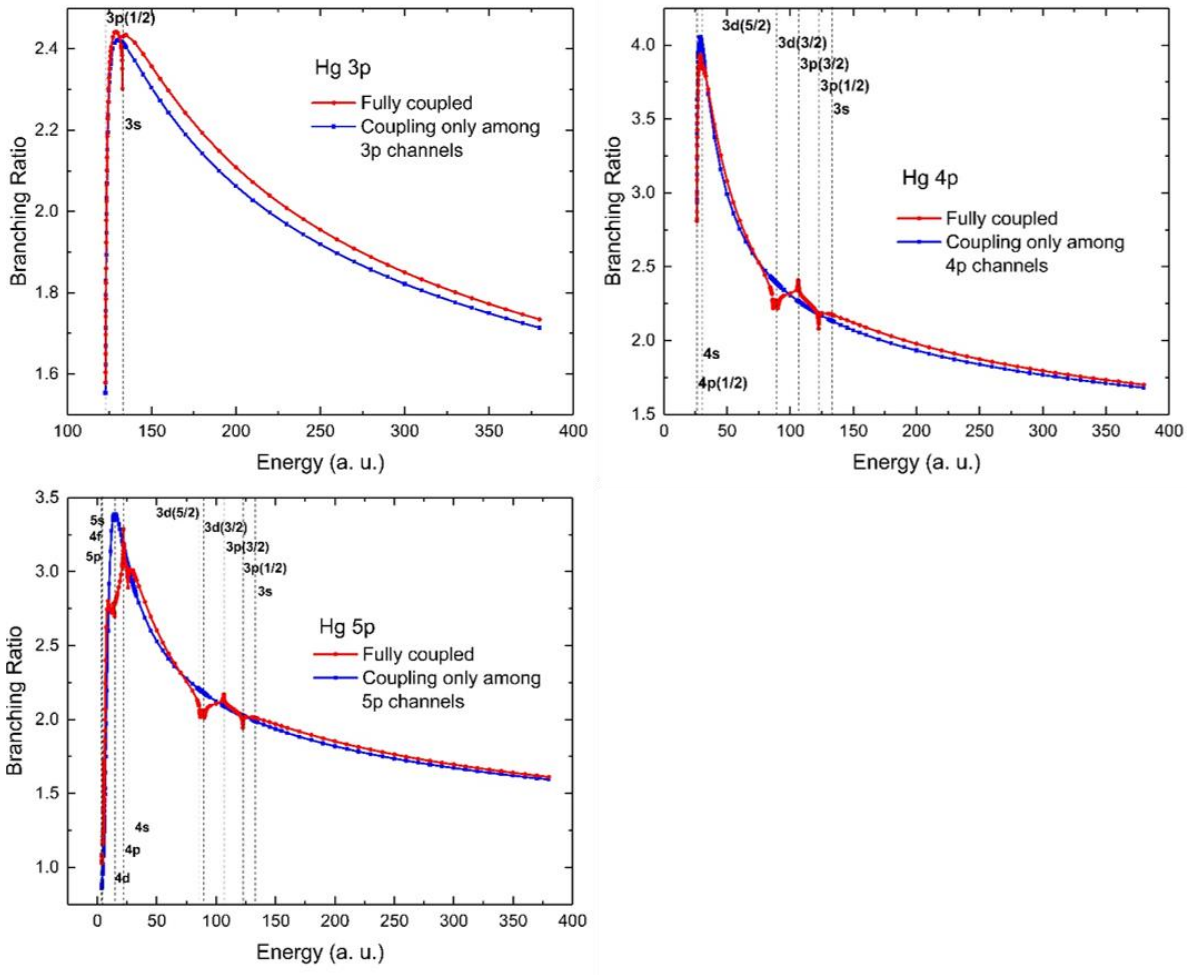

Figure 4.26 Branching ratio of Hg 3p, 4p, and 5p $\left({}^{\sigma_{np(3/2)}}/_{\sigma_{np(1/2)}}\right)$ *calculated with fully coupled (red-dots), and with only intrashell coupling (blue-squares). The vertical dashed lines indicate the thresholds.*

The overall views of Hg branching ratios of the *np* (3*p*, 4*p*, 5*p*), *nd* (3*d*, 4*d*, 5*d*), and 4*f* are depicted in figures 4.26 and 4.27 respectively. The asymptotic branching ratios of Hg are lower than other elements owing to the increased relativistic effect with higher *Z*. The difference between the branching ratios of fully coupled and intrashell coupled is slightly larger for Hg than in Xe,

following the same trend seen in Ne, Ar, and Kr except in Xe due to very complicated interactions of interchannel coupling.

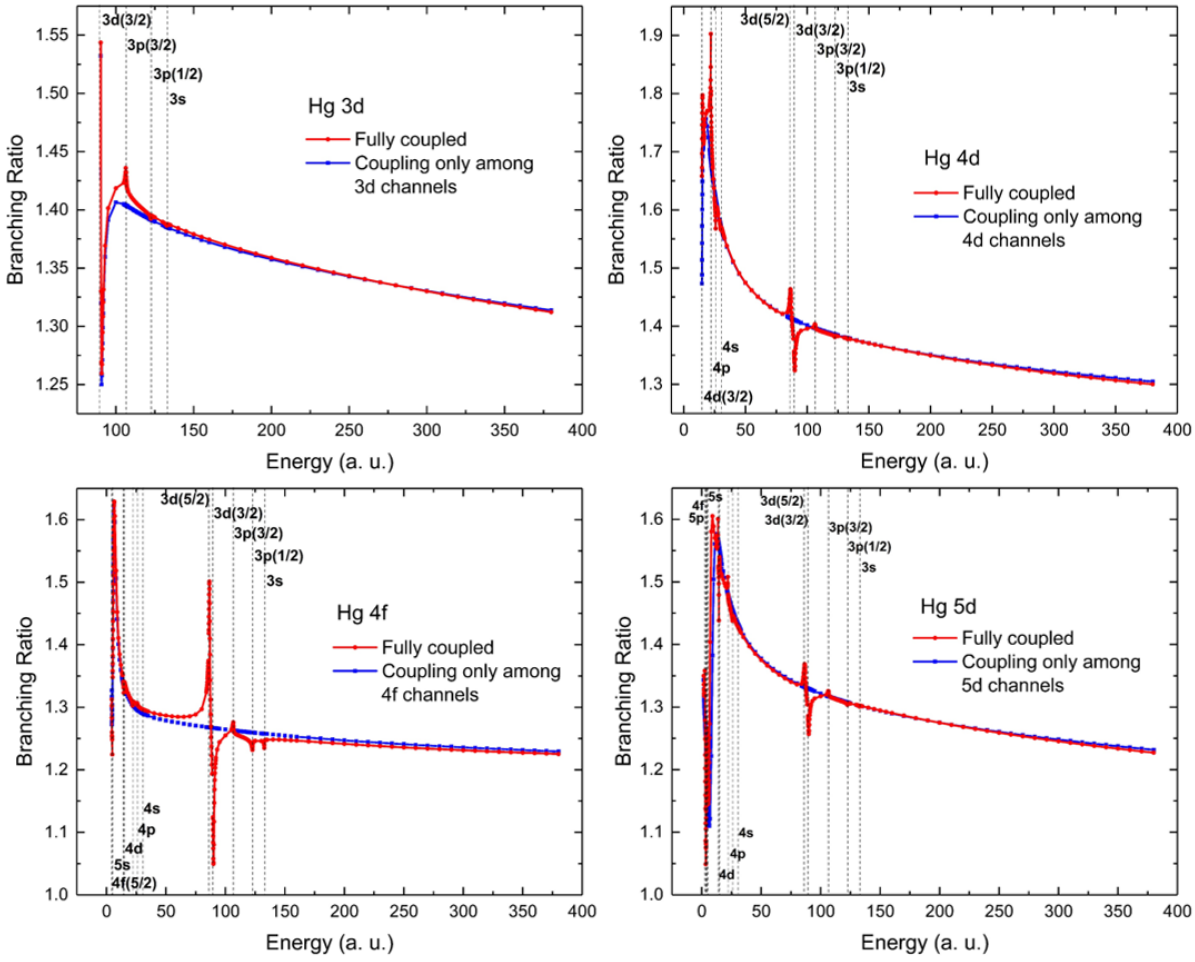

Figure 4.27 Branching ratio of Hg 3d, 4d, 5d $\left(\sigma_{nd(5/2)}/\sigma_{nd(3/2)}\right)$*, and 4f* $\left(\sigma_{4f(7/2)}/\sigma_{4f(5/2)}\right)$ *calculated with fully coupled (red-dots), and with only intrashell coupling (blue-squares). The vertical dashed lines indicate the thresholds.*

As seen and explained in other elements, Hg high-energy branching ratios are highly independent of principal quantum number *n* of the initial *np* or *nd* state, as shown in figures 4.26 and 4.27. The high-energy branching ratios of Hg subshells are depicted in figure 4.28 to clearly identify this behavior.

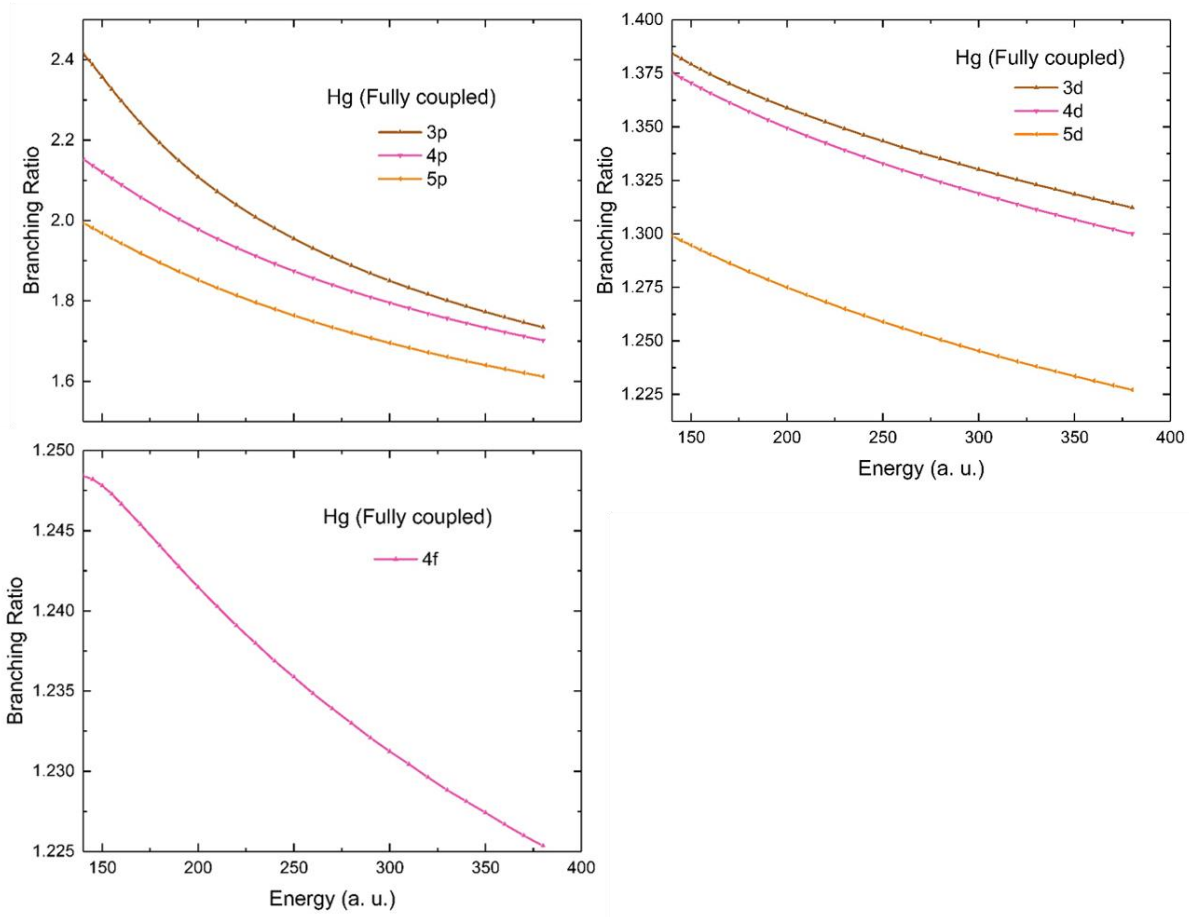

Figure 4.28 Comparison of Hg branching ratios np (3p –brown, 4p –pink, and 5p – orange) (upper left panel), nd (3d –brown, 4d –pink, and 5d –orange) (upper right panel), and 4f (lower left panel) at high-energy region.

All the branching ratios of Hg move further away below their statistical values with increasing energy as in other elements, and for *d*-subshells in Hg, this has been experimentally verified [44]. The *nd* and *np* branching ratios of Hg are somewhat lower than in the Xe, as expected. Furthermore, Hg *nd* branching ratios fall off slower than *np* as discussed in Xe and Kr, and 4*f* falls off even slower. It conveys the idea that the relativistic effects on the wave functions get smaller with the angular quantum number *l*. Hg *f* subshells experience a huge angular momentum barrier involved in the $f \rightarrow g$ transitions [58], and it causes their slower decrement with energy.

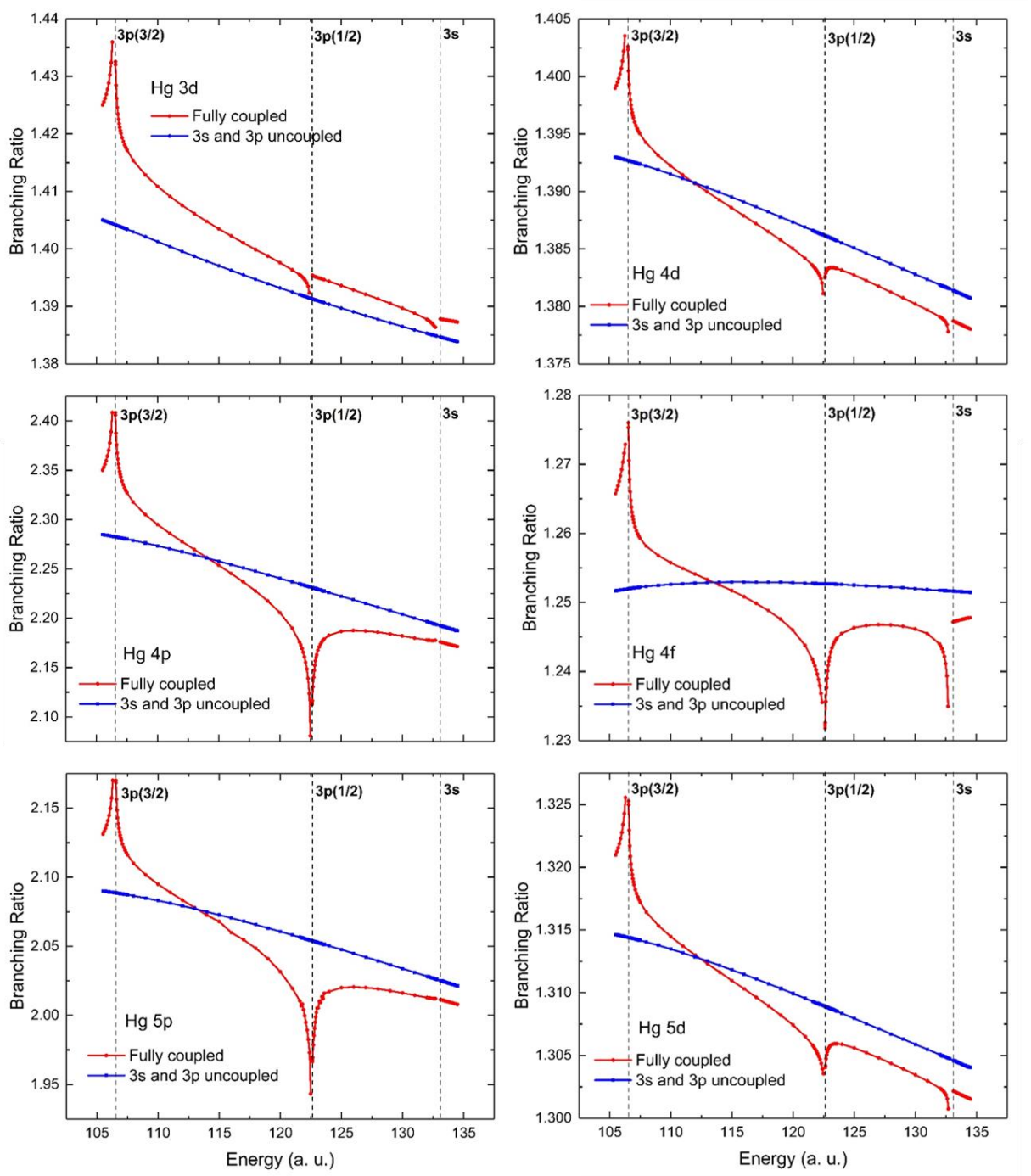

Figure 4.29 Branching ratios of Hg 3d, 4d, 5d $\left(\sigma_{nd\,(5/2)}/\sigma_{nd\,(3/2)}\right)$*, 4p, 5p* $\left(\sigma_{np\,(3/2)}/\sigma_{np\,(1/2)}\right)$*, and 4f* $\left(\sigma_{4f\,(7/2)}/\sigma_{4f\,(5/2)}\right)$ *calculated with fully coupled (red-dots), and without coupling to 3s and 3p channels (blue-squares). The vertical dashed lines indicate the thresholds.*

To explore the large excursions of Hg plots from their smooth behavior in the vicinity of inner-shell thresholds, Hg branching ratios in the region of $n = 3$ and $n = 4$ (*ns* and *np*) thresholds are shown in figure 4.29 and 4.30 respectively. When the corresponding *ns* and *np* channels are excluded from the calculations, the branching ratios are monotonically decreasing, thereby implying that the structures appeared due to the coupling.

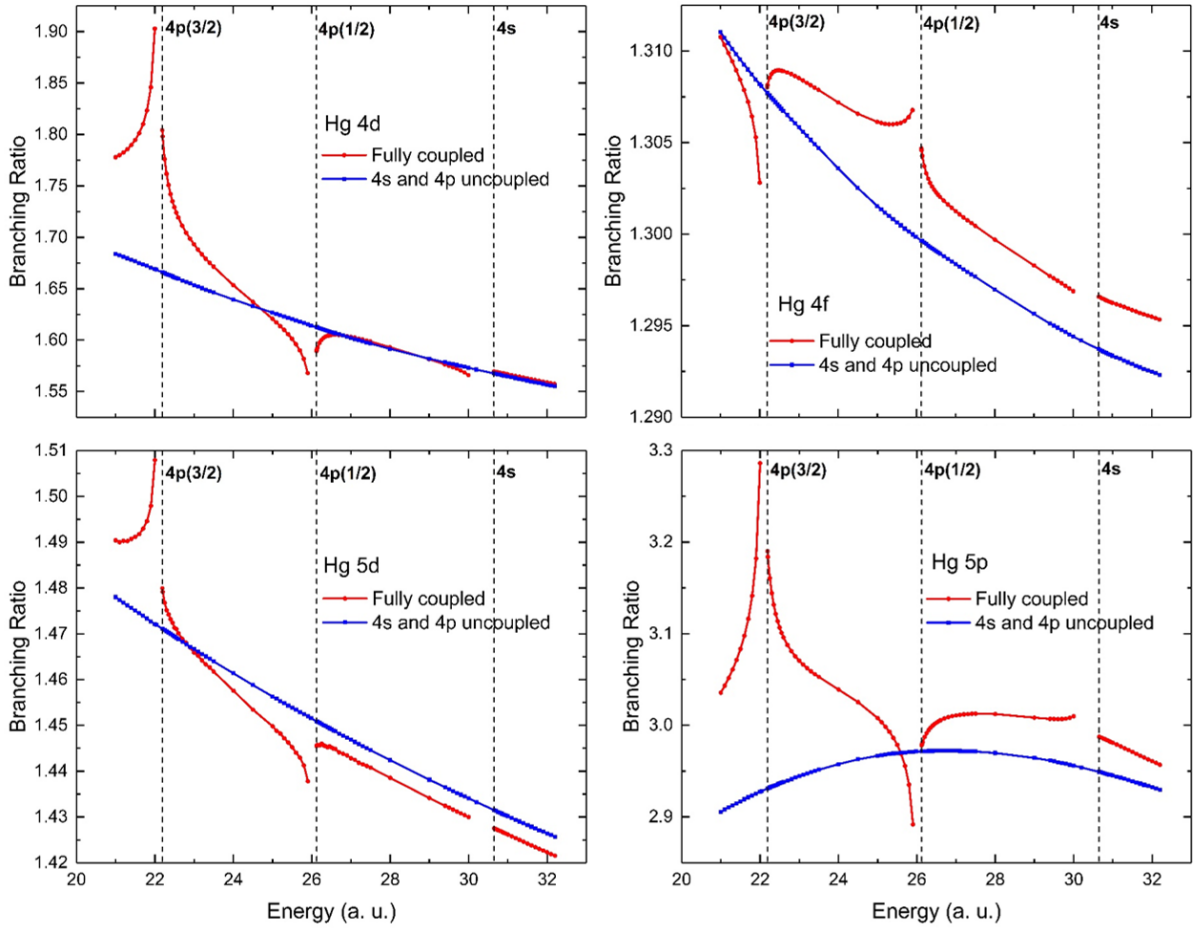

Figure 4.30 Branching ratios of Hg 4d, 5d $\left(\sigma_{nd\,(5/2)}/\sigma_{nd\,(3/2)}\right)$*, 5p* $\left(\sigma_{5p\,(3/2)}/\sigma_{5p\,(1/2)}\right)$*, and 4f* $\left(\sigma_{4f\,(7/2)}/\sigma_{4f\,(5/2)}\right)$ *calculated with fully coupled (red-dots), and without coupling to 4s and 4p channels (blue-squares). The vertical dashed lines indicate the thresholds.*

Qualitatively, the trend of all the branching ratios is the same around both sets of thresholds $n = 3$ and $n = 4$, except that the 4*f* branching ratio resonance behavior is flipped around $n = 4$

thresholds. The resonance has different shapes in the vicinity of the spin-orbit doublet threshold of Hg *p* subshells as in other elements. For Hg also, the excursion from the smooth background of the branching ratios around $n = 4$ thresholds is smaller in magnitude than around $n = 3$ thresholds, indicating that the interchannel coupling is less relativistic with principal quantum number *n*. As discussed for other elements, for Hg also, interchannel coupling affects the branching ratios over a broad energy range and it is not limited to just around the inner-shell thresholds. However, Hg does not exhibit the peculiar increase of branching ratios with the energy around *ns* thresholds.

The branching ratios of Hg 4*p*, 5*p*, 4*d*, 5*d*, and 4*f* in the vicinity of the 3*d* thresholds are particularly interesting and are shown in figure 4.31. Without the coupling of the 3*d* photoionization channels, the branching ratio plots are smooth and monotonically decreasing, demonstrating that the variations with energy are entirely due to the interchannel coupling. The branching ratio trends in the vicinity of 3*d* thresholds are altogether different than in the area of *np* thresholds. All the branching ratios follow a similar trend around the *np* thresholds. But around the 3*d* thresholds, the *nd* and *nf* branching ratios follow a similar pattern with a peak above the 3*d*(5/2) and a dip above the 3*d*(3/2) thresholds, while the *np* branching ratios exhibit dips above both thresholds. Therefore, the effect of the interchannel coupling with 3*d* subshells is dependent on the angular momentum as in the Xe case.

It is evident from the truncated calculations that the coupling with 3*d*(3/2) channels is primarily responsible for the structures around the 3*d*(3/2) threshold and coupling with the 3*d*(5/2) channel is entirely responsible for the structures around 3*d*(5/2) threshold. In this region also, the Auger resonance have different shapes below each of the 3*d* thresholds.

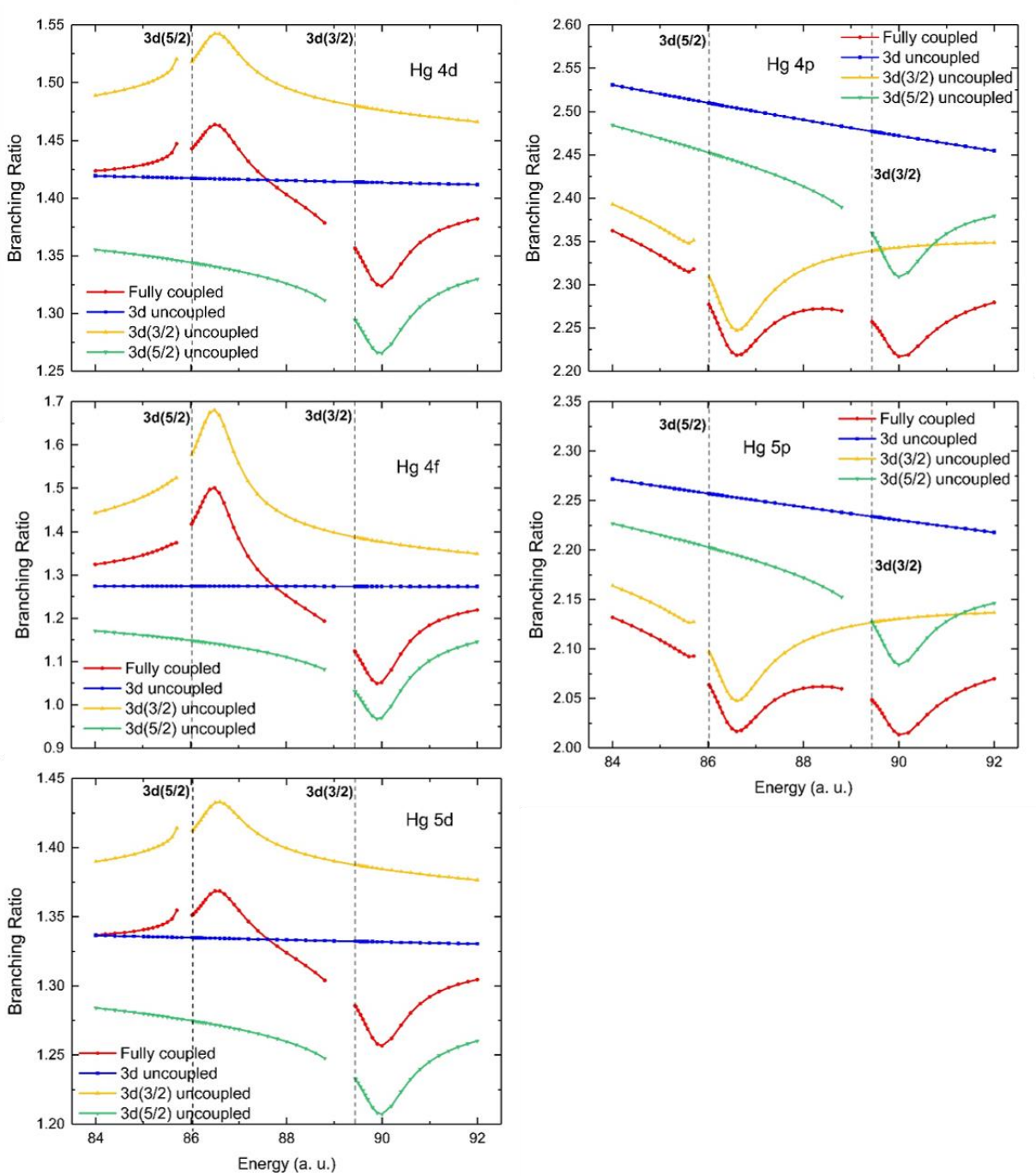

Figure 4.31 Branching ratios of Hg 4d, 5d $\left({}^{\sigma_{nd\,(5/2)}}/_{\sigma_{nd\,(3/2)}}\right)$*, 4p, 5p* $\left({}^{\sigma_{np\,(3/2)}}/_{\sigma_{np\,(1/2)}}\right)$*, and 4f* $\left({}^{\sigma_{4f\,(7/2)}}/_{\sigma_{4f\,(5/2)}}\right)$ *calculated with fully coupled (red-dots), without coupling to 3d channels (blue-squares), without coupling to 3d(3/2) channels (yellow-triangles), and without coupling to 3d(5/2) channels (green-inverted triangles). The vertical dashed lines indicate the 3d thresholds.*

In the vicinity of 3*d* thresholds, variations of Hg 4*d* and 5*d* branching ratios are much more significant than *np* case as in Xe. However, the Hg 4*f* variation is the largest in this energy region. In general, the interchannel coupling matrix element is larger between channels of the same angular momenta than in between channels of different angular momenta. But in this case, coupling between 3*d* and 4*f* subshells is stronger than the coupling between 3*d* and other *nd* subshells.

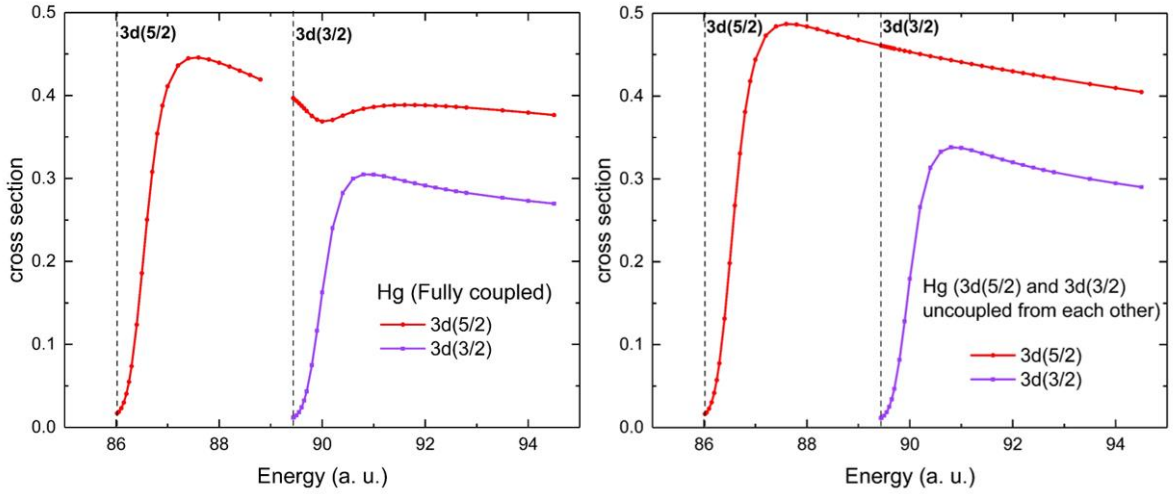

Figure 4.32 Calculated Hg 3d cross sections, 3d(3/2) (purple) and 3d(5/2) (red), left panel – fully coupled and right panel – uncoupled from each other.

To understand the variations of branching ratios around 3*d* thresholds, the individual cross sections for the 3*d* spin-orbit doublets were examined and results are shown in figure 4.32. The fully coupled Hg 3*d*(5/2) cross section exhibits a small drop at 90 a. u. near the energy of the 3*d*(3/2) maximum (left panel of figure 4.32). If the 3*d*(5/2) and 3*d*(3/2) channels are uncoupled from each other, this drop disappears (right panel of figure 4.32). This clearly indicates a spin-orbit interaction activated interchannel coupling (SOIAIC) effect as in the Xe case. However, the Hg branching ratios and cross sections do not show huge variations around 3*d* thresholds as Xe.

The features in the Xe branching ratios around the 3d thresholds are located at the exact photon energies of the shape resonance maxima of 3d spin-orbit doublet. Similarly, the extra drop of Hg 3d(5/2) cross section due to the SOIAIC effect is located at the photon energy of 90 a. u., and all the branching ratios show a drop at that energy. However, the other extrema of Hg branching ratio curves located at 86.6 a. u. while maximum point of 3d(5/2) cross section is located at 87.4 a. u. This indicates that for the Hg SOIAIC effect, oscillator strength transfers affect a board energy region, unlike Xe. The interchannel coupling effect in the photoionization process is rather complicated and can be expressed qualitatively from a perturbation point of view as the equation 4.2 [59, 60].

$$\boldsymbol{D_i(E) = M_i(E) + \sum_j \int dE' \frac{\langle \psi_i(E)|H-H_0|\psi_j(E')\rangle}{E-E'} M_j(E')}, \quad \textbf{(4.2)}$$

where, $D_i(E)$ is the fully coupled dipole matrix element of channel i, $M_i(E)$ are the uncoupled matrix elements of the various photoionization channels j, $H - H_0$ is the perturbing Hamiltonian, and $\psi_i(E)$ and $\psi_j(E')$ are final continuum wave functions of channel i and j and energies E and E' respectively. As per equation 4.2, depending on the configuration interactions in the final continuum state, the final continuum state wave functions of the channels with larger and smaller cross sections will transfer oscillator strength with each other. The interchannel coupling matrix element $\langle \psi_i(E)|H - H_0|\psi_j(E')\rangle$ will affect strongly to the channels with much smaller matrix elements.

Figure 4.33 shows the 4f, 5p, and 5d branching ratios in the vicinity of 4d thresholds. In this low-energy region, coupling effects are small. But still, due to the interchannel coupling of 4d channels, there is a rise and a drop above the 4d(3/2) threshold on 4f and 5d branching ratio curves,

respectively. As in 3*d* case, the coupling effect is dominant in *d* and *f* subshell branching ratios than in *p* subshell.

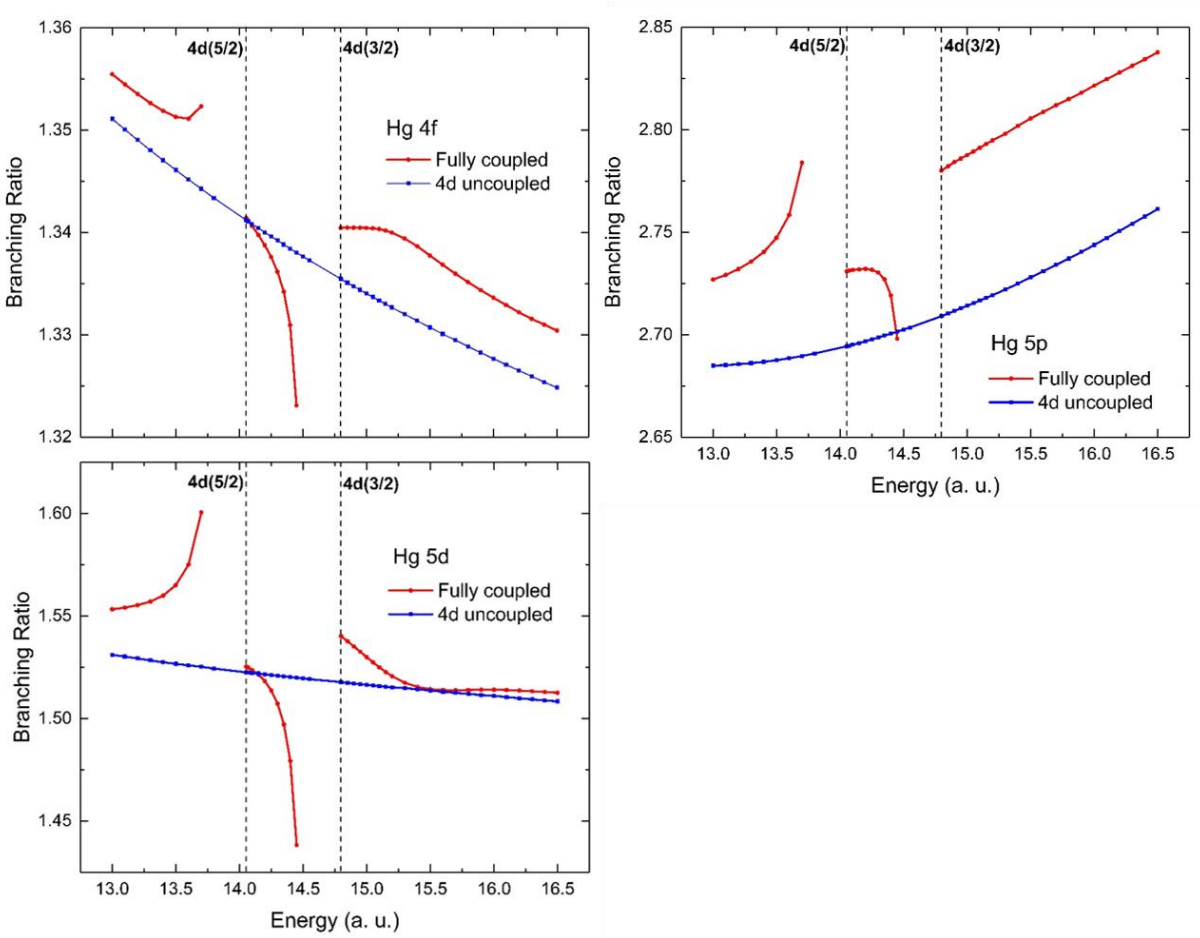

Figure 4.33 Branching ratios of Hg 4f $\left(\sigma_{4f\,(7/2)}/\sigma_{4f\,(5/2)}\right)$*, 5d* $\left(\sigma_{5d\,(5/2)}/\sigma_{5d\,(3/2)}\right)$*, and 5p* $\left(\sigma_{5p\,(3/2)}/\sigma_{5p\,(1/2)}\right)$ *calculated with fully coupled (red-dots), and without coupling to 4d channels (blue-squares). The vertical dashed lines indicate the 4d thresholds.*

4.6 Radon (Rn)

Radon is the heaviest noble gas atom studied, and electrons of Rn in the deeper inner shells have large effective *Z* and, therefore, it is highly relativistic as well as being radioactive. Rn calculations involved a total of 52 relativistic photoionization channels from 3*s*, 3*p*, 3*d*, 4*s*, 4*p*, 4*d*,

4*f*, 5*s*, 5*p*, *5d*, *6s*, and 6*p* subshells, leaving out the 1*s*, 2*s*, and 2*p* channels. As discussed in the sections on Xe and Hg, those channels were excluded since the binding energies of those subshells are so much higher than the considered energy range, they are essentially irrelevant for our calculations.

Table 4-6 Calculated subshell thresholds of Rn in atomic energy units

Subshell	Threshold (Relativistic)	Threshold (Nonrelativistic)
1*s*	3641.158	3229.917
2*s*	668.805	556.869
2*p*(1/2)	642.330	536.679
2*p*(3/2)	541.103	536.679
3*s*	166.832	138.412
3*p*(1/2)	154.895	128.672
3*p*(3/2)	131.731	128.672
3*d*(3/2)	112.567	110.702
3*d*(5/2)	107.759	110.702
4*s*	41.313	33.918
4*p*(1/2)	36.020	29.491
4*p*(3/2)	30.121	29.491
4*d*(3/2)	21.548	21.331
4*d*(5/2)	20.439	21.331

Table 4-6 shows the relativistically and nonrelativistically calculated subshell thresholds of Rn. The atomic number (*Z*) of Rn is 86, which is much heavier than the atoms considered so far. Therefore, as expected, the relativistic and nonrelativistic thresholds deviate considerably from each other. As noted and explained for the previous cases, in Rn also, outer subshells experience smaller deviations between relativistic and nonrelativistic calculations, and the nonrelativistic energies for *np*, *nd* and *nf* spin-orbit doublets are the same. All the elements show that for a specific atom, the spin-orbit splitting decreases with increasing *n* and *l*, while the splitting increases with *Z*.

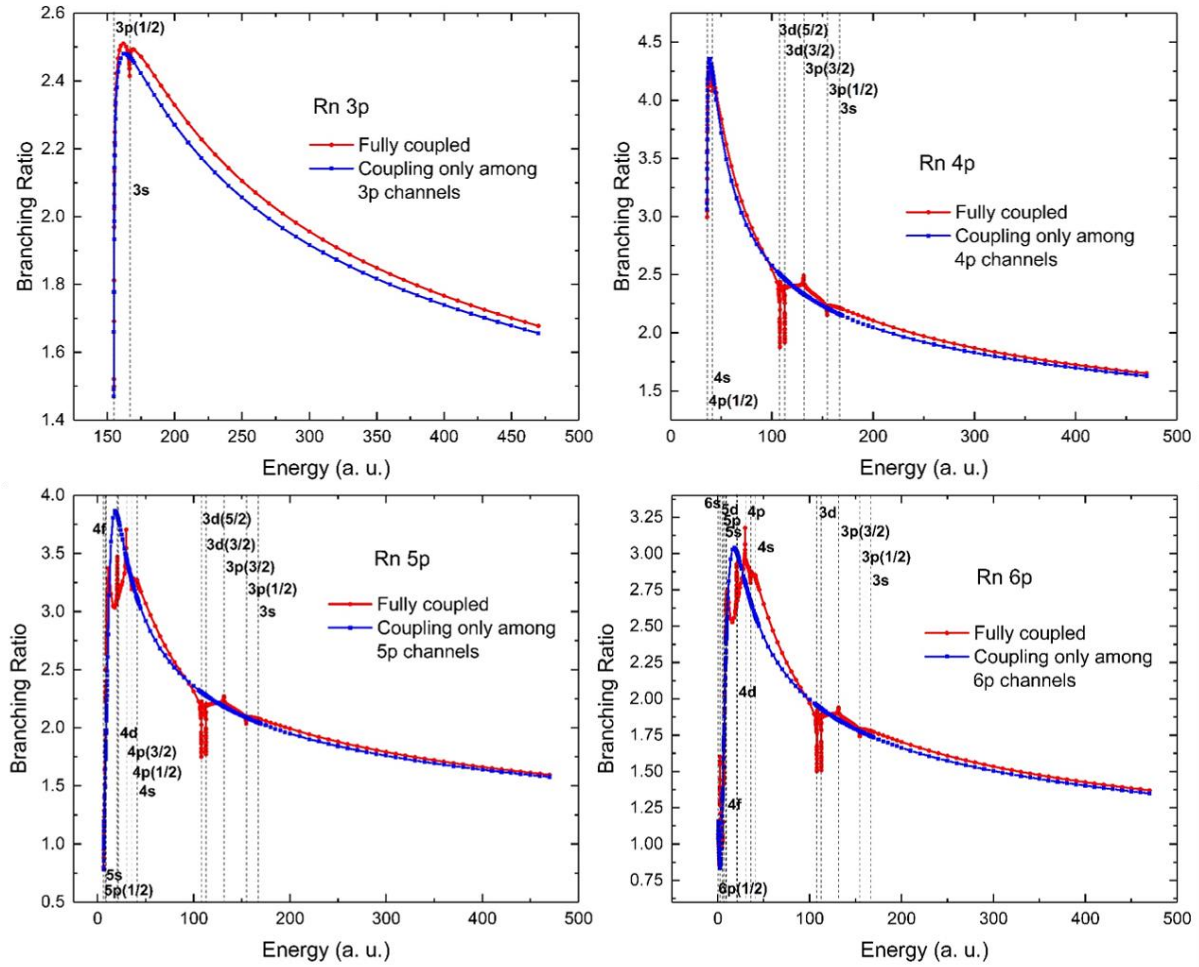

Figure 4.34 Branching ratio of Rn 3p, 4p, 5p, and 6p $\left(\sigma_{np(3/2)}/\sigma_{np(1/2)}\right)$ *calculated with fully coupled (red-dots), and with only intrashell coupling (blue-squares). The vertical dashed lines indicate the thresholds.*

The overall views of Rn's *np*, *nd*, and 4*f* branching ratios are shown in figures 4.34 and 4.35 respectively. Owing to the increased relativistic effect with higher Z, Rn exhibit the highest decrement of the branching ratios from their statistical ratios out of all the elements studied. At the highest energy point, 470 a. u., the *np* branching ratios of Rn are in the range of 1.37 – 1.68 while *nd* branching ratios are in the range of 1.24 – 1.28. They are somewhat lower than in previous elements, as expected. The difference between the branching ratios of fully coupled and intrashell coupled curves is slightly larger for Rn, following the trend that the difference is increased with *Z*.

Moreover, high-energy branching ratios are primarily independent of the principal quantum number of the initial *p* or *d* state. The comparison of high-energy branching ratios of Rn is shown in figure 4.36. The Rn *nd* branching ratios fall off slower than *np* as discussed in previous elements, and 4*f* falls off even slower. This shows that the relativistic effect on the wave functions is getting smaller with the angular quantum number *l*. moreover, *f* subshells are experiencing a huge angular momentum barrier involved in the $f \rightarrow g$ transitions causing a slower decrement of branching ratio with energy.

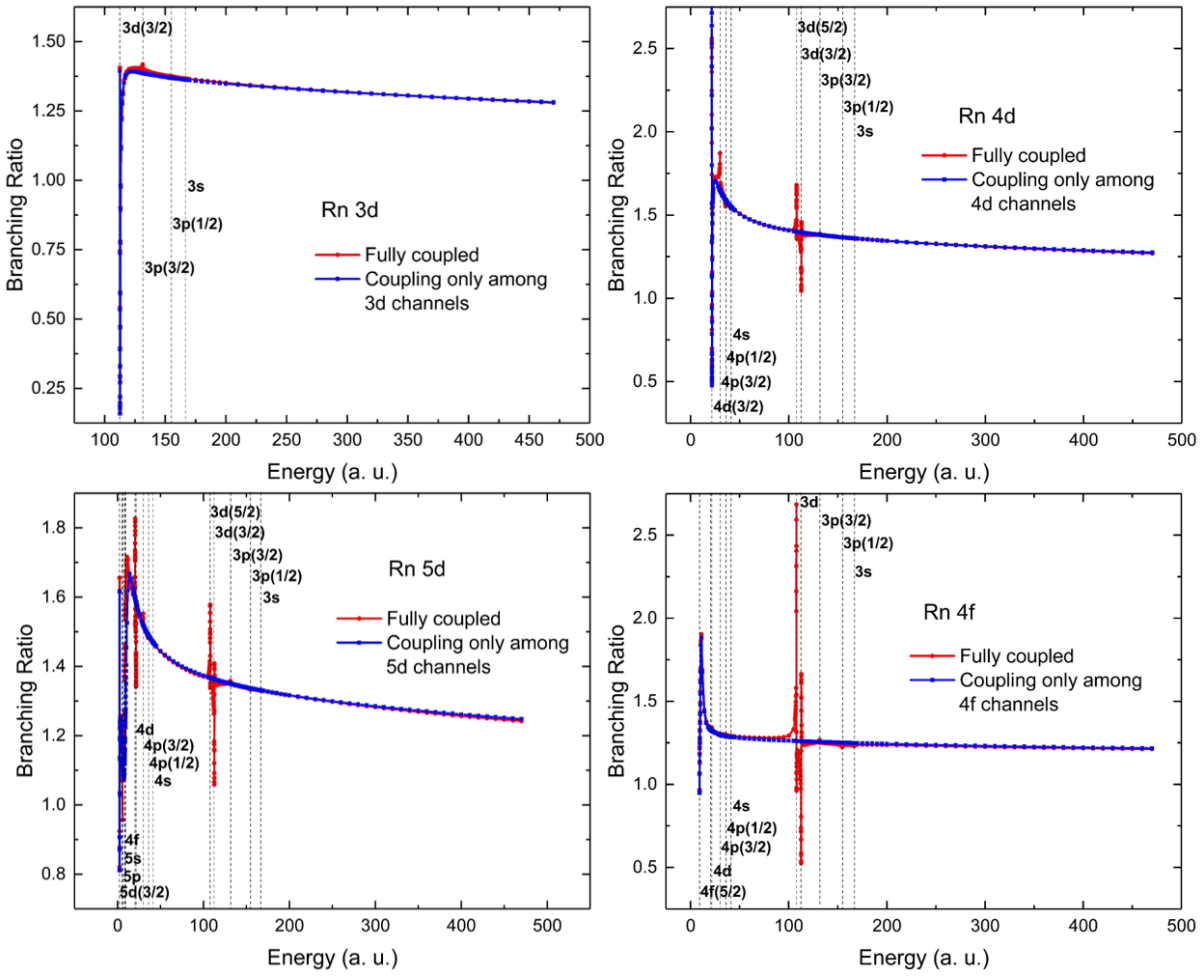

Figure 4.35 Branching ratio of Rn 3d, 4d, 5d $\left(\sigma_{nd\,(5/2)}/\sigma_{nd\,(3/2)}\right)$*, and 4f* $\left(\sigma_{4f\,(7/2)}/\sigma_{4f\,(5/2)}\right)$ *calculated with fully coupled (red-dots), and with only intrashell coupling (blue-squares). The vertical dashed lines indicate the thresholds.*

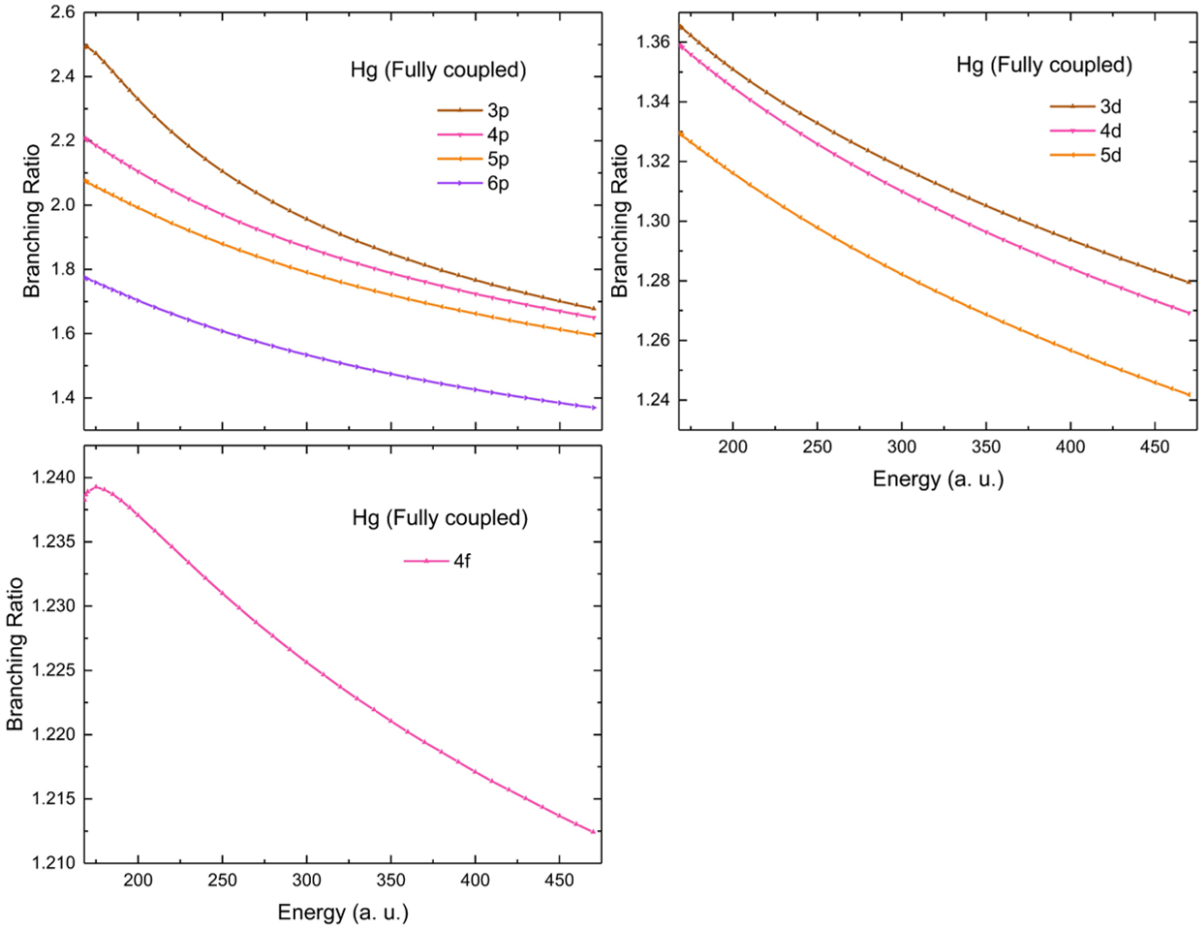

Figure 4.36 Comparison of Rn branching ratios np (3p –brown, 4p –pink, 5p –orange, and 6p -purple) (upper left panel), nd (3d –brown, 4d –pink, and 5d –orange) (upper right panel), and 4f (lower left panel) at high-energy region.

To explore the effect of interchannel coupling, Rn branching ratios in the vicinity of inner-shell thresholds $n = 3$ and $n = 4$ (*ns* and *np*) were plotted and shown in figures 4. 37, 4.38, and 4.39. When the corresponding *ns* and *np* channels are excluded from the calculations, the branching ratios monotonically decrease, demonstrating that the structures are due to interchannel coupling. However, Rn does not exhibit the increase of branching ratios with the energy around *ns* thresholds as seen in Xe and Kr.

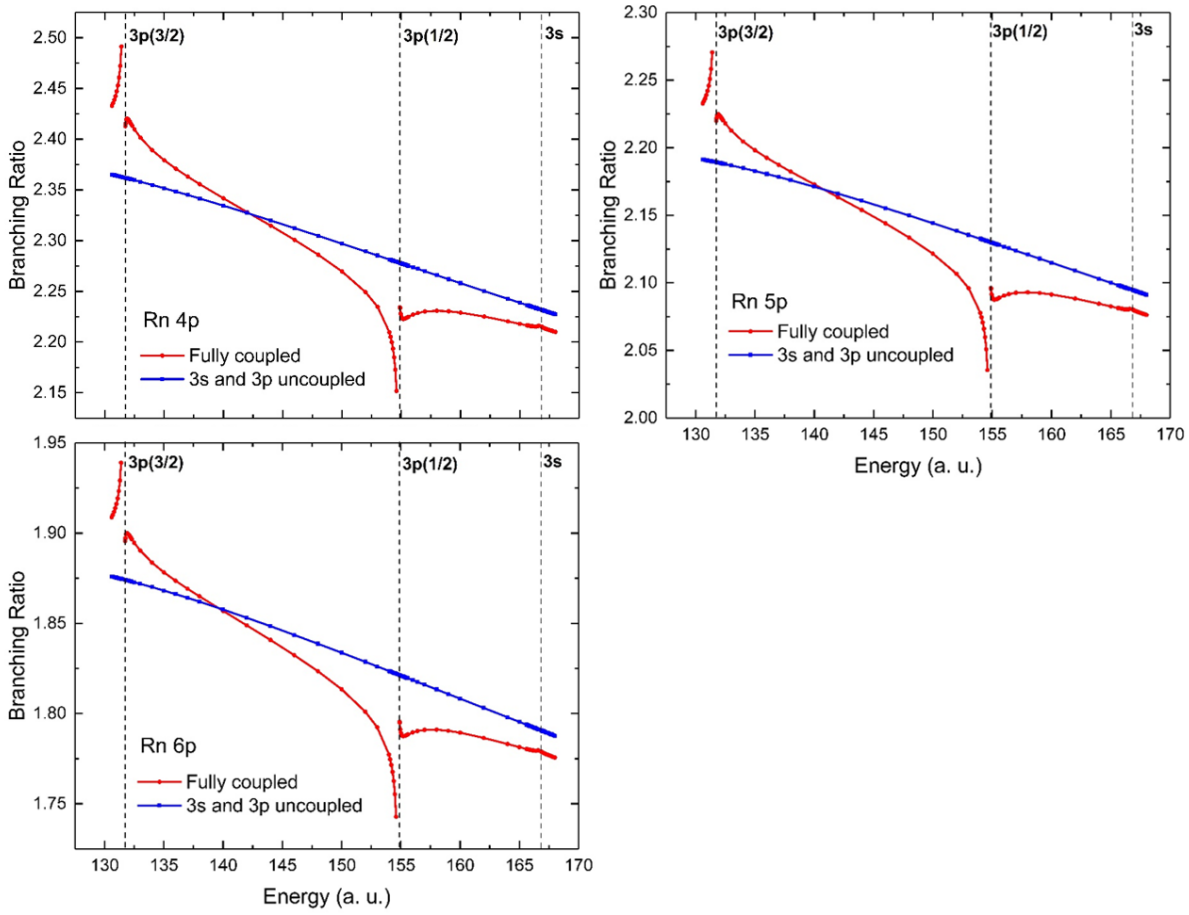

Figure 4.37 Branching ratios of Rn 4p, 5p, and 6p $\left({}^{\sigma_{np(3/2)}}/_{\sigma_{np(1/2)}}\right)$ *calculated with fully coupled (red-dots) and without coupling to 3s and 3p channels (blue-squares). The vertical dashed lines indicate the thresholds.*

Qualitatively, the trend of all the branching ratios is the same around both sets of thresholds $n = 3$ and $n = 4$. The pointing up and down of the branching ratio curves before thresholds indicate that the resonance has different shapes around different subshells as in other elements. For Rn also, the excursion from the smooth background of plots around $n = 4$ thresholds is smaller in magnitude than around $n = 3$ thresholds, indicating the interchannel coupling is getting less relativistic with principal quantum number n. As discussed in the other elements, for Rn also, interchannel coupling affects the branching ratios over a broad energy range, not limited to subshell thresholds.

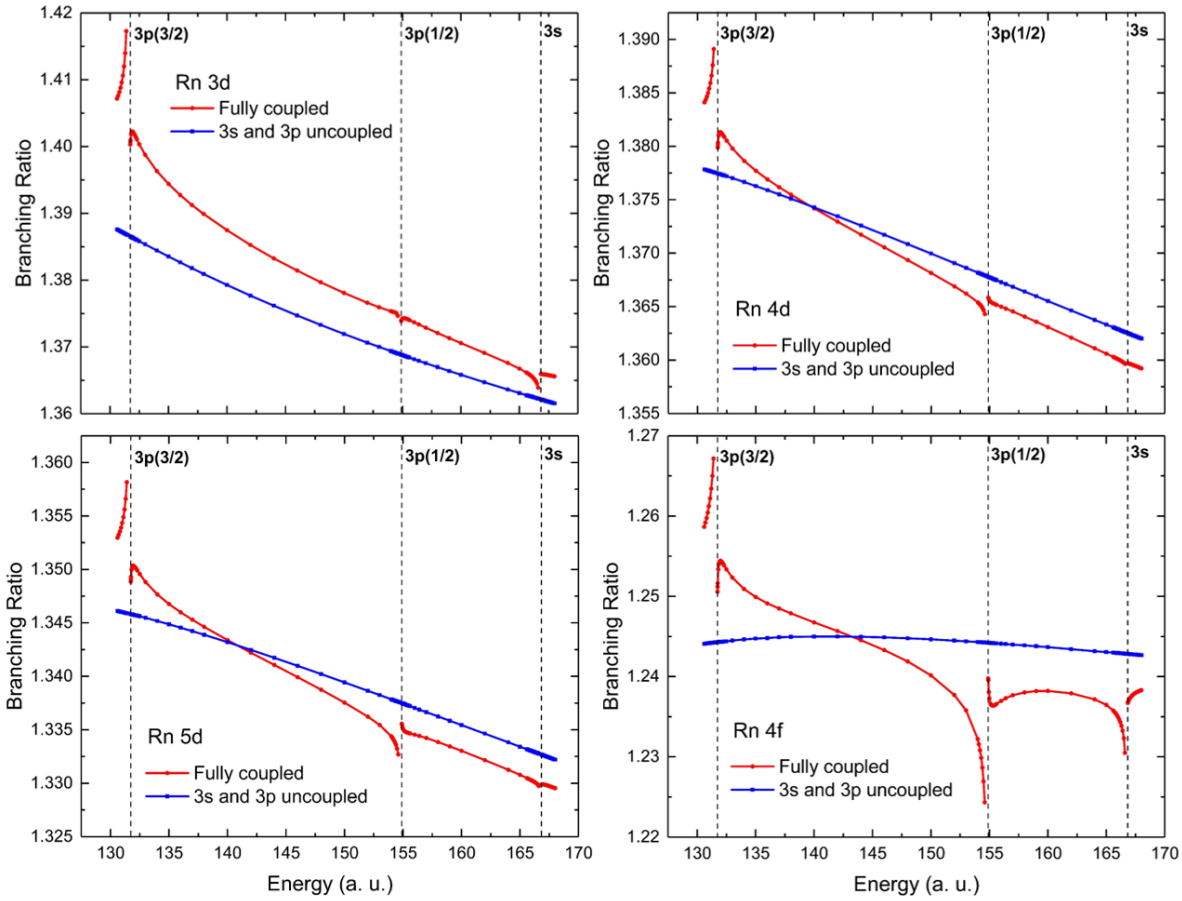

Figure 4.38 Branching ratios of Rn 3d, 4d, 5d $\left(\sigma_{nd(5/2)}/\sigma_{nd(3/2)}\right)$*, and 4f* $\left(\sigma_{4f(7/2)}/\sigma_{4f(5/2)}\right)$ *calculated with fully coupled (red-dots), and without coupling to 3s and 3p channels (blue-squares). The vertical dashed lines indicate the thresholds.*

Similar interchannel coupling effects were found at low energies in previous studies [61, 62], especially for n = 5 subshells. In these studies, several minima in dipole matrix elements induced by interchannel coupling were found. The existence and location of these various minima are important determinants of the spectral distribution of the oscillator strength in the photoionization cross sections and branching ratios [62].

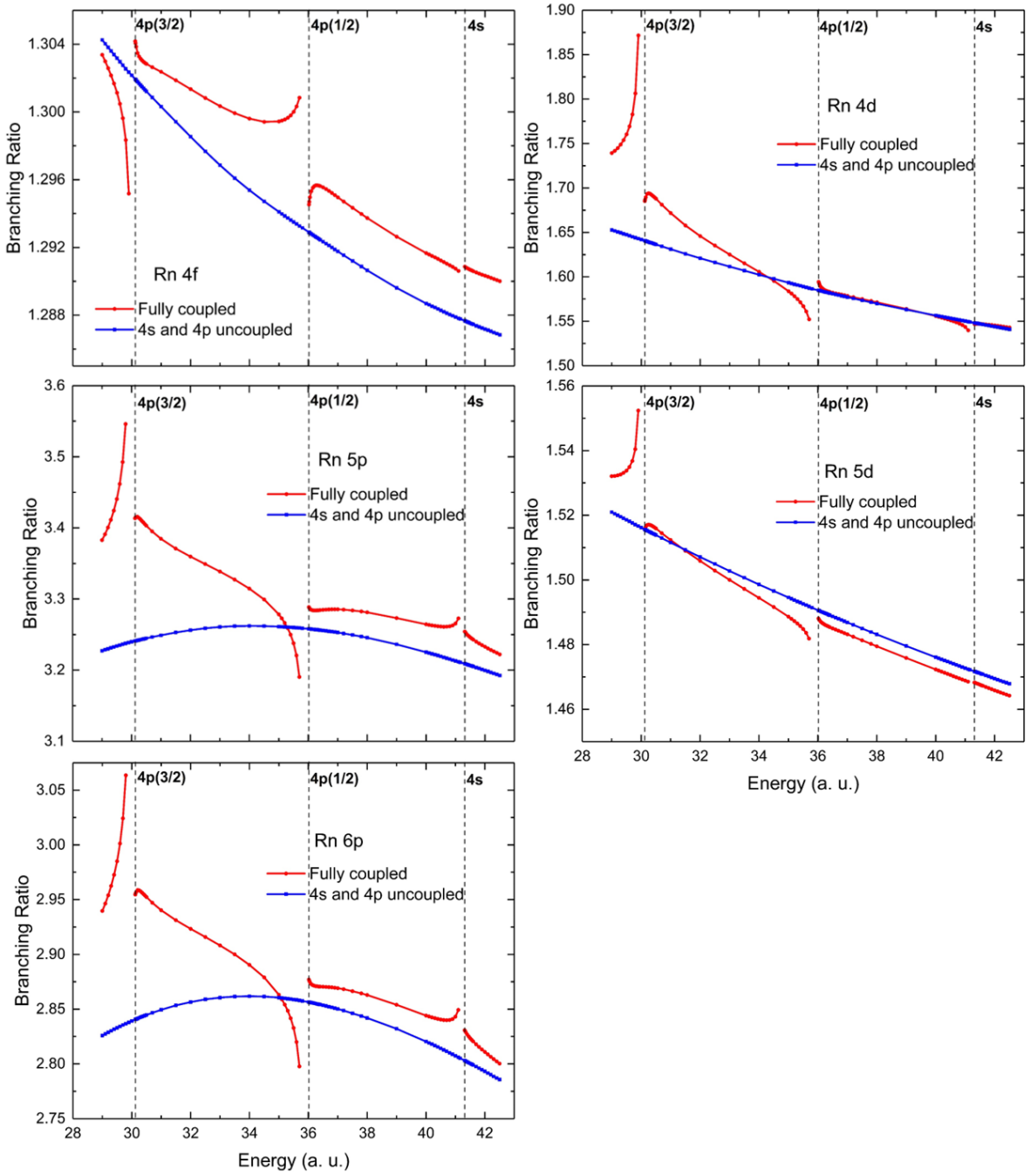

Figure 4.39 Branching ratios of Rn 4d, 5d $\left(\sigma_{nd(5/2)}/\sigma_{nd(3/2)}\right)$*, 5p, 6p* $\left(\sigma_{np(3/2)}/\sigma_{np(1/2)}\right)$*, and 4f* $\left(\sigma_{4f(7/2)}/\sigma_{4f(5/2)}\right)$ *calculated with fully coupled (red-dots), and without coupling to 4s and 4p channels (blue-squares). The vertical dashed lines indicate the thresholds.*

The branching ratios of Rn 4*p*, 5*p*, 6*p*, 4*d*, 5*d*, and 4*f* in the vicinity of the 3*d* thresholds are particularly interesting because of the unusual structures in the curves and are shown in figure 4.40. The sharp variations in the branching ratios are caused solely by the coupling with 3*d* channels because omitting coupling of those channels gives featureless plots. The branching ratio trends in the vicinity of 3*d* thresholds are altogether different from the area of *np* thresholds as in the Xe case. All the branching ratios follow a similar trend around the *np* thresholds. But around the 3*d* thresholds, the *nd* and *nf* branching ratios follow a similar pattern with a peak and then a drop above the 3*d*(5/2) threshold and a dip and then a rise above the 3*d*(3/2) threshold, while the *np* branching ratios exhibit a drop and then a rise above both thresholds. Therefore, the effects of the interchannel coupling with 3*d* subshells are dependent on the angular momentum as in the Xe and Hg cases.

In the neighborhood of 3*d* thresholds, fully coupled *4p*, 5*p*, and 6*p* branching ratios vary by about 0.6, 0.5, and 0.4, respectively, within a small energy range. Also, fully coupled *4d*, 5*d* and 4*f* branching ratios vary about 0.6, 0.5, and 2.2 respectively, within the same energy range. This pattern indicates that the interchannel coupling effect of 3*d* increases with the angular momentum quantum number *l* while decreasing with the principal quantum number *n*. This decrement with *n* can be explained in that with the increasing *n*, the subshell moves further away from the 3*d* subshells thereby decreasing the interchannel coupling matrix element.

To understand interchannel coupling effects in this region, the individual cross sections of the Rn 3*d* spin-orbit doublets were examined, and the results are shown in figure 4.41. The 3*d* cross sections show sharp maxima above the thresholds known as shape resonance or delayed maxima, as discussed in the Xe section. In addition, the Rn 3*d*(5/2) cross section exhibits an extra small drop and a rise in the energy region of the 3*d*(3/2) shape resonance maximum. If the 3*d*(5/2)

and 3*d*(3/2) channels are uncoupled from each other, these extrema disappear (right panel of figure 4.41). This clearly indicates a SOIAIC effect as in the Xe and Hg case.

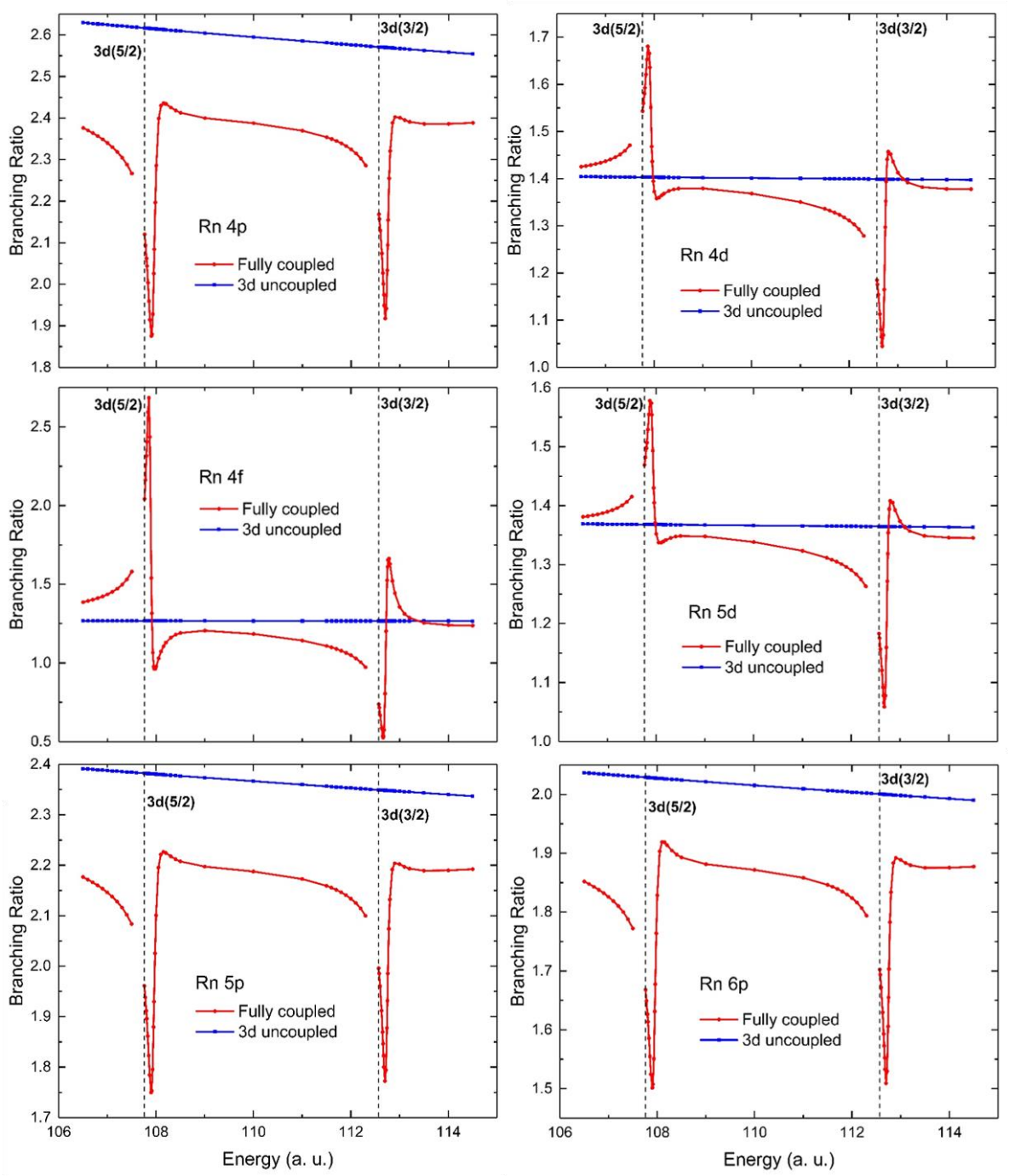

Figure 4.40 Branching ratios of Rn and 4p, 5p, 6p $\left(\sigma_{np(3/2)}/\sigma_{np(1/2)}\right)$*, 4d, 5d* $\left(\sigma_{nd(5/2)}/\sigma_{nd(3/2)}\right)$*, and 4f* $\left(\sigma_{4f(7/2)}/\sigma_{4f(5/2)}\right)$ *calculated with fully coupled (red-dots), and without coupling to 3d channels (blue-squares). The vertical dashed lines indicate the 3d thresholds.*

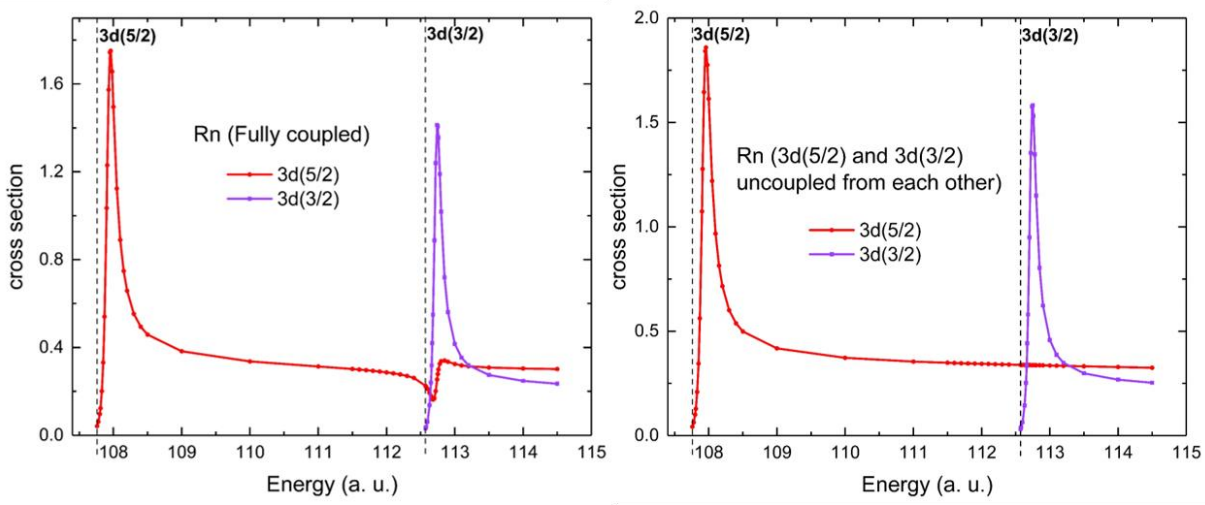

Figure 4.41 Calculated Rn 3d cross sections, 3d(3/2) (purple) and 3d(5/2) (red), left panel – fully coupled and right panel – uncoupled from each other.

The shape resonance occurred on Rn 3*d* cross sections at 108 a. u. and 113 a. u. and the extrema on all the branching ratio curves located around the same energy points. As in equation 4.2, the interchannel coupling matrix element strongly affects the channels with much smaller matrix elements. Here the shape resonance in 3*d*(3/2) induces variations in the 3*d*(5/2) cross section at the energy where it is comparably small. This phenomenon makes significant variations on other cross sections, making features in branching ratio curves.

The branching ratios of Rn 5*p*, 6*p*, 5*d*, and 4*f* in the vicinity of the 4*d* thresholds are shown in figure 4.42, and the 3*d* cross sections in the same energy region are shown in figure 4.43. They exhibit similar behavior as the above phenomenon around 3*d* thresholds. However, in this situation, the features of the branching ratios are smaller, and extrema are not sharp, as in 3*d* case. It is interesting to note that except for 5*d*, all the other branching ratio curves flip around 4*d* thresholds compared to around 3*d* thresholds. To verify and fully understand this behavior, further studies with high *Z* atoms will be needed.

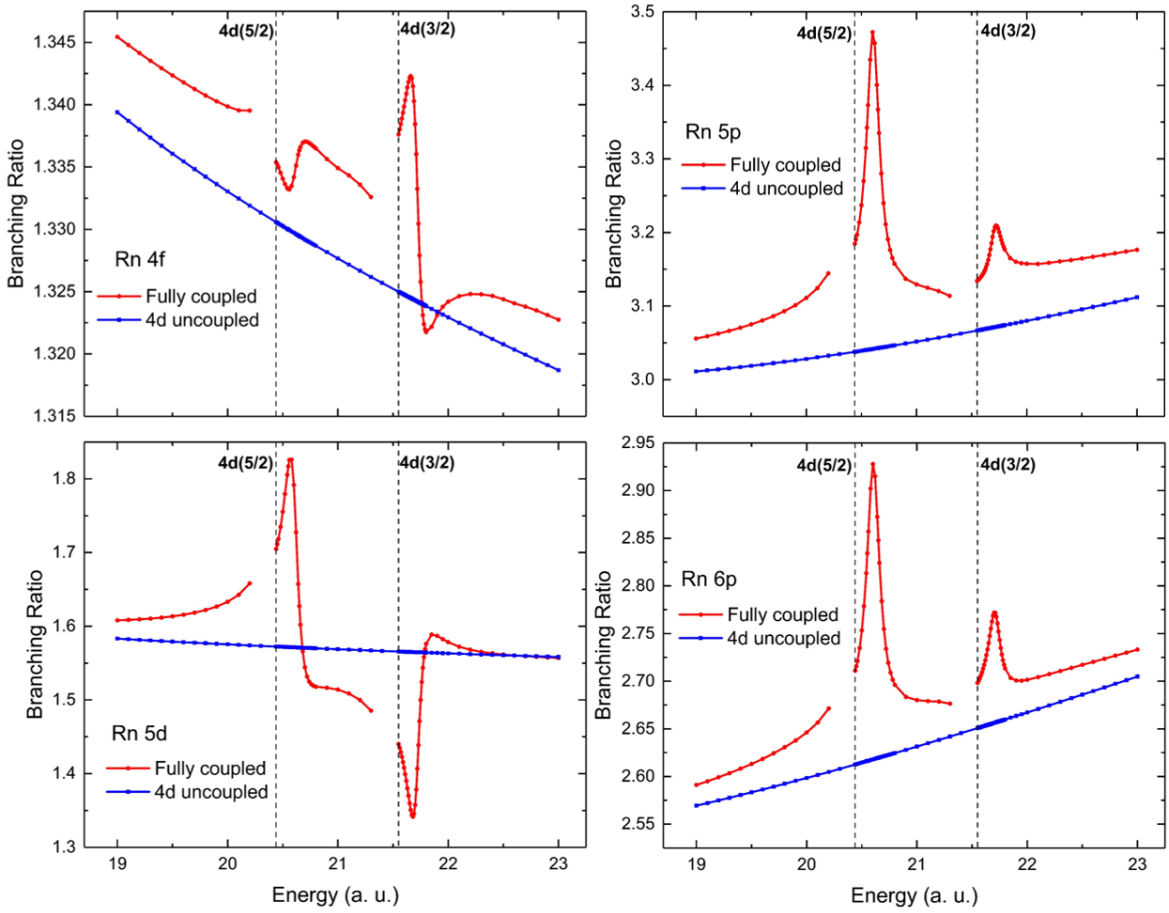

Figure 4.42 Branching ratios of Rn and 5p, 6p $\left({}^{\sigma_{np(3/2)}}/_{\sigma_{np(1/2)}}\right)$*, 5d* $\left({}^{\sigma_{5d(5/2)}}/_{\sigma_{5d(3/2)}}\right)$*, and 4f* $\left({}^{\sigma_{4f(7/2)}}/_{\sigma_{4f(5/2)}}\right)$ *calculated with fully coupled (red-dots), and without coupling to 4d channels (blue-squares). The vertical dashed lines indicate the 4d thresholds.*

The variation of 4*d* cross sections in the vicinity of their thresholds is also similar to that of 3*d*. However, the induced SOIAIC feature in the 4*d*(5/2) cross section, just above the 4*d*(3/2) threshold is smaller than in the 3d case. This occurs because the maximum in the uncoupled 4*d*(3/2) cross section is only a factor of two larger than the 4*d*(5/2) cross section at the same energy, while in the 3*d* case, it is a factor of four, thereby making the interchannel coupling proportionally smaller in the 4d case.

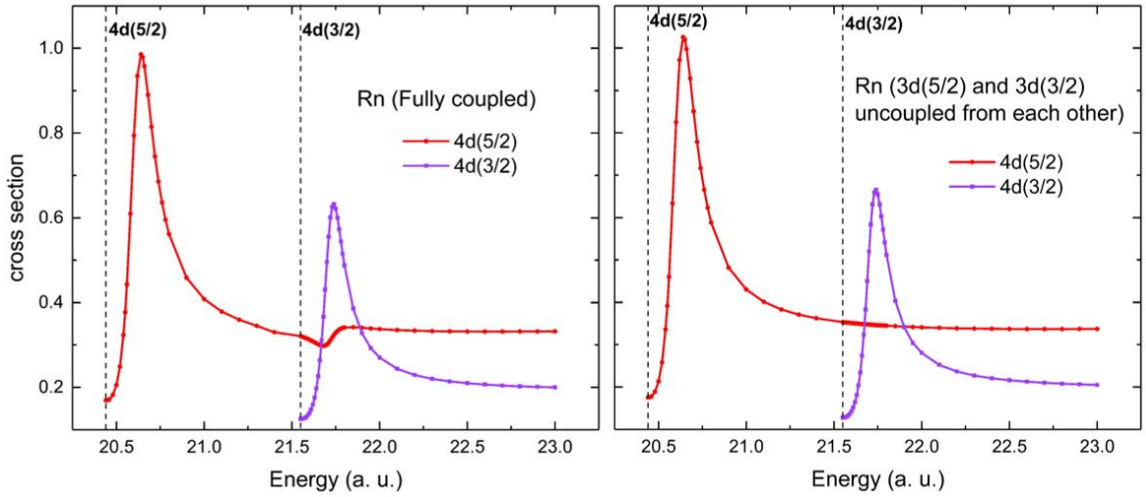

Figure 4.43 Calculated Rn 4d cross sections, 3d(3/2) (purple) and 3d(5/2) (red), left panel – fully coupled and right panel – uncoupled from each other.

5 CONCLUSIONS

A survey of the branching ratios of spin-orbit doublets of the noble gases Ne, Ar, Kr, Xe, Rn, and Hg has been conducted over a broad range of photon energies. It was found that photoionization branching ratios of spin-orbit doublets at high energies well above their thresholds, do not approach the statistical value of $(l + 1)/l$, but decrease with energy owing to the relativistic effects on the initial state np_j wave functions as predicted many years ago [8, 48] and confirmed experimentally for few cases recently [9].

The matrix element is generated at smaller and smaller r, closer to the nucleus, with increasing energy. This occurs due to the constraints of the combination of energy and momentum conservation in the photoionization process. Further away from the nucleus, both nl_j spin-orbit split wave functions behave similarly, and are virtually identical. But closer to the nucleus, nl_j bound states behave differently as a function of j as determined by the Dirac equation. As a result, the ratio of the radial charge densities of state $l-1/2$ to state $l+1/2$ increases as r decreases and diverges as $1/r^2$ as $r \rightarrow 0$. It was found that this phenomenon is caused the branching ratio to decrease from the statistical value at higher energies [49] and continue to decease with energy. Furthermore, this effect increases with Z since relativistic effect increases with Z.

Well above the thresholds, nd branching ratios fall off slower than np branching ratios with energy due to the strong centrifugal repulsion, which keeps the nd wave functions further away from the nucleus than np wave functions. The $4f$ branching ratio falls off even slower, owing to the huge angular momentum barrier involved in the $f \rightarrow g$ transitions. But, the initial state principal quantum number n is not important for the high-energy behavior of spin-orbit doublet branching ratios. This occurs because the wave functions of initial states of the same l but different n are

exactly the same at small r except for an overall normalization factor that cancels out in the branching ratios.

As suggested earlier [9, 10], it was found through this study that the branching ratios could be strongly affected in the vicinity of inner-shell thresholds through correlation in the final-state wave functions by interchannel coupling. The interchannel coupling affects the two members of spin-orbit doublets differently, indicating that the interchannel coupling itself is also affected by relativistic interactions. This effect is evident even in Ne, the lowest-Z atom studied.

The difference between the fully coupled and intrashell coupled branching ratios increases with Z for Ne, Ar and Kr. But the Xe results diverge from this behavior due to very complicated interchannel coupling interactions which can increase or decrease cross sections; with so many different interchannel coupling interactions in Xe, some of them apparently partially cancel out. Moreover, Kr and Xe branching ratios show an increase with energy in the vicinity of ns thresholds due to the interchannel coupling with np channels. This indicates that the interchannel coupling with inner shells is not limited to a small energy region around the subshell threshold, but it is operative over a broad energy range and redistributes the probability for photoionization.

As a rule, it was found that the interchannel coupling matrix elements were largest between photoionization channels of the same initial state angular momentum. This was demonstrated in the 4d branching ratio in the neighborhood of the 3d thresholds. In addition, the interactions became less important with increasing angular momentum difference. Interestingly, the 4f branching ratios of Hg and Rn show the highest variation around nd thresholds. In that case, coupling between nd and 4f subshells is stronger than the coupling between nd subshells.

The interchannel coupling effect of a particular channel on branching ratio decreases with the principal quantum number n of the spin-orbit doublets. This decrement with n can be explained

by noting that with the increasing n, the spin-orbit doublet wave functions move further away from the particular inner subshell, thereby decreasing the overlap and the interchannel coupling matrix element.

The SOIAIC effect was found earlier through experimental and theoretical studies in the Xe 3*d* spin-orbit doublets [13, 57]. In the present study, we found similar SOIAIC effects in Hg 3*d*, Rn 3*d*, and Rn 4*d* spin-orbit doublets. The *nd* subshells in those elements show shape resonance above their thresholds, and small extrema in *nd*(5/2) cross sections were found in the vicinity of *nd*(3/2) shape resonance maxima. And these structures were evident in the branching ratios as well.

In the final continuum state, the interchannel coupling (essentially configuration interaction in the continuum) mixes the wave functions of the various channels. As a result of this mixing channels with larger cross sections will transfer oscillator strength to the channel with the smaller cross section. This phenomenon is responsible for the SOIAIC effect in the *nd*(5/2) cross sections. Moreover, this interchannel coupling was seen to induce significant variations in high energy cross sections of all subshells of all the atoms studies, particularly in the neighborhood of inner-shell thresholds.

This research provides a broad theoretical analysis of relativistic effects and interchannel coupling interactions in the photoionization branching ratios of spin-orbit doublets in high-energy regions and gives an overview of the phenomenology. This work will be extended to higher Z atoms in the future to test the various conclusions that the present work has suggested. It will also be interesting to look at how the branching ratios of spin-orbit doublets work in the vicinity of *nf* thresholds. Other than the work of Ref.[9] there is no experimental work on the noble gas branching ratios at the higher energies. We hope the present paper will prompt new laboratory studies.

REFERENCES

[1] A.F. Starace, Theory of Atomic Photoionization, Handbuch der Physik, 6 (1982) 1-121.

[2] P.A.M. Dirac, R.H. Fowler, The quantum theory of the electron, Proceedings of the Royal Society of London. Series A, Containing Papers of a Mathematical and Physical Character, 117 (1928) 610-624.

[3] D.A. Keating, Evolution of Relativistic Effects in the Photoionization of Free and Confined Heavy Atoms, Georgia State University, 2018.

[4] E.J. Baerends, W.H.E. Schwarz, P. Schwerdtfeger, J.G. Snijders, Relativistic atomic orbital contractions and expansions: magnitudes and explanations, Journal of Physics B: Atomic, Molecular and Optical Physics, 23 (1990) 3225-3240.

[5] W.R. Johnson, K.T. Cheng, Photoionization of the outer shells of neon, argon, krypton, and xenon using the relativistic random-phase approximation, Physical Review A, 20 (1979) 978-988.

[6] J. Berkowitz, Photoabsorption, photoionization, and photoelectron spectroscopy, Academic Press, New York1979.

[7] P.C. Deshmukh, S.T. Manson, Photoionization of magnesium in the relativistic random-phase approximation, Physical Review A, 28 (1983) 209-217.

[8] Y.S. Kim, R.H. Pratt, A. Ron, Nonstatistical behavior of photoeffect subshell branching ratios at high energies, Physical Review A, 24 (1981) 1889-1893.

[9] R. Püttner, J.B. Martins, T. Marchenko, O. Travnikova, R. Guillemin, L. Journel, I. Ismail, G. Goldsztejn, D. Koulentianos, D. Céolin, M.L.M. Rocco, M.N. Piancastelli, M. Simon, D.A. Keating, C. Rasadi Munasinghe, P.C. Deshmukh, S.T. Manson, Nonstatistical behavior of the photoionization of spin–orbit doublets, Journal of Physics B: Atomic, Molecular and Optical Physics, 54 (2021) 085001.

[10] W. Drube, T.M. Grehk, S. Thieß, G.B. Pradhan, H.R. Varma, P.C. Deshmukh, S.T. Manson, Pronounced effects of interchannel coupling in high-energy photoionization, Journal of Physics B: Atomic, Molecular and Optical Physics, 46 (2013) 245006.

[11] W.R. Johnson, C.D. Lin, Multichannel relativistic random-phase approximation for the photoionization of atoms, Physical Review A, 20 (1979) 964-977.

[12] W.R. Johnson, C.D. Lin, K.T. Cheng, C.M. Lee, Relativistic Random-Phase Approximation, Physica Scripta, 21 (1980) 409-422.

[13] S. Banerjee, P.C. Deshmukh, A.S. Kheifets, S.T. Manson, Effects of spin-orbit-interaction-activated interchannel coupling on photoemission time delay, Physical Review A, 101 (2020) 043411.

[14] S.T. Manson, Atomic Photoelectron Spectroscopy, Part I, in: L. Marton (Ed.) Advances in Electronics and Electron Physics, Academic Press1976, pp. 73-111.

[15] P. Padukka, Inner-Shell Photoionization Of Free And Confined Mg, Georgia State University, 2014.

[16] B.H. Bransden, C.J. Joachain, Physics of atoms and molecules, 2nd ed. ed., Prentice Hall2003.

[17] A.F. Starace, Atomic Photoionization, in: H.O. Lutz, J.S. Briggs, H. Kleinpoppen (Eds.) Fundamental Processes in Energetic Atomic Collisions, Springer US, Boston, MA, 1983, pp. 69-110.

[18] K.T. Hecht, The Emission of Photons by Atoms: Electric Dipole Approximation, in: K.T. Hecht (Ed.) Quantum Mechanics, Springer New York, New York, NY, 2000, pp. 598-605.

[19] A. Starace, Photoionization of Atoms, in: G. Drake (Ed.) Springer Handbook of Atomic, Molecular, and Optical Physics, Springer New York, New York, NY, 2006, pp. 379-390.

[20] S.T. Manson, The Calculation of Photoionization Cross Sections: An Atomic View, Topics in Applied Physics V. 6: Photoemission in Solids I, Springer Verlag, Berlin, 1978, pp. 135 - 163.

[21] L.H. Thomas, The calculation of atomic fields, Mathematical Proceedings of the Cambridge Philosophical Society, 23 (1927) 542-548.

[22] D.R. Hartree, The Wave Mechanics of an Atom with a Non-Coulomb Central Field. Part II. Some Results and Discussion, Mathematical Proceedings of the Cambridge Philosophical Society, 24 (1928) 111-132.

[23] J.C. Slater, A Simplification of the Hartree-Fock Method, Physical Review, 81 (1951) 385-390.

[24] D.R. Hartree, The calculation of atomic structures, Reports on Progress in Physics, 11 (1947) 113-143.

[25] I.P. Grant, H.M. Quiney, Foundations of the Relativistic Theory of Atomic and Molecular Structure, in: D. Bates, B. Bederson (Eds.) Advances in Atomic and Molecular Physics, Academic Press1988, pp. 37-86.

[26] W.R. Johnson, K.T. Cheng, M.H. Chen, Chapter 3 - Accurate Relativistic Calculations Including QED Contributions for Few-Electron Systems, in: P. Schwerdtfeger (Ed.) Theoretical and Computational Chemistry, Elsevier2004, pp. 120-187.

[27] P. Jönsson, G. Gaigalas, P. Rynkun, L. Radžiūtė, J. Ekman, S. Gustafsson, H. Hartman, K. Wang, M. Godefroid, C. Froese Fischer, I. Grant, T. Brage, G. Del Zanna, Multiconfiguration Dirac-Hartree-Fock Calculations with Spectroscopic Accuracy: Applications to Astrophysics, Atoms, 5 (2017) 16.

[28] F. Salvat, J.M. Fernández-Varea, radial: A Fortran subroutine package for the solution of the radial Schrödinger and Dirac wave equations, Computer Physics Communications, 240 (2019) 165-177.

[29] O. Zatsarinny, C. Fischer, DBSR_HF: A B-spline Dirac-Hartree-Fock program, Comput. Phys. Commun., 202 (2016) 287-303.

[30] A.K. Razavi, Photoionization and Structure of the Superheavy Atoms No, Cn and Og, Department of Physics and Astronomy, Georgia State University, 2021.

[31] I.P. Grant, N.C. Pyper, Breit interaction in multi-configuration relativistic atomic calculations, Journal of Physics B: Atomic and Molecular Physics, 9 (1976) 761-774.

[32] M.Y. Amusia, The Ionization of Inner Shells of Atoms Taking Account of Outer Shell Rearrangement, in: R. Marrus, M. Prior, H. Shugart (Eds.) Atomic Physics 5, Springer US, Boston, MA, 1977, pp. 537-565.

[33] S. Manson, Relativistic-random-phase approximation calculations of atomic photoionization: what we have learned, Canadian Journal of Physics, 87 (2009) 5-8.

[34] X. Ren, P. Rinke, C. Joas, M. Scheffler, Random-phase approximation and its applications in computational chemistry and materials science, Journal of Materials Science, 47 (2012) 7447-7471.

[35] I.P. Grant, Relativistic calculation of atomic structures, Advances in Physics, 19 (1970) 747-811.

[36] H. Izadneshan, Numerical Solution Methods for Green Function and Solving the Time Independent Schroedinger Equation, Australian Journal of Basic and Applied Sciences, 5(10) (2011) 1352-1358.

[37] A.L. Fetter, J.D. Walecka, Quantum Theory of Many-Particle Systems., McGraw-Hill, New York.1971.

[38] S.T. Manson, Calculation of Auto-Ionization Rates, Physical Review, 145 (1966) 35-40.

[39] G.B. Armen, H. Aksela, T. Åberg, S. Aksela, The resonant Auger effect, Journal of Physics B: Atomic, Molecular and Optical Physics, 33 (2000) R49-R92.

[40] W. Ong, S.T. Manson, Dirac-Fock calculations of atomic photoionization: Branching ratios and angular distributions in the outer p shells of the noble gases, Physical Review A, 21 (1980) 842-850.

[41] S.T. Manson, A.F. Starace, Photoelectron angular distributions: energy dependence for s subshells, Reviews of Modern Physics, 54 (1982) 389-405.

[42] U. Fano, D. Dill, Angular Momentum Transfer in the Theory of Angular Distributions, Physical Review A, 6 (1972) 185-192.

[43] T.E.H. Walker, J.T. Waber, Spin-orbit coupling photoionization, Journal of Physics B: Atomic and Molecular Physics, 7 (1974) 674-692.

[44] J.L. Dehmer, J. Berkowitz, Partial photoionization cross sections for Hg between 600 and 250 Aº. Effect of spin-orbit coupling on the $^2D_{5/2}/^2D_{3/2}$ branching ratio of Hg, Physical Review A, 10 (1974) 484-490.

[45] T.E.H. Walker, J. Berkowitz, J.L. Dehmer, J.T. Waber, Nonstatistical Ratios of Photoionization Cross Sections for States Split by Spin-Orbit Coupling, Physical Review Letters, 31 (1973) 678-681.

[46] E.W.B. Dias, H.S. Chakraborty, P.C. Deshmukh, S.T. Manson, O. Hemmers, P. Glans, D.L. Hansen, H. Wang, S.B. Whitfield, D.W. Lindle, R. Wehlitz, J.C. Levin, I.A. Sellin, R.C.C. Perera,

Breakdown of the Independent Particle Approximation in High-Energy Photoionization, Physical Review Letters, 78 (1997) 4553-4556.

[47] D.L. Hansen, O. Hemmers, H. Wang, D.W. Lindle, P. Focke, I.A. Sellin, C. Heske, H.S. Chakraborty, P.C. Deshmukh, S.T. Manson, Validity of the independent-particle approximation in x-ray photoemission: The exception, not the rule, Physical Review A, 60 (1999) R2641-R2644.

[48] A. Ron, Y.S. Kim, R.H. Pratt, Subshell branching ratios of partial photoionization cross sections, Physical Review A, 24 (1981) 1260-1263.

[49] H.A. Bethe, E.E. Salpeter, Quantum Mechanics of One- and Two- Electron Atoms, Springer, Berlin, 1957.

[50] R.H. Pratt, H.K. Tseng, Behavior of Electron Wave Functions near the Atomic Nucleus and Normalization Screening Theory in the Atomic Photoeffect, Physical Review A, 5 (1972) 1063-1072.

[51] R.H. Pratt, A. Ron, H.K. Tseng, Atomic Photoelectric Effect Above 10 keV, Reviews of Modern Physics, 45 (1973) 273-325.

[52] Y.S. Kim, Normalization screening theory manifested in photoeffect, Radiation Physics and Chemistry (1993), 59 (2000) 145-147.

[53] F.A. Parpia, W.R. Johnson, V. Radojevic, Application of the relativistic local-density approximation to photoionization of the outer shells of neon, argon, krypton, and xenon, Physical Review A, 29 (1984) 3173-3180.

[54] S.T. Manson, J.W. Cooper, Photo-Ionization in the Soft x-Ray Range: Z Dependence in a Central-Potential Model, Physical Review, 165 (1968) 126-138.

[55] A. Kivimäki, U. Hergenhahn, B. Kempgens, R. Hentges, M.N. Piancastelli, K. Maier, A. Rüdel, J.J. Tulkki, A.M. Bradshaw, Near-threshold study of Xe 3d photoionization, Physical Review A, 63 (2000) 012716.

[56] M.Y. Amusia, L.V. Chernysheva, S.T. Manson, A.M. Msezane, V. Radojević, Strong Electron Correlation in Photoionization of Spin-Orbit Doublets, Physical Review Letters, 88 (2002) 093002.

[57] V. Radojević, D.M. Davidović, M.Y. Amusia, Near-threshold photoionization of the Xe 3d spin-orbit doublet: Relativistic, relaxation, and intershell interaction effects, Physical Review A, 67 (2003) 022719.

[58] S.T. Manson, Dependence of the angular distribution of atomic photoelectrons on energy and z. II. d- and f-subshells, Journal of Electron Spectroscopy and Related Phenomena, 37 (1985) 37-56.

[59] U. Fano, Effects of Configuration Interaction on Intensities and Phase Shifts, Physical Review, 124 (1961) 1866-1878.

[60] A.K. Razavi, R.K. Hosseini, D.A. Keating, P.C. Deshmukh, S.T. Manson, Photoionization of superheavy atoms: correlation and relativistic effects, Journal of Physics B: Atomic, Molecular and Optical Physics, 53 (2020) 205203.

[61] M. Kutzner, P. Pelley, L. Banks, R. Robertson, L. Caesar, Many-body effects in the photoionization of radon, Physical Review A, 61 (2000) 062703.

[62] P.C. Deshmukh, V. Radojević, S.T. Manson, Photoionization of the outer shells of radon and radium: Relativistic random-phase approximation for high-Z atoms, Physical Review A, 45 (1992) 6339-6348.

APPENDICES

A. Dipole Approximation

In the photoionization process, the interaction of a photon with an electron of an atom depend on the exponential term $e^{i\bar{k}\cdot\bar{r}}$ as in equation 2.6. Where $\bar{k}$ is the wavenumber of the incident photon and $\bar{r}$ is the coordinate of the target electron. This exponential term can be expanded as in equation 2.7, and it can be replaced by unity using the dipole approximation.

$$\left|\bar{\boldsymbol{k}}\cdot\bar{\boldsymbol{r}}\right| = \frac{\boldsymbol{p}}{\hbar}\boldsymbol{r} = \frac{\boldsymbol{E}}{\hbar\boldsymbol{c}}\boldsymbol{r} = \frac{\boldsymbol{E}\boldsymbol{a_0}}{\hbar\boldsymbol{c}}\frac{\boldsymbol{r}}{\boldsymbol{a_0}} = \boldsymbol{\alpha E}\frac{\boldsymbol{r}}{\boldsymbol{a_0}}. \qquad \textbf{(A.1)}$$

Where *P* and *E* are the momentum and energy of the incident photon. For an inner shell, $r/a_0 \sim 0.1$ and for a photon with wavelength $\lambda >> 100$ Å, $|k\cdot r| \ll 1$. Then the exponential term can be replaced by unity. If $|k\cdot r| = 0.1$ then, $E = 137\ a.u.$ as in equation A.1. If we take the second term of the expansion (quadrupole term),

$$\boldsymbol{e^{i\boldsymbol{k}\cdot\boldsymbol{r}} = 1 + i\boldsymbol{\kappa}\cdot\boldsymbol{r}}. \qquad \textbf{(A.2)}$$

Where the second term is nearly 0.1, however, the first and second terms go to different final states, and thus there are no cross terms. And, since the cross sections depend upon the absolute squares are the matrix elements, the absolute squares of the first two terms should be compared. Then, noting the dot product of the second (quadrupole) term introduces a cosine, and the average value of the square of the cosine is ½, we find that for outer shells, the quadrupole cross section is less than 10% of the dipole cross section up to an energy of about 100 a.u.; for inner shells, this becomes about 800 a.u. Therefore, for the present calculations, we use the electric dipole approximation, i.e. the above expansion A.2 is replaced by unity.

B. Selection rules for electric dipole transitions

Since the total angular momentum J and the parity operators of electrons in atoms commute with the total Hamiltonian operator, atomic states are eigenstates of J^2, J_z (with quantum numbers J and M_J, respectively) and of parity. Therefore to have non-vanishing Clebsch-Gordan coefficients for the electric dipole matrix, the following selection rules are applied for the allowed dipole transitions of photoionization of atomic electrons [16].

a. $\Delta M_J = 0, \pm 1$

b. $\Delta J = 0, \pm 1$ ($J = 0 \leftrightarrow J' = 0$ forbidden)

c. According to Laporte's rule, initial and final atomic states must have opposite parity.

Where prime above the quantum numbers indicates the final state. If the spin-orbit interactions are weak (L-S coupling limit), then the total orbital angular momentum L and the total spin angular momentum S of electrons are conserved. In this situation, selection rules can be written as follows [16],

a. $\Delta M_L = 0, \pm 1$

b. $\Delta L = 0, \pm 1$ ($L = 0 \leftrightarrow L' = 0$ forbidden)

c. $\Delta S = 0$